UCGE Reports
Number 20239

Department of Geomatics Engineering

Performance Evaluation of Low Cost MEMS-Based IMU Integrated With GPS for Land Vehicle Navigation Application

(URL: http://www.geomatics.ucalgary.ca/research/publications/GradTheses.html)

by

Saurabh Godha

February 2006

UNIVERSITY OF CALGARY

PERFORMANCE EVALUATION OF LOW COST MEMS-BASED IMU INTEGRATED WITH GPS FOR LAND VEHICLE NAVIGATION APPLICATION

by

SAURABH GODHA

A THESIS

SUBMITTED TO THE FACULTY OF GRADUATE STUDIES

IN PARTIAL FULFILMENT OF THE REQUIREMENTS FOR THE

DEGREE OF (MASTER OF SCIENCE)

DEPARTMENT OF GEOMATICS ENGINEERING

CALGARY, ALBERTA

FEBRUARY, 2006

ABSTRACT

Land vehicle navigation system (LVNS) technology is a subject of great interest today due to its potential for both consumer and business vehicle markets. Global Positioning System (GPS) is a common choice for positioning in such systems. However, GPS alone is incapable of providing continuous and reliable positioning, because of its inherent dependency on external electromagnetic signals. The availability of low cost MEMS inertial sensors is now making it feasible to use Inertial Navigation System (INS) in conjunction with GPS to fulfill the demands of such systems. This thesis therefore evaluates the positioning capability of GPS/INS integrated systems utilizing MEMS Inertial Measurement Units (IMU) for LVNS and investigates on methods to improve its performance.

The primary piece of equipment used is a MEMS-based Crista IMU (from Cloud Cap Technology Inc.) and a NovAtel OEM4 GPS receiver. A tactical grade Honeywell HG1700 IMU is also used to compare the performance differences of the two IMUs, under similar operating conditions. Different GPS/INS integration strategies and different INS filters are used to asses the system performance under various operating conditions based on GPS availability. For keeping the errors from growing in MEMS INS under challenging GPS environments, the use of vehicle motion-specific constraints is evaluated. This method is suitable for real-time applications. For post-mission applications the use of backward smoothing techniques, such as the Rauch-Tung-Streibel (RTS) smoother, is investigated.

The performance of the system is assessed primarily in terms of position and velocity errors computed with respect to an independent navigation solution. The results show that under complete GPS coverage, the GPS/MEMS INS integrated system provides accuracies of better than 0.4 m in the position domain. The integrated system provides RMS horizontal position accuracies better than 7 m in a severely signal degraded environment. The performance improves significantly with the proposed use of vehicle motion constraints and backward smoothing techniques. Overall the results confirm the strong potential of GPS/MEMS INS integrated systems for their use in land vehicle navigation applications.

ACKNOWLEDGEMENTS

I would like to thank my supervisor, Dr. M. Elizabeth Cannon, for her support, guidance and encouragement throughout my studies. I would further like extend my appreciation to members and ex-members of PLAN group for their help in various ways, during my studies. I am grateful to the members of my examining committee, Dr. Gérard Lachapelle, Dr. Mathew Tait, and Dr. Elise Fear, for their efforts in reading through this thesis.

Most of all, I would like to thank my parents, for their love, encouragement and understanding through all of my years of study. This work would not have been possible without their support.

DEDICATION

To my parents.

TABLE OF CONTENTS

LIST OF TABLES

LIST OF FIGURES

LIST OF SYMBOLS

bar	…Averaged quantity
dots	…Time derivative
hat	…Estimated quantity
~	…Measured value by the sensor
*	…Nominal state vector value
$( )(t)$	…Quantity as a function of time
$( )_k$	…Quantity at k^{th} epoch
$( )^-$	…Predicted quantity
$( )^+$	…Updated quantity
$( )^q$	…Quantity in q-frame,
$( )_a$	…Accelerometer specific quantity
$( )_g$	…Gyro specific quantity
$\frac{\partial}{\partial X}$	…Partial derivative with respect to X
A B	…Weighing matrices
E^e	…Skew-symmetric matrix of misalignment error states
F	…System dynamic matrix
G	…Shaping matrix
	…Smoothing Gain
H	…Design matrix
I	…Identity matrix
K	…Kalman gain matrix
M	…Design matrix mapping blunder onto observations
$N(p, q)$	…Normal distribution with mean p and variance q
N	…Prime Vertical radius
	…Tensor of gravity gradients

P	…Error covariance matrix associated with state vector
$Q(t)$	…Spectral density matrix
Q	…Process noise covariance matrix
R	…Measurement noise covariance matrix
R_p^q	…Rotation matrix from the *p*-frame to the *q*-frame
S_X	…Scale-factor errors of sensor *X*
b_X	…Turn-on bias of sensor *X*
c	…Speed of light in vacuum (2.99792458×10^8 m/s)
d_{ion}	…Ionospheric error
d_{orb}	…Satellite orbital error
d_{trop}	…Tropospheric error
dt	…Satellite clock error
dT	…Receiver clock error
e	…Eccentricity
f	…Specific force
	…System model non-linear function
h_0 , h_2	…Allan variance parameters that describe clock-drift
h	…Ellipsoidal height
	…Measurement model non-linear function
m	…Non-orthogonality error
p	…Pseudorange
q_i	…Quaternions $i = 1…4$
	…Spectral density of *i*
r	…Position vector (x^e, y^e, z^e)
v	…Velocity vector (v_x^e, v_y^e, v_z^e)
	…Innovation sequence
$v^e \times$	…Skew-symmetric matrix of velocity vector

w …Angular rate

…Process Noise

x …State vector

z …Observation vector

δb_X …Bias-drift of sensor X

∇ …Blunder vector

τ_i …Correlation time of process i

ω_e …Earth's rotation rate (15.041˚/h)

γ^e …Normal gravity vector $(\gamma_x^e, \gamma_y^e, \gamma_z^e)$

ψ …Heading

ϕ …Latitude

λ …Longitude

ε …Misalignment error state vector $(\varepsilon_x, \varepsilon_y, \varepsilon_z)$,

δ …Perturbation from the nominal value

η …Pitch

η_X …Random noise of system X

ξ …Roll

ω_{pq}^r …Rotation rate of the q-frame, relative to the p-frame, expressed …in the r-frame.

Ω_{pq}^r …Skew symmetric matrix of the rotation rate ω_{pq}^r

σ_X …Standard deviation of X

ρ …True range between satellite and receiver antenna (m)

Φ …Transition matrix

Δt …Time increment $(t_{k+1} - t_k)$

$\Delta\theta_{pq}^r$ …Vector of angular increments of q frame, relative to p frame, …expressed in r frame

Δv_f^q …Velocity increments expressed in q frame

LIST OF ABBREVIATIONS

BDS	…Black Diamond System
C/A-code	…Coarse/Acquisition code
CCIT	…Calgary Center for Innovative Technology
CDMA	…Code Division Multiple Access
C/N_0	…Carrier to Noise Density Ratio
$C^3NavG^{2™}$	…Combined Code and Carrier for NAVigation with GPS and …GLONASS Software
CIMU	…Commercial Inertial Measurement Unit
DD	…Double Difference
DR	…Dead Reckoning
DGPS	…Differential GPS
DOP	…Dilution of Precision
ECEF	…Earth-Centred Earth-Fixed
EKF	…Extended Kalman Filter
GPS	…Global Positioning System
HDOP	…Horizontal Dilution of Precision
HSGPS	…High-Sensitivity GPS
IMU	…Inertial Measurement Unit
INS	…Inertial Navigation System
ISA	…Integrated System Availability
LBS	…Location Based Services
LC	…Loose Coupling
LKF	…Linearized Kalman Filter
LLF	…Local Level Frame
LOS	…Line of Sight
LSQ	…Least Square
LVNS	…Land Vehicle Navigation System
MEMS	…Micro Electro Mechanical Systems
P-code	…Precise Code
PPM	…Parts-Per-Million

PIT	…Pre-detection Integration Time
PPS	…Pulse-Per-Second
PRN	…Pseudo-Random Noise
PV	…Position Velocity
PVA	…Position Velocity Acceleration
RHCP	…Right Hand Circularly Polarized
RF	…Radio-Frequency
RLG	…Ring Laser Gyro
RMS	…Root Mean Square
RTS	…Rauch-Tung-Streibel
SD	…Single Difference
SV	…Satellite Vehicle
TC	…Tight Coupling
TD	…Triple Difference
TEC	…Total Electron Content
VDOP	…Vertical Dilution of Precision
ZUPT	…Zero Velocity Update

CHAPTER ONE : INTRODUCTION

The E911 mandate and the emergence of location-based services (LBS) have been the main thrusts in the demand and growth of positioning products such as in-car navigation systems, personal-locator systems (PDA/mobile phones), and fleet management systems. Some of the purposes of these products is to provide accurate position information of users/vehicles to be able to connect them to nearby points of interest (such as retail businesses, public facilities, or travel destinations), to be able to advise them of current conditions (e.g. traffic), or to be able to provide routing and tracking services (Liu 2002). This thesis discusses LBS in the context of a Land Vehicle Navigation System (LVNS).

1.1 Background

LVNS has been a major focus for research over the past decade. The aim of such a system is to accurately locate a vehicle on a road network, and thus the positioning technology is an important requirement. An ideal positioning technology in LVNS will have the following characteristics:

1. *Ability to provide continuous and reliable navigation solution*
2. *Ability to maintain acceptable accuracy levels*

The accuracy requirement for a land vehicle generally varies with the application. For instance, the acceptable accuracy level for emergency services like an ambulance is 15-20 m (2D, 95%), whereas the corresponding requirement for an autonomous car is at the sub-metre level.

Different technologies exist to determine the position of a vehicle, out of which two are used most commonly. The first is the Global Positioning System (GPS) which relies on the radio-frequency (RF) signals from satellites in space which have known locations. The second technology is an Inertial Navigation System (INS), which is a self-contained Dead Reckoning (DR) navigation system, and provides dynamic information through direct measurements from an Inertial Measurement Unit (IMU).

Over the years, increasingly falling cost of GPS receivers has rendered the system attractive for the design of LVNS (Zhao et al 2003). The primary advantage of using GPS includes its ability to provide absolute navigation information, and the long term accuracy in the solution. Although the solution provided by GPS is sufficiently accurate (especially when used in differential mode), it is unable to fulfill the requirements of continuity and reliability in many situations. Being a satellite-based navigation system, GPS requires line-of-sight (LOS) between the receiver antenna and the satellites. However, in the case of a land vehicle, the LOS criteria may not always be met, because a land vehicle typically moves in urban and under dense foliage environments which prevent signals from reaching the antenna. Thus, signal interruption is one of the primary reasons which affects the continuity and reliability of the navigation solution from GPS (Kaplan 1996). The issue of continuity is addressed to some extent by High Sensitivity GPS receivers (HSGPS). HSGPS tracks signals at low strengths, using longer pre-detection integration times (PIT) and data wipe-off methods, and thus typically provide a higher number of measurements relative to a conventional GPS receiver (Chansarkar & Garin 2000, MacGougan 2003). However, the use of such measurements in degraded

signal environments can be detrimental to the navigation solution if measurement faults are not identified and understood, which in turn could result in position errors of 100s of metres (ibid)**.** Thus, in general GPS cannot be solely used for navigation, especially in urban environments.

Unlike GPS, an INS is a self contained DR navigation system which provides position and velocity information through direct measurements from an IMU. The advantage of INS over GPS is its independence from external electromagnetic signals, and its ability to operate in all environments. This allows an INS to provide a continuous navigation solution, with excellent short term accuracy (Chiang 2004). However, the INS suffers from time-dependent error growth which causes a drift in the solution, thus compromising the long term accuracy of the system. The drift of high quality inertial devices is small, and can fulfill the accuracy requirement in land applications for longer periods. However, there are two specific limitations for their use in general applications, such as LVNS. One is their price (over US $90,000 for a high-end IMU and over $10,000 for medium grade IMUs), and the other is the regulation by the governments against their unrestricted use (Shin 2001). Due to these limitations, the use of INS has generally been confined to only high accuracy navigation and geo-referencing applications (Hide 2003).

Recently, with advances in Micro Electro-Mechanical Systems (MEMS) technology, low cost MEMS-based inertial sensors are available (Barbour & Schmidt 2001, Park 2004). The immediate start-up time, low power consumption, weight and cost of these sensors meet the specifications and requirements needed for commercial applications, like

vehicle navigation. However, due to relative lack of maturity of this technology, the performance of these sensors is limited (Shin et al 2005), which causes the navigation solution to degrade rapidly in the absence of an aiding source. The errors of even today's most accurate INS (based on high end IMUs) would become unacceptably large after several minutes (Gaylor 2003). It therefore becomes necessary to provide an INS with regular updates in order to bound the errors to an acceptable level.

The powerful synergy between the GPS and INS, and the availability of low cost MEMS sensors, makes the combination of these two navigation technologies a viable positioning option for LVNS. Their combination not only offers the accuracy and continuity in the solution, but also enhances the reliability of the system (Rogers 2000). GPS, when combined with MEMS inertial devices, can restrict their error growth over time, and allows for online estimation of the sensor errors, while the inertial devices can bridge the position estimates when there is no GPS signal reception. Also, the use of inertial components allows the GPS measurements to be compared against statistical limits and reject those measurements that are beyond the limits, thus enhancing the reliability and integrity of the system (Brenner 1995). Ultimately, the navigation solution derived from a GPS/INS system is better than either standalone solution.

As GPS/MEMS INS (INS utilizing MEMS IMU) systems constitute an increasingly attractive low cost option, it is of significant importance to evaluate their performance. Thus, the broad aim of this research is to evaluate the performance of a GPS/MEMS INS

integrated system, and to develop a system capable of providing an accurate navigation solution, reliably and continuously for land vehicle navigation application.

1.2 Low Cost Inertial Sensors

The need to maintain reasonable cost levels when integrating an INS with GPS for consumer applications is driving the technology development for MEMS inertial sensors (Barbour & Schmidt 2001). MEMS-based sensors exploit the benefits of high volume manufacturing techniques and flexible and rugged packaging options (Faulkner et al 2002). This results in small and robust inertial sensors that are resulting in new markets, where inertial technology is now being used in applications that were previously not feasible due to size and cost constraints (ibid). To this end, MEMS inertial sensors are the lowest cost inertial sensors available for use in commercial applications, such as land navigation (Hide 2003). These sensors, based on their performance levels and intended applications, are often categorized under automotive grade sensors (ibid). This section provides a brief overview of MEMS inertial sensor technology, and their performance differences relative to tactical and navigation grade IMUs.

1.2.1 MEMS Inertial Sensors

MEMS research on inertial sensors has focused primarily on accelerometers and gyroscopes (Park 2004). Of the two, accelerometers were developed first, and have undergone significant development ever since. However, MEMS gyroscopes are a relatively new technology (ibid).

MEMS accelerometers are typically a pendulous/displacement mass type system that uses capacitive sensing to provide a measure of acceleration. It consists of a proof mass located at the centre of two electrodes, each made of silicon. The deflection of the proof mass leads to the change of capacitance which is used to measure the amplitude of the force that led to displacement of the proof mass (Kraft 1997). This method is generally termed as an open loop mode of operation. Another mode is the closed loop, where the counteracting force required to keep the proof mass at zero-deflection point is measured, to provide a measure of acceleration (Park 2004)**.** These silicon accelerometers are being developed for a wide range of applications commercially such as automotive air bags, as well as autonomous vehicle markets (Barbour & Schmidt 2001).

The majority of MEMS-based gyroscopes currently under development operates in a vibratory mode and measures the angular rate instead of the absolute angle (Park 2004). These gyros consist of a sensing element vibrating with constant amplitude controlled by a vibrating motor that maintains the oscillation at constant amplitude. When this system is rotated around any axis other than the axis of its internal in-plane vibration, the Coriolis force causes the element to oscillate out of the plane (Faulkner et al 2002). This oscillation is picked-up by the sensing capacitors and is used to provide a measure of angular rate.

1.2.2 Performance Characteristics

Table 1.1 lists the typical error characteristics of low cost MEMS sensors. The table also shows the error characteristics of navigation and tactical grade IMUs to facilitate direct

performance comparison. The MEMS IMU used in this study is the Crista IMU (from Cloud Cap Technology Inc.), which is used as an example (in the table) to characterize the performance of low cost MEMS IMUs. The navigation grade IMU used is the Honeywell Commercial IMU (CIMU) and the tactical grade IMU used is the Honeywell HG1700 IMU.

Table 1.1: Technical Characteristics of Different IMU Grades (Crista-Interface/Operation Document 2004, Petovello 2003)

IMU	***CIMU***	***HG1700***	***Crista***
Grade	***Navigation***	***Tactical***	***Automotive***
	Accelerometers		
In Run Bias (mg)	0.025	1	2.5
Turn On Bias (mg)	-	-	30
Scale Factor (PPM)	100	300	10000
Velocity Random Walk (g/√Hz) *	-	2.16e-006	370e-006
	Gyros		
In Run Bias (°/h)	0.0022	1	<1040
Turn On Bias (°/h)	-	-	5400
Scale Factor (PPM)	5	150	10000
Angle Random Walk (°/h /√Hz) *	6.92	7.5	226.8
Cost	>$90000	>$20000	<$2000

* ***Obtained from static testing in lab***

The quality of an IMU is often judged by the quality of the gyros contained in the sensor system (El-Sheimy 2004). As can be noted from the table, that MEMS IMU (Crista IMU) features a turn-on bias of about 5400 °/h in gyros, while these biases are negligible in

higher grade IMUs. Also, the MEMS IMU exhibits in-run bias drift of more than 1000 ˚/h, compared to 1 ˚/h for a tactical grade system, and few orders of magnitude lower for a navigation grade IMU. Given this level of errors in MEMS sensors, traditional approaches for integrating GPS and INS are likely to fail, and some non-traditional algorithms and approaches are required (Salychev et al 2000). However, in terms of cost the MEMS-level IMU is clearly a favourable option for the use in commercial applications. As can be noted, the cost of MEMS inertial sensors is ten times lower than that of medium accuracy tactical grade IMUs.

1.3 Previous Research and their Limitations

In the last few years, several researchers have investigated the integration of low performance/MEMS INS with GPS, for instance Salychev et al (2000), Mathur & Grass (2000), Kealy et al (2001), Cao et al (2002), Hide (2003), Park (2004), and Shin (2005). The following sections discuss the key aspect of a GPS/INS integrated system (from the MEMS INS stand point), and the relevant research undertaken along with their limitations.

1.3.1 Integration Strategy

The concept of integrating GPS and INS has been well researched. Different integration strategies have been developed and tested with different grades of IMUs. Typically, three main strategies are used, namely loose integration, tight integration and ultra-tight (or deep) integration (Petovello 2003). Deep integration is performed at the hardware level and thus, is practical for implementation by equipment manufacturers only (Bye et al 1997, Kreye 2000) or through software receivers (Kondo et al 2005), and hence will not

be discussed any further. The other two integration strategies, i.e. loosely and tightly coupled, have been used most commonly in past research. Both integration strategies can be implemented using two independent approaches, the open loop (feed forward) and the closed loop (feedback).

Studies involving low performance/MEMS IMU which have been conducted over the last few years have mainly concentrated on the loosely coupled integration approach. Salychev et al (2000), Nayak (2000), and Mathur & Grass (2000) evaluated the ability of a low cost motion sensor, specifically the MotionPak^{TM} IMU (which costs about $8000 US) integrated with GPS using a loosely coupled integration strategy with an open loop approach. While the former two used pseudorange/Doppler-derived DGPS updates, the latter used carrier-phase based DGPS, both for land vehicle and aviation applications. Kealy et al (2001) developed an intelligent integrated system based on a MEMS based AHRS-DMU^{TM} (which costs more than $4000 US), and map data, specifically for a land vehicle. Some recent work has focused on the tightly coupled integration strategy, for instance Hide (2003), and Brown & Lu (2004). Hide (2003) used a Crossbow AHRS DMU-HDX (which costs more than $4000 US), with carrier-phase based DGPS, for marine application. Brown & Lu (2004) presented some preliminary performance test results of the MEMS-based Crista IMU (which is the IMU used in this study). The position errors in this system were shown to grow rapidly during GPS outages, reaching more than 225 m (2D) for the outage duration of 50 s.

One specific limitation of many of these researches is that an open loop approach is used for integration, which is suitable only for integration with high-end inertial sensors. A low cost IMU propagates relatively large navigation errors in a small time interval. Without a feedback loop the inertial sensor measurements, and the mechanization parameters, will have higher error values which can spoil the small error assumptions made in an INS error model, and could potentially degrade system performance (Zhang 2003). A closed loop configuration corrects the INS parameters periodically using the error estimates from the Kalman filter, and thus maintains the small error assumptions.

1.3.2 Initial Alignment

One of the important issues while working with a low cost MEMS IMU is the initial alignment of the system. The process of computing the initial parameter of the transformation matrix (from the IMU body frame to the navigation frame) is called the INS alignment procedure (Jekeli 2001). For navigation-grade and high-end tactical grade IMUs, the analytical coarse alignment method followed by fine alignment can be applied to estimate the initial attitude parameters (Farrell & Barth 2001). However, for low cost IMUs, these methods often fail owing to large sensor errors (see Table 1.1). The roll and pitch of vehicle can still be obtained using the stationary accelerometer data with limited accuracy, but heading (azimuth) alignment cannot be accomplished. Another practical problem in using conventional static alignment methods is that the system is slated to be used in a consumer vehicle; hence, the user cannot be expected to wait until the sensor alignment is finished (Shin & El-Sheimy 2004).

Different options, such as kinematic alignment and the use of an external heading sensor, have been tested in previous studies. Salychev et al (2000) and Nayak (2000) used heading information stored from a magnetic compass as periodic input to their integrated system for heading alignment. The possibility of using GPS processed navigation information for in-motion INS alignment is explored in Shin (2001), Salycheva & Cannon (2004), and Shin & El-Sheimy (2004). While the former two studies discuss the algorithm involving the use of GPS processed velocity information to align the INS, which was tested with a tactical grade IMU, the latter used GPS processed position information for alignment of a medium accuracy MEMS IMU.

1.3.3 Sensor Error Calibration/Modeling

The performance of a GPS/INS integrated system is mainly characterized by the ability of the INS to bridge GPS outages. This basically depends on the inertial sensor errors, which, if remain un-accounted for, cause a rapid degradation in the INS navigation solution during periods of GPS unavailability. The inertial sensor errors can be divided into two parts, deterministic errors and random errors (Salychev 1998, Nassar 2003). In order to integrate MEMS inertial sensors with GPS, and to provide a continuous and reliable navigation solution, the characteristics of different error sources, and the understanding of the variability of these errors are of significant importance (Park & Gao 2002). The process of understanding the sensor error behaviour is called sensor error characterization (Grewal et al 2001).

Deterministic error sources include the bias and scale-factor errors which can be removed by specific calibration procedures. These errors are deterministic in the sense that their values can be obtained by performing several tests in the laboratory. Park & Gao (2002), Winkler et al (2003), and Park (2004) discuss the lab calibration procedure for MEMS inertial sensors. They developed a turn table test procedure to estimate the biases and scale-factor errors in these sensors. Shin (2001) developed a field calibration procedure which requires rotating the IMU, manually, through a specific scheme of rotations. The developed methodology was tested with a tactical grade IMU. A field calibration scheme is specifically useful for low cost IMUs, whose constant bias part and scale factor error values vary from turn-on to turn-on. Another option, as discussed in Godha & Cannon (2005a), is to model these errors in a Kalman Filter.

The inertial sensor random errors primarily include the sensor noise, which consists of two parts, a high frequency component and a low frequency component. The high frequency component has white noise characteristics, while the low frequency component (more commonly termed as bias drift) is characterized by correlated noise (Skaloud 1999). One way to deal with high frequency noise is to de-noise the inertial sensor measurements prior to processing, using the wavelet de-noising techniques. Several studies have focused on evaluating the advantages of such techniques, for instance Skaloud (1999), Nassar (2003), Chiang et al (2004), and Abdel-Hamid et al (2004). Of these, Chiang et al (2004), and Abdel-Hamid et al (2004) specifically looked at the wavelet de-noising application with MEMS IMU, for LVNS. The former demonstrated an improvement in stand-alone INS performance by about 5-20 % after de-noising the

inertial sensor measurements, while the latter showed an improvement in the range of 30-60% with de-noising.

The low frequency noise component (correlated noise) can be modeled with sufficient accuracy using random processes such as random constant (random bias), random walk, or a Gauss-Markov processes. Details of these stochastic models could be found in Gelb (1974) and Nassar (2003). The most commonly used process is the first order Gauss Markov process. Recently some of the studies have tested the use of Auto-Regressive (AR) modeling methods (e.g. Park 2004), which were shown to provide slight improvement in system performance.

1.3.4 Rapid Degradation in Solution during GPS Outage

The primary concern when working with a low performance IMU is that the navigation solution degrades rapidly in the absence of an aiding source (which is mainly GPS). So, to constrain the system errors to acceptable levels during this period, some additional form of aiding is required (Wang & Wilson 2002). Different researchers have come up with different ways to deal with this situation, specifically the use of an auxiliary sensor system, deriving measurements based on vehicle behaviour, and some special estimation techniques.

Several researchers have investigated methods to prevent INS error degradation during GPS outages with the help of auxiliary sensors such as an odometer (Sukkarieh 2000, Shin 2005, Shin & El-Sheimy 2005), magnetometer (Zhang et al 2003, Godha et al

2005), Vehicle Motion Sensors (Numajima et al 2002), and an array of pseudolites (Lee 2002). However, the use of additional sensors limits the application areas of these navigation systems, and also increases the cost of the overall system.

The problem of keeping the accuracy of the INS within bounds can also be addressed by considering the vehicle motion constraints arising from the fact that the land vehicles mostly travel on roads (Scott 1994). Assuming that the vehicle does not slip and always remains in contact with the ground, the velocity of the vehicle in the plane perpendicular to the forward direction should be zero (Sukkarieh 2000). Observations constructed using this fact can be used in the INS data processing loop when GPS is not available, in order to extend the ability of the system to keep the position accuracy within bounds for longer periods (Cunha et al, 2003). Sukkarieh (2000) demonstrated the effectiveness of these constraints with a medium accuracy IMU, Shin (2001) used constraints to bound the mechanization errors in a tactical grade IMU, and recently Wang (2004) demonstrated their use with a single axis MEMS gyro and accelerometer. An important limitation of these works is that, none of these studies used a MEMS IMU for their integrated system Also, all of these studies focused on constraining the mechanization errors with only updates coming from velocity constraints, with no GPS updates. The other means of implementation is to use GPS when it is available with INS to provide navigation information, and when a GPS outage (complete or partial) is encountered, constraints-derived velocity measurements are added to the system to keep the velocity, and thus position, errors bounded (Godha & Cannon 2005a).

Another constraint that can be imposed in a land vehicle environment is a height constraint (Godha et al 2005). Since the vehicle always stays on the road, the height solution does not generally vary by more than a few tens of metres over a particular region. Therefore, during periods of poor GPS availability, the height solution could be considered as a known parameter, which can potentially help to improve the horizontal solution accuracies (Lachapelle et al 2003).

The use of special estimation techniques, such as backward smoothing, can be used to improve system performance during GPS outages. Smoothing uses the fact that the sensor data can also be used in a reverse time fashion (Gelb 1974). It provides an estimate using the observation that is ahead in time of the current estimate; therefore, smoothing is clearly a post processing method. Different smoothing techniques exist, for instance the Forward-Backward smoother and the Rauch Tung Streibel (RTS) smoother (Gelb 1974, Scherzinger 2004), out of which the RTS smoother seems to be gaining popularity because of its ease of implementation. Nassar (2003) used an RTS smoother to reduce the errors accumulated in both navigation and tactical grade INSs. The smoother was shown to improve the navigation solution by about 75-85%. Shin & El-Sheimy (2005) used the same smoother for a pipeline surveying application, with a tactical grade IMU. Only one study (to the author's knowledge) has focused on the use of an RTS smoother with a MEMS level IMU, Shin (2005); however, the study was somewhat limited as the performance of smoother was tested with just one data set collected in open sky conditions. Thus, further investigation on the performance of RTS smoother with MEMS IMU is desired.

1.3.5 Operational Environment

The operational environment of a navigation system plays a large role in the quality of solution obtained (Petovello 2003). Operational environments are generally characterized into three categories based on the number of GPS satellites available. These are: (1) open area (average of 8-12 satellites available); (2) semi-urban area (average of 2-8 satellites available); and (3) urban area (average of 0-6 satellites available) (Salycheva 2004). Most previous studies (involving MEMS level/low performance IMU), have focused on evaluating the system performance under benign operational conditions (open area with a clear view of sky). The performance in urban environments is more commonly quantified by simulating a GPS outage (by rejecting satellites in post processing) in an otherwise good GPS conditions. While this method is valid for an evaluation of the stand-alone performance of an INS, it is generally not well representative of the possible accuracies in an urban environment (Godha et al 2005). The reason for this is two fold. First, GPS outages in an urban environment are very frequent, vary in duration, and are often a blend of complete and partial outages. Second, in actual conditions GPS data (when available) is degraded primarily by poor satellite geometry, low C/N_o and multipath (Mezentsev 2005). Such problems cause large measurement errors that can introduce a bias in the estimated parameters, thus compromising system integrity (Petovello 2003). On the contrary, in simulation analysis the GPS data before and after the simulated outage is mostly clean and fault free; so, the results obtained by simulation of a GPS outage, are likely to be optimistic relative to the actual performance of standalone INS in urban canyon environments (Godha et al 2005).

Some studies that focused on evaluating the performance of an integrated system in signal degraded environments include Sukkarieh (2000), Petovello (2003), and Salycheva (2004). All of these studies were limited in terms of the operational environment, the type of IMU used, and the application considered. For instance, Sukkarieh (2000) specifically looked at the integration of a medium accuracy INS with DGPS, for an application involving the navigation of straddle carriers which are slow moving vehicles (<10 m/s). Petovello (2003) and Salycheva (2004) looked at the performance of an integrated system in pseudo-urban and urban environments, respectively; however, the IMU used for the study was a high cost (from an LVNS design stand point), tactical grade, IMU. Recently, Hide & Moore (2005) directed some work towards evaluating a DGPS/MEMS INS integrated system in urban environments, where a tightly coupled integration scheme was used for integration. The integrated system in this case was shown to provide a few metre level accuracies.

1.4 Objectives

Given the lack of research being directed towards the integration of a low cost/performance MEMS INS, this thesis expands upon the work described in the previous sections. The specific objectives of this thesis are:

1. *To analyze the performance of DGPS/MEMS INS system using closed loop loosely and tightly coupled integration schemes*. The MEMS IMU being used is the Crista IMU from Cloud Cap Technology Inc., and the GPS receiver used is the NovAtel

OEM4 receiver. The performance of the system will be evaluated during complete GPS availability, partial GPS outages, and complete GPS outages.

2. *To investigate the performance improvements achievable in a DGPS/MEMS INS integrated system through the use of vehicle motion constraints, during GPS outages*. Specifically, two kinds of constraints are used, the vehicle velocity constraints and the height constraints. The performance of the system will be quantified using both constraints individually and simultaneously, and the improvements will be assessed through comparison with the case when no constraints are used.

3. *To investigate the performance improvements that a backward smoothing technique, specifically the RTS smoother, can provide*. The smoother performance with DGPS/MEMS INS integrated system will be assessed during complete GPS availability and complete outages.

4. *To asses the relative difference in the performance of MEMS IMU and a tactical grade IMU, under similar operating conditions*. The tactical grade IMU being used is a Honeywell HG1700 IMU. Each of the above stated tasks will also be carried out with the HG1700 IMU. The specific aim is to provide a rigorous quantitative analysis of performance differences between two different grades of IMUs using side-by-side testing.

5. *To evaluate the performance of the systems in different operating environments, specifically open, semi-urban and urban areas*. One data set collected in each environment will be used to asses the performance of both MEMS and tactical grade IMUs based DGPS/INS integrated system.

1.5 Research Methodology Summary

The following methodology has been carried out to meet the objectives outlined in the previous section:

1. *Error characterization of MEMS IMU*: The first step in the development of an integrated system is the error characterization of the IMU. This basically focused on examining the deterministic error sources (turn-on bias and scale factor), obtaining the high-frequency noise power (sensor noise), and analyzing the low-frequency sensor drifts (in-run bias drift) present in the MEMS sensors. Based on the drift error characteristics, a suitable stochastic model and the corresponding parameters were chosen to model the errors in a Kalman filter.

2. *Implementation of INS mechanization for strapdown INS*: This is a basic step in all INS processing. The INS mechanization was implemented to convert the raw sensor angular and velocity increments into useful navigation information.

3. *GPS processing*: This step involved implementation of a GPS filter to compute the navigation solution from GPS measurements, in differential mode. Two different

differential processing modes were implemented, single differenced and double differenced; however, this thesis deals only with the single differencing method.

4. *Implementation of integration algorithms*: This is the step where the navigation solutions from the GPS and INS are fused together to obtain a blended solution. Both loosely coupled and tightly coupled integration strategies were implemented using a closed loop approach. An augmented state Kalman filter is developed for integration of the MEMS INS with GPS for effective sensor error compensation. The specific advantage of such a filter is that the inertial sensor raw measurements could be corrected for deterministic errors (which vary on each turn-on) more efficiently.

5. *Implementation of (error compensation) algorithms to bridge GPS data outages*: This step involved the development and implementation of different algorithms to prevent INS error degradation during GPS outages. Methods such as vehicle motion constraints and backward smoothing are used.

6. *Software development*: All the integration strategies, INS filters, GPS filters, error compensation algorithms, and backward smoothing techniques are implemented in software developed in C++. The software is a post-processing package, although most of the implemented algorithms are adaptable to real-time applications, with an exception of the smoothing technique.

7. *Field tests and data analysis:* The final step of this research was to undertake field tests and data processing. Simultaneous field testing was conducted with different grades of IMUs, different GPS receivers, and magnetometers. The analysis involved interpreting the results obtained from open, semi-urban and urban areas.

1.6 Outline

Chapter Two provides an overview of the GPS and INS systems. Various GPS error sources along with differential GPS methods to reduce measurement errors are discussed. Following this discussion, the inertial navigation system in introduced, along with a discussion of its equations of motion, inertial sensor errors, and alignment techniques.

Chapter Three provides an overview of estimation methods and discusses the Kalman filter algorithm. It also provides a brief overview of the innovations-based outlier detection scheme used in this work.

Chapter Four discusses different integration strategies and approaches for blending GPS and INS. It then provides the designs of the GPS and the INS filters developed in this study. Finally, it discusses the algorithms for compensating errors in the INS mechanized navigation solutions during GPS outages.

Chapter Five and Chapter Six provides the field tests descriptions and presents the performance testing results of both DGPS/MEMS INS and DGPS/tactical INS integrated system in the open, semi-urban and urban areas. Results obtained using different

integration strategies, different INS filters, and under different GPS conditions are presented. The impact of vehicle motion constraints under partial and complete GPS outages is also evaluated.

Chapter Seven provides a brief introduction to smoothing techniques followed by a discussion about the RTS smoother. It then presents some test results in open and urban areas.

Chapter Eight summarizes the work presented in this thesis, and draw conclusions from the test results and analysis. Finally, several recommendations for future work are outlined.

CHAPTER TWO : GPS AND INS SYSTEM OVERVIEW

This chapter discusses the fundamentals of GPS and INS systems. An overview of GPS will be provided first, along with a discussion of various error sources that affect GPS measurements. Differential GPS methods used to mitigate these errors will be discussed. The latter half of this chapter discusses inertial navigation concepts including the mechanization equations, inertial sensor errors, and the alignment procedure.

2.1 Global Positioning System

GPS, officially also known as NAVSTAR (Navigation System with Timing and Ranging), is an all weather, worldwide, satellite-based navigation system developed by the U.S. Department of Defense (DoD) (Hofmann-Wellenhof et al 1992). It belongs to a large class of radio navigation systems that allow the user to determine range from a known signal transmitting station by measuring the differential time of travel of the signal. GPS receivers take this information and use trilateration to calculate the user's position.

The GPS system consists of three segments: the space segment, the control segment, and the user segment. The space segment consists of satellites which continuously broadcast signals. As of September 23, 2005, there are 29 functional GPS satellites in orbit (www.navcen.uscg.gov/ftp/GPS/status.txt). These satellites orbit the Earth in six 12-hr (11-hr, 58-min) orbital planes. The control segment deals with monitoring the health of the satellites and uploading navigation data (Misra & Enge 2001). It consists of a system of tracking stations located around the world, including six monitor stations, four ground

antennas, and a master control station. The user segment is by far the largest and the most dynamic segment of the GPS, which consists of the antennas and receiver-processors that measure and decode the satellite transmissions to provide positioning information to the user (Farrell & Barth 2001). Originally designed for the military users, GPS is now being used extensively in applications intended for civilian users. In-fact, the civilian users constitute a major portion of the user segment, where the estimated number of civilian users is around few million and is growing every year (Lachapelle 1995). A schematic representation of each GPS segment is shown in Figure 2.1.

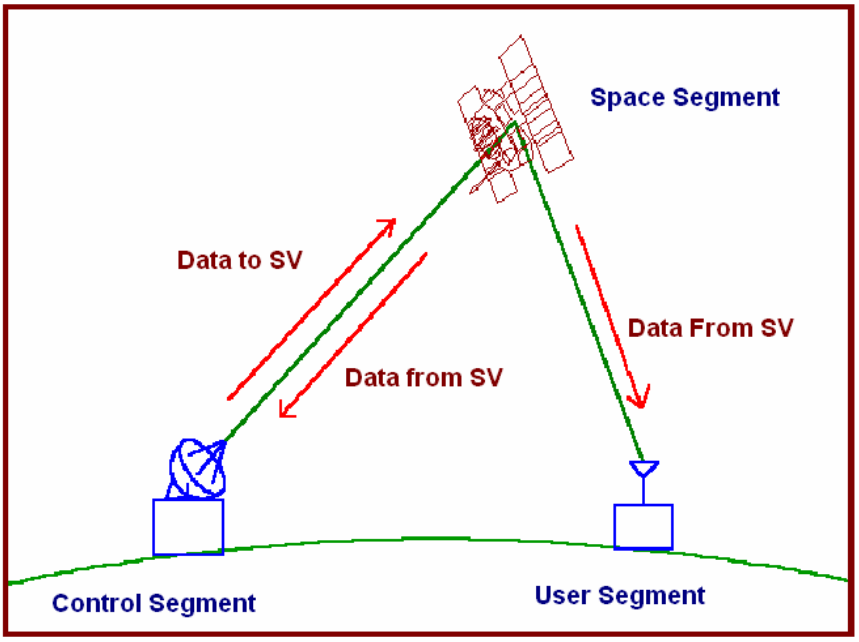

Figure 2.1: Schematic Representation of GPS Segments (Dana 1994)

The GPS is a spread spectrum Code Division Multiple Access (CDMA) system that broadcasts bi-phase modulated Right Hand Circularly Polarized (RHCP) signals at two carrier frequencies: L1 (1575.42 MHz) and L2 (1227.60 MHz). These signals are modulated by two Pseudo-Random Noise (PRN) codes, the Coarse-Acquisition (C/A)

code on L1 and the P-code on both L1 and L2**.** The access to P-code is restricted only to military users via its encryption by a Y code, a technique termed as anti-spoofing. The PRN code for each satellite is unique which allows a receiver to discriminate between satellites. Each satellite vehicle (SV) is identified by its respective PRN code number. In addition to these PRN codes, the navigation message consisting of information such as satellite ephemeris, satellite clock bias and satellite status is also modulated onto the L1 and L2 carriers.

A single-frequency civilian user can obtain three types of measurements from the currently available GPS signal. These are: (1) Code phase (pseudorange) measurement; (2) Carrier phase measurement; and (3) Doppler/incremental phase measurement. With the GPS modernization plan, the new signal on L2 frequency (L2C) will become available for civilian use which will allow constructing additional measurements (Fontana et al 2001). This signal, however, is likely to be 'fully available' (i.e. on all satellites) by the year 2011. The carrier phase measurement is the most precise measurements available to GPS users, and is typically used in high-accuracy (cm-level) application such as geodetic surveying, and automatic vehicle applications. However, typical accuracy requirements in land vehicle navigation application are on the order of few metres. In an open area environment, GPS pseudorange measurements can provide accuracies better than 5 m in differential mode for a baseline length of 50 km from reference station (Misra & Enge 2001). Thus, in this research, only pseudorange (L1-C/A) and Doppler measurements are utilized, the details of which are provided in the following sections.

2.1.1 Pseudorange Measurements

The code pseudorange measurement represents the apparent distance between the GPS satellite and the receiver antenna. These measurements are derived from the PRN codes, by measuring the amount of time shift required to align the PRN-code replica generated at the receiver with the one received from the satellite (Hofmann-Wellenhof et al 1992). Using this information the GPS receiver determines the time required for the signal to propagate from the satellite to the receiver, which when scaled by the speed of light provides the pseudorange measurement. These measurements are termed as pseudoranges instead of ranges because the clocks of the satellites and the receiver are not perfectly synchronized to GPS time. The measurements therefore contain clock biases; hence, the term *pseudo.*

The *true* pseudorange is the pseudorange in the idealized error-free condition, which includes the true range and the clock error bias. However, in real measurements there are random noise effects, and various propagation and system specific errors. The measured pseudorange, thus, is generally expressed by Equation (2.1) (Lachapelle 2003):

$$p(t) = \rho(t) + cdt(t) - cdT(t) + d_{orb}(t) + d_{ion}(t) + d_{trop}(t) + \eta_p \tag{2.1}$$

where, (t) represent the variable value at time 't'. The symbol:

p is the measured pseudorange (m),

ρ is the true range between satellite and the receiver antenna (m),

dt is the satellite clock error (s),

dT is the receiver clock error (s),

d_{orb} is the satellite orbital error (m),

d_{ion} is the ionospheric error (m),

d_{trop} is the tropospheric error (m) ,

η_p is the error because of multipath and noise (m), and

c is the speed of light in vacuum (m/s).

A brief overview of the above mentioned error sources will be provided in Section 2.1.3, while a more detailed treatment of each error source can be found in Parkinson & Spilker (1996), Kaplan (1996), and Misra & Enge (2001).

Pseudorange measurements are useful in determining a user's position in terms of latitude, longitude, and height (all referenced to the WGS84 ellipsoid). These three unknowns combined with the receiver clock error term, results in a total of four unknown parameters (Farrell & Barth 2001). Thus, independent GPS navigation requires signals from at least four satellites for computation of a complete position solution. However, with clock aiding, it is possible to navigate with less than four satellites (Zhang 1997). Augmenting GPS with clock and height aiding requires only as few as two satellites measurements to provide the navigation solution (ibid).

2.1.2 Doppler Measurements

The Doppler frequency represents the rate of change of the carrier phase observable, and is typically measured in L1 cycles per second (Hz). These measurements, when scaled by

the L1 wavelength, provide the range rate measurement. This observable can be expressed by Equation (2.2) (Lachapelle 2003):

$$\dot{p}(t) = \dot{\rho}(t) + cd\dot{t}(t) - cd\dot{T}(t) + \dot{d}_{orb}(t) - \dot{d}_{ion}(t) + \dot{d}_{trop}(t) + \eta_{\dot{p}} \tag{2.2}$$

where, (t) represent the variable value at time 't'. The symbol:

$\dot{p}$ is the observed range rate derived from Doppler measurements (m/s),

$\dot{\rho}$ is the true range rate between the satellite and the receiver (m/s),

$d\dot{t}$ is the satellite clock drift,

$d\dot{T}$ is the receiver clock drift,

$\dot{d}_{orb}$ is the satellite orbital drift error (m/s),

$\dot{d}_{ion}$ is the ionospheric error drift (m/s),

$\dot{d}_{trop}$ is the tropospheric error drift (m/s) , and

$\eta_{\dot{p}}$ is the drift error because of multipath and noise (m/s).

The range rate reflects the relative velocity between the receiver and the GPS satellite, and thus can be used for computing velocities.

2.1.3 GPS Errors and Mitigation

GPS error sources can be classified into the common mode errors and the non-common mode errors. The non-common mode errors are those that could be distinct to receivers operating even in close proximity (Farrell & Barth 2001), and includes receiver specific errors such as clock errors, multipath and noise. The common mode errors are error sources such as satellite clock error, orbital error, ionospheric error and tropospheric

error, which exhibits spatial correlation and are common to every receiver operating in a limited geographic region. Given this property, the common mode error can be reduced to small values using DGPS techniques (Misra & Enge 2001).

DGPS involves a GPS receiver/antenna at a known location (reference station), a receiver at an unknown location (rover station), possible changing positions, and a communication medium between the two if real-time positioning is desired (Farrell & Barth 2001). The underlying principle is to compute the measurement differences for a particular PRN at reference and rover station, which reduces the effect of the common mode errors. Then, with the knowledge of the precise reference station position, the position of rover station can be computed using the differenced measurements. The concept is explained graphically in Figure 2.2.

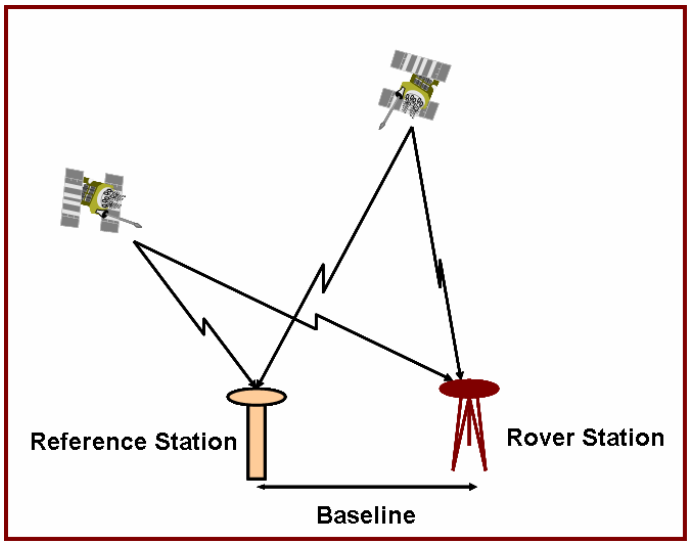

Figure 2.2: Differential GPS Concept

Three different DGPS techniques exist, namely the single-difference (SD), the double-difference (DD) and the triple-difference (TD), out of which SD and DD are used most

commonly. To this end, SD is preferred approach when only pseudorange and Doppler measurements are involved in GPS computations. The primary reason for this is that the non-common mode errors (i.e. receiver noise and multipath) tend to get amplified in DGPS techniques, because of their non-spatially correlated characteristics. The amplification is greater in DD (or TD) relative to SD. Thus, in the context of this thesis the common mode errors are mitigated using the SD technique. This technique can be implemented using two methods (Lachapelle 2003):

- Differencing between receivers – eliminates satellite-specific errors, and
- Differencing between satellites – eliminates receiver-specific errors.

Here, differencing between the two receivers is used whereby measurements at the reference and the rover stations are subtracted, for a particular satellite. The corresponding pseudorange and Doppler measurements are represented by Equations (2.3) through (2.5) (Misra & Enge 2001):

$$\Delta = (*)_{rover} - (*)_{reference} \tag{2.3}$$

$$\Delta p(t) = \Delta\rho(t) + c\Delta dT(t) + \Delta d_{orb}(t) + \Delta d_{ion}(t) + \Delta d_{trop}(t) + \eta_{\Delta} \tag{2.4}$$

$$\Delta \dot{p}(t) = \Delta\dot{\rho}(t) + c\Delta d\dot{T}(t) + \Delta \dot{d}_{orb}(t) + \Delta \dot{d}_{ion}(t) + \Delta \dot{d}_{trop}(t) + \dot{\eta}_{\Delta} \tag{2.5}$$

The advantage of forming such an observable is that the satellite clock errors get eliminated completely, while the satellite orbital errors and the propagation errors due to the ionosphere and troposphere get reduced significantly. Since the errors are reduced, the quality of the measurement is improved, which ultimately leads to an improved positioning accuracy relative to the stand-alone GPS case (Farrell & Barth 2001).

However, high accuracies can be achieved in differential mode only if the baseline between the reference and rover station is small, in which case the measured ranges are affected by these errors in similar proportions (Hoffman-Wellenhoff et al 1992). With increasing baselines, the spatial correlation between the errors weakens, leading to relatively large residual errors which degrade the accuracy of the obtainable solution. Since only satellite specific errors are reduced in 'between receiver' differencing, the receiver clock error needs to be included in the GPS computations as an unknown. Further details of the remaining error sources and the effect of their residual errors after differencing are discussed in the following sections.

2.1.3.1 Satellite Orbital Error (d_{orb})

The satellite orbital errors are the discrepancies between the true satellite positions and the computed values. The satellite orbits are monitored continuously from several monitoring stations around the Earth and the predicted orbital information is transmitted to the satellites, which in turn is transmitted to the receivers as the part of the navigation message (Zumberge & Bertiger 1996). The accuracy of these predictions is limited as there are a maximum of three satellite uploads per day.

The orbital errors are correlated for two receivers and thus can be damped by differencing between two receivers (Misra & Enge 2001). However, since the effective range error due to orbital errors is line-of-sight dependent, the ability of differential techniques to compensate for orbital errors is dependent on the user position relative to the reference

station. Typically, for a baseline length of 100 km, the residual orbital error after differencing remains less than 5 cm (ibid).

2.1.3.2 Ionospheric Error (d_{ion})

The ionosphere is the layer extending from a height of about 50 km to about 1000 km that consists of ionized air (free electrons and ions). The ionization of the air is caused by the sun's radiation and thus the physical characteristics of the ionosphere change widely between day and night (Misra & Enge 2001). The presence of free electrons affects the refractive indices of the various layers of the ionosphere, and thus the GPS signals do not travel at the vacuum speed of light as they pass through this region (Farrell & Barth 2001). The change in velocities ultimately results in phase advance and code delay. This however, is dependent on Total Electron Content (TEC) over the signal path (Hoffmann-Wellenhoff et al 1992).

Due to their spatial correlation, the ionospheric error gets reduced by differential techniques. However, the post-differential residual errors depend upon the spatial variability of the TEC in the ionosphere (Misra & Enge 2001). In fact, the ionosphere can show considerable variability both spatially and temporally resulting from the solar activity and magnetic storm-induced traveling disturbances (ibid). For a satellite overhead, the residual error after differential corrections is typically on the order of 5-20 cm for a baseline length of 100 km, but can be up to 1 m if the ionosphere is active (ibid).

2.1.3.3 Tropospheric Error (d_{trop})

The troposphere is the neutral region of the Earth's atmosphere extending from the Earth's surface up to 50 km. When GPS signals propagate through the troposphere, they experience range delays dependent on the pressure, temperature and moisture content along the signal path (Shreshtha 2003). These delays are normally represented to have a wet component and a dry component (Farrell & Barth 2001). The dry part results from the dry gases in the troposphere while the wet part results from the water vapour. About 90 % of the tropospheric delay arises from the dry component, which can be predicted with an accuracy of about 1 %, while the rest 10 % is the contribution from the wet component (Hoffmann-Wellenhoff et al 1992). The wet component is difficult to predict, since water vapour density varies with the local weather and can exhibit drastic variations, and thus the prediction accuracy is only about 10-20 % (ibid).

The ability of differential techniques to compensate for tropospheric effects depends on the inter-receiver separation, as receivers separated by several kilometres may be subject to different weather conditions. Specifically, the water vapour content can show considerable variability both spatially and temporally. Thus, the residual errors for a baseline length of 100 km can be in the range of 10-15 cm (Misra & Enge 2001). Residual errors are generally higher for satellites at lower elevation angles.

2.1.3.4 Receiver Clock Error (dT)

This error is the offset of the receiver clock with respect to the reference GPS time. It is a time-varying error that affects all simultaneous range measurements in the same fashion,

at a particular epoch. Therefore, if measurements from four satellites are available, these errors can be estimated in GPS computations (Farrell & Barth 2001). Another option is to compute 'between satellite' differences, which eliminates this error completely. In this work, receiver clock error is included as an unknown parameter in the GPS computations.

Typical receiver clock errors may vary from a few metres to few thousand kilometres, depending on the quality of the oscillator used in a GPS receiver. It is very common for these crystal oscillators to have some error in frequency, which give rise to a drift characteristic in the clock error (Brown & Hwang 1997).

2.1.3.5 Multipath

Multipath refers to the phenomenon of a signal reaching an antenna via two or more paths along with the direct line-of-sight (LOS) GPS signal (Misra & Enge 2001). A land vehicle typically moves in urban environment which generally comprises of reflectors of the electromagnetic signals, such as buildings (glassy), metal surfaces etc., as shown in Figure 2.3. Multipath may therefore be the single most dominant source of errors in satellite-based vehicle navigation systems. Multipath signals are always delayed since they travel longer distances than LOS signal. The time delay is entirely dependent upon the geometry of the environment in which the receiver is located (Braasch 1996). Multipath can introduce both negative and positive error on the pseudorange measurement depending on the phase of the multipath signal.

Multipath affects both the code and the carrier phase measurements but the magnitudes of the error differ significantly (Misra & Enge 2001). The code multipath can vary from ±1 m in favourable conditions to few tens of metres in highly reflective environments. The maximum range error possible on GPS code signals is limited to ±150 m in the case of line-of-sight signals (Parkinson & Spilker 1996). For the non line-of-sight signals (also called the echo-only signals), this error is much greater than ±150 m which depends entirely on the reflected signal geometry (Macgougan 2003). The phase measurements error due to multipath generally does not exceed 4.75 cm (Ray 2000). Since Doppler measurements are derived from the rate of phase change, the effect of multipath on GPS velocity measurements is very small (Syed 2005). A detailed analysis on the effects of multipath on GPS observables can be found in Ray (2000).

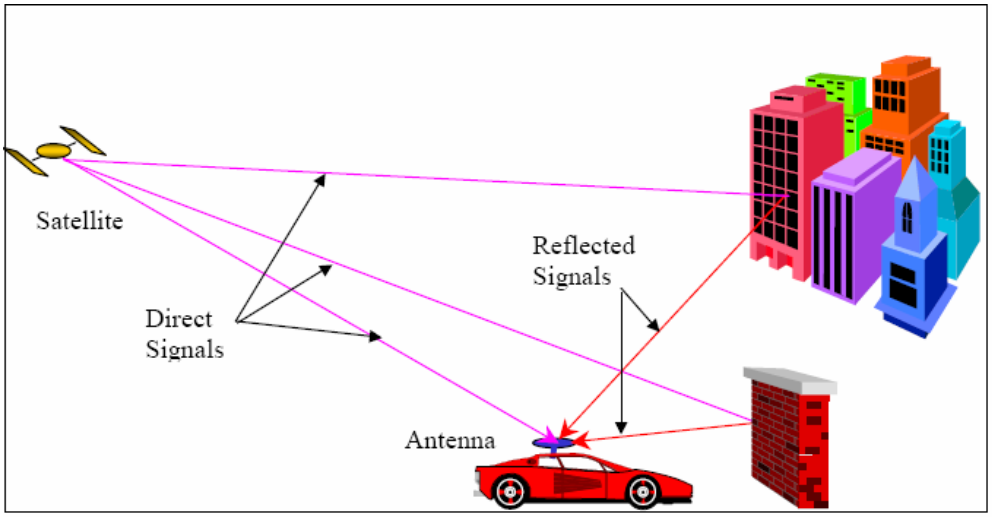

Figure 2.3: Multipath Environment (Nayak 2000)

Since multipath is a highly localized phenomenon, with very low spatial and temporal correlation, it can not be reduced by differential techniques (Ray 2000). Numerous,

techniques have been developed for mitigating multipath based on the design of receiver and antenna designs. The effect of multipath can be reduced in antenna design process by lowering the contributions of some type of reflections (Misra & Enge 2001). One of the most effective techniques based on design of receiver architecture is Narrow Correlator technique, which is well described in van Dierendonck et al (1992).

In the context of this work, multipath is dealt through integration with inertial sensors. GPS measurements are subject to the innovation based statistical testing, where any inconsistencies in GPS measurement (possibly due to multipath) relative to navigation information from inertial sensors, is detected and rejected from the computational processing for the navigation solution.

2.1.3.6 Receiver Errors

Receiver error includes the contributions from the thermal noise error and the effects of dynamic stress on the tracking loops (Ward 1996). The magnitude of this error is dependent on the technology incorporated in a particular receiver (Farrell & Barth 2001). In high quality receivers, these errors are negligible for carrier phase and a few decimetres for code phase. The GPS receiver noise can typically be assessed through a zero-baseline test, where the two receivers are connected to a single antenna using a signal splitter (Hoffmann-Wellenhof et al 1992).

In order to characterize the measurement noise of the GPS receiver (being used in this study), a zero-baseline test was carried out with two NovAtel OEM4 receivers. A total of

sixteen hours of static data was collected with each receiver on the roof of Calgary Centre for Innovative Technology (CCIT) building. Double differenced (DD) measurements were computed, where the highest elevation satellite was used as a reference satellite for computations. Double differencing removes all the significant error sources, with only errors left being the receiver specific errors and multipath. The observations were divided into separate bins, based on the satellite elevation angles (2˚ bin size). The standard deviation of the un-differenced noise was then calculated using the obtained double-differenced measurements (Raquet 1998). Figure 2.4 shows the computed code and Doppler noise power as a function of elevation angle.

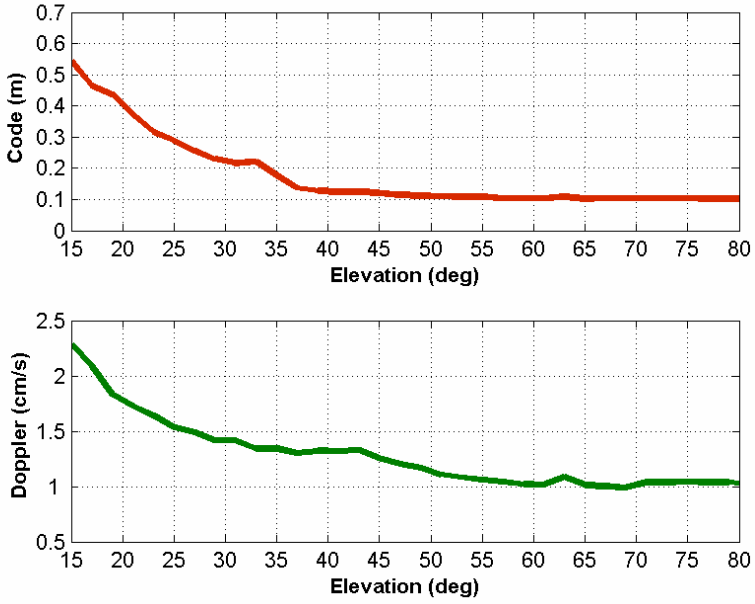

Figure 2.4: Receiver Noise Power in OEM4 Receivers

The OEM4 is a high quality geodetic grade receiver, which provides very low noise C/A code and Doppler measurements (Petovello et al 2003). From Figure 2.4 it can be seen that for elevation angles greater than 45˚, the noise power is around 10 cm, while below that it goes up to 50 cm. The values seen here are relatively lower than that shown in

Petovello (2003), but agree well with the ones shown in Lachapelle (2003). The results with Doppler observations show cm/s-level accuracy. However, it should be noted that the data for these computations was collected under benign operational conditions, where multipath effects are minimal. Under more adverse conditions, the effect of multipath can reach several metres even with high-quality GPS receivers (Ray 2000).

Since noise is a receiver-specific phenomenon, it cannot be reduced by differential techniques. In-fact, this error gets amplified by a factor of $\sqrt{2}$ for differential measurements (single differenced) (Lachapelle 2003).

2.1.3.7 GPS Error Summary

The contribution from each of the error sources into the GPS measurement is listed in the Table 2.1. The differential errors are specified in parts per million (PPM), where 1 PPM implies 1 mm error for a baseline of 1 km.

Table 2.1: GPS Pseudorange Error Sources (Misra & Enge 2001)

Error Source	***Single Point***	***Differential Errors***
	(m)	***(PPM)***
Orbital	3 – 5	0.1 – 0.5
Satellite Clock	2 – 3*	–
Ionosphere	2 – 50	0.5 – 2
Troposphere	2 – 30	1 – 1.5
Code Multipath	0.2 – 3**	–
Code Noise	0.1 – 2	–

* After application of broadcast clock corrections

** Under benign operating conditions

2.2 Inertial Navigation System (INS)

An INS is a self-contained Dead Reckoning (DR) navigation system, which provides dynamic information about position and velocity, based on the measurements obtained from an Inertial Measurement Unit (IMU) (Jekeli 2001). An IMU consists of three accelerometers and three gyros mounted on an orthogonal triad. The basic operating principle of inertial navigation is based on Newton's law of motion, which says that an object continues to be in a state of rest or uniform motion, unless acted upon by an external force. The application of any external force generates the acceleration, which is sensed by accelerometers contained in an IMU. This acceleration, when integrated twice, provides the change in the state of the object with respect to the initial conditions. Thus, an INS generically provides the *change* in the state of the object, and the knowledge of the initial condition (position, velocity and attitude) of the platform prior to the start of the navigation is essential for its operation (El-Sheimy 2004).

However, the computation process is more complicated then it sounds because of the fact that the IMU provides measurements in a coordinate frame different than the coordinate frame in which position and velocity are usually expressed (Mathur 1999). This is what drives the need of gyros in an INS, which provides angular measurements to be able to transform the sensed acceleration to an appropriate frame, prior to integration. It follows that the accuracy of the angular measurements is fundamental to an INS, because any errors in transformation of acceleration will ultimately lead to errors in position. Thus, the ability of an INS to enable the continuous determination of vehicle position, velocity and attitude, primarily depends on the quality of gyro sensors used (El-Sheimy 2004).

2.2.1 Coordinate Frames and Transformations

The INS developed in this research typically requires transformations between four coordinate systems, which are defined below. These definitions follow from El-Sheimy (2004).

An Inertial Frame (i-frame) is a non-rotating and non-accelerating frame with respect to fixed stars. The inertial frame is defined as follows:

Origin : Earth's centre of mass

Z^i-Axis : Parallel to the spin axis of the Earth

X^i-Axis : Pointing towards the mean vernal equinox

Y^i-Axis : Orthogonal to X and Z completing a right-handed system

An Earth Centered Earth Fixed (ECEF or e-frame) is defined as follows (Figure 2.5):

Origin : Earth's centre of mass

Z^e-Axis : Parallel to the mean spin axis of the Earth

X^e-Axis : Pointing towards the mean meridian of Greenwich

Y^e-Axis : Orthogonal to the X and Z axes to complete a right-handed frame

The Local Level Frame (LLF or l-frame) is a local geodetic frame (Figure 2.5) and is defined as follows:

Origin : Coinciding with sensor frame

Z^l-Axis : Orthogonal to reference ellipsoid pointing Up

X^l-Axis : Pointing towards geodetic East

Y^l-Axis : Pointing toward geodetic North

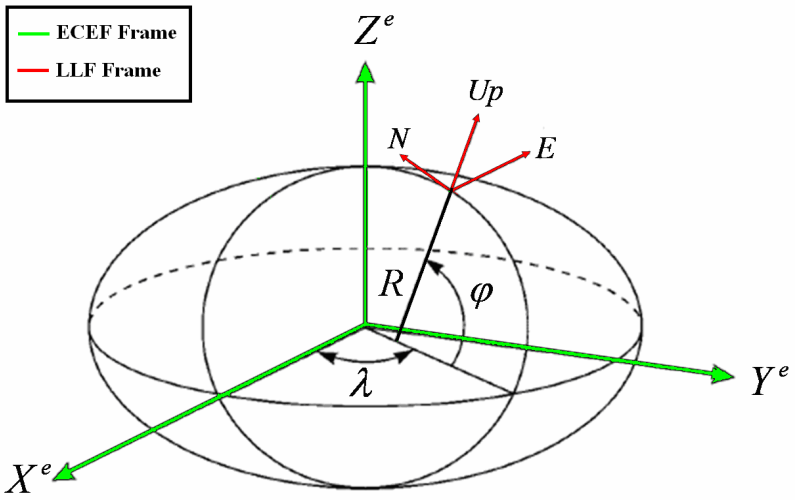

Figure 2.5: ECEF and LLF Frame (adapted from Salychev 1998)

A Body Frame (b-frame) is an orthogonal frame, whose axes coincide with the axis of the IMU. The body frame is assumed to be aligned with the vehicle frame (Figure 2.6), and is defined as follows:

Origin : Centre of the IMU

X^b-Axis : Pointing towards the right of the vehicle

Y^b-Axis : Pointing towards the front of the vehicle

Z^b-Axis : Orthogonal to the X and Y axes to complete a right-handed system

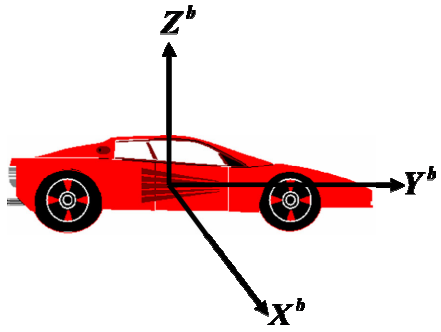

Figure 2.6: Body Frame (b-frame)

The transformation between e-frame and l-frame can be performed by two consecutive rotations around the X^e and Z^e axes, and is given by Equation (2.6):

$$R_e^l = \left(R_l^e\right)^T = R_1(90^\circ - \varphi)R_3(\lambda + 90^\circ) \tag{2.6}$$

where, superscript 'T' means the transpose. The symbol,

φ is the latitude,

λ is the longitude,

R_e^l is the rotation matrix from e-frame to l-frame, and

R_i is the rotation matrix about the i^{th} axis.

The transformation between b-frame and l-frame can be performed by three consecutive rotations around Z^b, X^b and Y^b, and is assumed to be defined by Equation (2.7):

$$R_b^l = \left(R_l^b\right)^T = R_3(\psi)R_1(-\eta)R_2(-\xi) \tag{2.7}$$

where,

ψ is the heading of the vehicle,

η is the pitch of the vehicle,

ξ is the roll of the vehicle, and

R_b^l is the rotation matrix from b-frame to l-frame.

Thus, the corresponding transformation between the b-frame and e-frame can be carried out from the multiplication of Equation (2.6) and Equation (2.7), and is given by Equation (2.8):

$$R_b^e = (R_e^l)^T \times R_b^l = R_l^e \times R_b^l \tag{2.8}$$

where R_b^e is the rotation matrix from b-frame to e-frame.

2.2.2 Mechanization Equations

Mechanization equations are the set of equations used to convert the specific force (f^b) and angular velocity (ω^b) measurements obtained from an IMU into useful position, velocity and attitude information (Savage 2000). In the context of this work, the mechanization is implemented in ECEF frame. The discussion below follows from El-Sheimy (2004).

The integration of the raw data obtained from the IMU is done in two steps. In the first step, the body sensed angular rates are integrated to compute the transformation matrix (rotation matrix) from b-frame to e-frame. A gyro senses the angular rates due to Earth rotation and the rotation due to vehicle movement. To get the actual vehicle angular velocity, Earth rotation rate should be transformed into the body frame, and removed from the measured angular rates. Once the angular rate is obtained, a transformation matrix (R_b^e) can be computed using a quaternion approach.

In the second step, the computed transformation matrix (R_b^e) is used to rotate the measured specific force from the b-frame to e-frame. The output of an accelerometer represents the sum of actual vehicle acceleration and the gravity. The sensed acceleration information must therefore be compensated for gravity in order to determine the total acceleration of the vehicle. This acceleration can then be integrated to obtain vehicle velocity, which when integrated provides the vehicle position.

The above discussed procedure in mathematical terms is stated by Equation (2.9) (El-Sheimy 2004):

$$\begin{bmatrix} \dot{r}^e \\ \dot{v}^e \\ \dot{R}_b^e \end{bmatrix} = \begin{bmatrix} v^e \\ R_b^e \left\langle f^b \right\rangle - 2\Omega_{ie}^e v^e + \gamma^e \\ R_b^e (\Omega_{ei}^b + \left\langle \Omega_{ib}^b \right\rangle) \end{bmatrix} \tag{2.9}$$

where, 'dots' denotes the time derivative, the superscript '*e*' and '*b* ' represents the values in e-frame and b-frame, respectively. The symbol,

r^e is the position vector (x^e, y^e, z^e),

v^e is the velocity vector (v_x^e, v_y^e, v_z^e),

γ^e is the gravity vector $(\gamma_x^e, \gamma_y^e, \gamma_z^e)$,

R_b^e is the rotation matrix from b-frame to e-frame,

Ω_{ei}^b is the skew-symmetric matrix of the rotation rate w_{ei}^b,

Ω_{ib}^b is the skew-symmetric matrix of the rotation rate w_{ib}^b.

The values within the braces '$\langle\ \rangle$' in Equation (2.9) are the measurement inputs to the system, obtained from an IMU. The above system of equations can essentially be solved in a four-step process, as discussed in the following sections (ibid).

2.2.2.1 Correction of the Raw Data

The inputs to the computational process are the angular increments ($\Delta\widetilde{\theta}_{ib}^b$), and the velocity increments ($\Delta\widetilde{v}_f^b$). Most low-cost IMUs output accelerations and angular velocities, which can be scaled to obtain velocity and angular increments. These raw

measurements are typically corrupted by errors such as turn-on bias, in-run bias, scale factor errors and other misalignment errors (Park et al 2002, Hou 2004). Specific details about each of these sensor errors are provided in Section 2.2.3. The values for these errors can either be obtained from lab-calibration procedures, or it can be estimated in a Kalman filter (which is discussed in Chapter Four).

Once the sensor errors are obtained, the measurements can be corrected using Equations (2.10) and (2.11) for gyros and accelerometers, respectively:

$$\Delta\theta_{ib}^{b} = \frac{(\Delta\widetilde{\theta}_{ib}^{b} - b_g \Delta t)}{(1 + S_g)} \tag{2.10}$$

$$\Delta v_{f}^{b} = \frac{(\Delta\widetilde{v}_{f}^{b} - b_a \Delta t)}{(1 + S_a)} \tag{2.11}$$

where, '$\sim$' represents the raw measurements. The symbol:

b_a, b_g are the bias instabilities and turn-on bias for each sensor,

S_a, S_g are the scale-factor errors for each sensor, and

Δt is the time increment $(t_{k+1} - t_k)$.

2.2.2.2 Attitude Update

As stated earlier, the total angular increment obtained from a gyro is the combination of the vehicle's rotation and the rotation of the navigation frame (e-frame) relative to inertial space. The angular increments due to the Earth's rotation rate in body frame can be computed using Equation (2.12):

$$\Delta\theta_{ie}^{b} = R_{e}^{b}\omega_{ie}^{e}\Delta t = R_{e}^{b}\begin{bmatrix} 0 \\ 0 \\ \omega_{e} \end{bmatrix}\Delta t \tag{2.12}$$

where ω_e is the Earth's rotation rate (15.041˚/h).

Thus, the angular increment due to body rotation with respect to the e-frame can then be obtained by Equation (2.13):

$$\Delta\theta_{eb}^{b} = \Delta\theta_{ib}^{b} - \Delta\theta_{ie}^{b} \tag{2.13}$$

The computation of the 'new' rotation matrix, R_e^b, from the angular increments (obtained from Equation (2.13)), is usually done using a quaternion approach. In this approach, the rotation matrix is expressed by a single rotation angle (θ) about a fixed spatial axis. For a comprehensive discussion about quaternions, readers are referred to Savage (2000). The rotation matrix can thus be updated using computed angular increments $\Delta\theta_{eb}^{b}$ ($\Delta\theta_x^b, \Delta\theta_y^b, \Delta\theta_z^b$), as stated in Equation (2.14):

$$\begin{bmatrix} q_1 \\ q_2 \\ q_3 \\ q_4 \end{bmatrix}_{k+1} = \begin{bmatrix} q_1 \\ q_2 \\ q_3 \\ q_4 \end{bmatrix}_{k} + \frac{1}{2}\begin{bmatrix} c & s\Delta\theta_z^b & -s\Delta\theta_y^b & s\Delta\theta_x^b \\ -s\Delta\theta_z^b & c & s\Delta\theta_x^b & s\Delta\theta_y^b \\ s\Delta\theta_y^b & -s\Delta\theta_x^b & c & s\Delta\theta_z^b \\ -s\Delta\theta_x^b & -s\Delta\theta_y^b & -s\Delta\theta_z^b & c \end{bmatrix}\begin{bmatrix} q_1 \\ q_2 \\ q_3 \\ q_4 \end{bmatrix}_{k} \tag{2.14}$$

where, $s = \frac{2}{\theta}\sin\left(\frac{\theta}{2}\right)$, $c = 2\cos\left(\frac{\theta}{2} - 1\right)$, and $\theta = \sqrt{(\Delta\theta_x^b)^2 + (\Delta\theta_y^b)^2 + (\Delta\theta_z^b)^2}$

Having obtained the updated quaternion, the updated rotation matrix can thus be computed using Equation (2.15):

$$(R_b^e)_{k+1} = \begin{bmatrix} (q_1^2 - q_2^2 - q_3^2 + q_4^2) & 2(q_1q_2 - q_3q_4) & 2(q_1q_3 + q_2q_4) \\ 2(q_1q_2 + q_3q_4) & (q_2^2 - q_1^2 - q_3^2 + q_4^2) & 2(q_2q_3 - q_1q_4) \\ 2(q_1q_3 - q_2q_4) & 2(q_2q_3 + q_1q_4) & (q_3^2 - q_1^2 - q_2^2 + q_4^2) \end{bmatrix} \quad (2.15)$$

Equation (2.15) can be used to compute the vehicle's attitude parameters (roll, pitch and heading). For this, the rotation matrix from the b-frame to the l-frame needs to be computed, which is done by Equation (2.16):

$$R_b^l = R_e^l \times R_b^e \quad (2.16)$$

The attitude parameters can then be obtained by a comparison of Equation (2.16) with (2.7), and are computed using Equations (2.17) through (2.19):

$$\xi = -\tan^{-1}\left(\frac{(R_b^l)_{3,1}}{(R_b^l)_{3,3}}\right) \quad (2.17)$$

$$\eta = \sin^{-1}\left((R_b^l)_{3,2}\right) \quad (2.18)$$

$$\psi = \tan^{-1}\left(\frac{(R_b^l)_{1,2}}{(R_b^l)_{2,2}}\right) \quad (2.19)$$

where $(R_b^l)_{p,q}$ is the element of the p^{th} row and the q^{th} column of (R_b^l) matrix.

2.2.2.3 Transformation of Specific Force to the Navigation Frame

The velocity increment (Δv_f^b) should be rotated into the navigation frame (e-frame) prior to integration. Since, the rotation matrix is a function of time; instead of using the rotation matrix computed above (Equation (2.15)) the average orientation of the IMU during the interval t_k to t_{k+1} is preferred (Petovello 2003). Having said that, the velocity

increment in the e-frame can thus be calculated using either Equation (2.20) or Equation (2.21):

$$\Delta v_f^e = (R_b^e)_k \left(I + \frac{1}{2} S^b \right) \Delta v_f^b \tag{2.20}$$

$$\Delta v_f^e = (R_b^e)_{k+1} \left(I - \frac{1}{2} S^b \right) \Delta v_f^b \tag{2.21}$$

where, I is an identity matrix, and S^b is a skew-symmetric form of the angular increments in Equation (2.13).

2.2.2.4 Position and Velocity Update

The final velocity increment for computation of the vehicle's velocity is computed using Equation (2.22):

$$\Delta v^e = \Delta v_f^e - 2\Omega_{ie}^e v_k^e \Delta t + \gamma^e \Delta t \tag{2.22}$$

The second term above is the Coriolis acceleration, which is computed using the previous epoch's velocity (v_k^e), and the third term is the gravity correction computed based on the vehicle's position. Once the velocity increments are computed, the velocity can be updated using Equation (2.23):

$$v_{k+1}^e = v_k^e + \Delta v^e \tag{2.23}$$

Finally, the vehicle's position in the e-frame (Earth-fixed coordinates) can be obtained though the computed velocity using Equation (2.24):

$$r_{k+1}^{e} = r_{k}^{e} + \left(v_{k+1}^{e} + v_{k}^{e}\right)\frac{\Delta t}{2} \tag{2.24}$$

Figure 2.7 summarizes the overall e-frame INS mechanization described in this section.

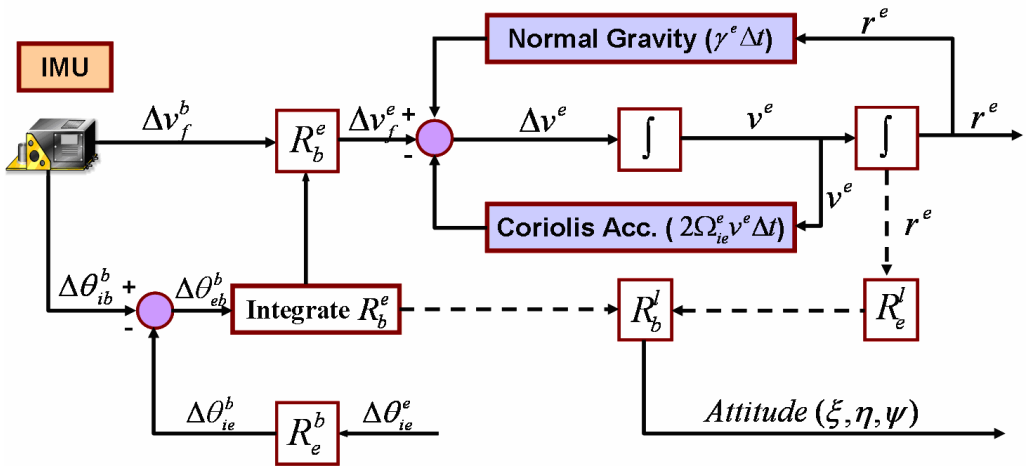

Figure 2.7: ECEF (e-frame) INS Mechanization (adapted from El-Sheimy 2004)

2.2.3 Inertial Sensor Errors

Despite remarkable advances of MEMS technology in cost and size constraints, MEMS based inertial sensors have inherited the error behaviour of conventional inertial sensors (Park 2004). The primary sources of gyro and accelerometer errors include sensor noise, scale factor errors, bias instability from turn-on to turn-on and bias drift after turn-on. Thus, the inertial sensor measurement equation for both accelerometer and gyros is given by Equations (2.25) and (2.26), respectively (Hide 2003, El-Sheimy 2004):

$$\tilde{f} = f + b_a + f.S_a + f.m_a + \eta_a \tag{2.25}$$

$$\tilde{w} = w + b_g + w.S_g + w.m_g + \eta_g \tag{2.26}$$

where, '~' denotes the measured value by the sensor, the subscript '*a*' means accelerometer specific errors, and '*g*' means gyro specific error. The symbols,

f is the specific force,

w is the angular rate,

b is the sensor bias,

S is the scale-factor error,

m is the non-orthogonality of sensor triads, and

η is the sensor random noise.

There are essentially two approaches to account for these sensor errors. The first approach is to determine the errors through specific lab-calibration procedures and correct the inertial measurements for them, before the navigation processing (Scherzinger 2004). The second approach is to include these errors as an additional part of the functional model parameters during the estimation process. However, not all the errors are deterministic in nature, and some errors have to be modeled stochastically. This section therefore provides a brief overview of each of these errors characteristics and determines the specific errors that need to be modeled stochastically during the estimation process.

2.2.3.1 Noise

Noise is an additional signal resulting from the sensor itself or other electronic equipment that interferes with the output signals being measured (El-Sheimy 2004). In general, noise is non-systematic and therefore cannot be removed from the data using deterministic models (Hou 2004). It can only be modeled by a stochastic process, where it is often considered as zero mean white Gaussian noise. The errors build up in gyro and

accelerometer measurements due to white noise is termed as angular/velocity random walk. The noise density is generally characterized in the units of signal/√Hz.

To use the IMU for any practical purpose, it is important to determine the noise power of the gyro and accelerometer sensors. Noise power can be determined using two methods. The first method is to compute the standard deviation using a few seconds of static data (after removing the mean) at several periods in the data set (Petovello 2003). The mean of the computed standard deviation values provides a heuristic estimate of the noise power. The second method is based on the wavelet decomposition of the data. Wavelet decomposition is a process in which a signal is successively broken down into low and high frequency components (Skaloud 1999, Nassar 2003). Low frequency components represent the slowly varying sensor errors (such as bias drift), while high frequency components represent the sensor noise. The standard deviation of the high frequency component thus provides the noise power estimate.

2.2.3.2 Sensor Bias

The inertial sensor bias is defined as the average of the output of each sensor over a specified time, measured at specified operating conditions that have no correlation with input acceleration or rotation (IEEE Std., 2001). The gyro bias is typically expressed in $^{\circ}$/h (or rad/s) and the accelerometer bias is expressed in m/s^2 (or mg).

The bias is generally considered to have two parts, a deterministic bias offset (often termed as turn-on bias) and a bias-drift. Turn-on bias is the bias in the inertial sensor

output when the sensor is turned on. This bias part remains constant over a particular mission, and thus is deterministic through lab calibration procedures. In most of the high end, or navigation grade, IMUs the turn-on biases (and the scale factors) are negligible (Nayak 2000). However, for low cost sensors such as the MEMS sensors, these errors are quite large and their repeatability is typically poor and thus, frequent calibration, which is every time the sensor is used, becomes a necessity. The bias-drift refers to the rate at which the error in inertial sensor accumulates with time (El-Sheimy 2004). This part is random in nature, and thus has to be modeled stochastically.

2.2.3.3 Scale Factor Errors

A scale factor is the ratio of a change in the output to a change in the input intended to be measured (IEEE Std., 2001). These errors are expressed in PPM. Typically, these errors are deterministic in nature but can also be modeled stochastically using any suitable random process (Scherzinger 2004).

2.2.3.4 Non-Orthogonality Errors

These errors are the result of a misalignment of the sensor axes caused by imperfections in the construction of the sensor assembly (Hide 2003). As a result, each axis is affected by measurements of the other two axes in the body frame. Axes misalignments, in general, are modeled as part of INS error equations (El-Sheimy 2004).

2.2.4 Initial Alignment

The initial alignment process of INS consists of two alignment modes, the horizontal alignment and the heading alignment.

2.2.4.1 Horizontal Alignment

An initial estimate of the horizontal alignment angles (roll and pitch) is obtained by accelerometer levelling, which uses knowledge of gravity sensed by each accelerometer, under static conditions. The obtained velocity increments from the accelerometer are used to compute roll and pitch using Equations (2.27) and (2.28) (Petovello 2003):

$$\xi = -\sin^{-1}\left(\frac{\Delta\bar{v}_x^b}{\gamma\Delta t}\right) \tag{2.27}$$

$$\eta = \sin^{-1}\left(\frac{\Delta\bar{v}_y^b}{\gamma\Delta t}\right) \tag{2.28}$$

where the 'bar' above a quantity represents a time average. The accuracy of these estimates depends on the accelerometer biases, through the relation given by Equations (2.29) and (2.30) (Nayak 2000, El-Sheimy 2004):

$$\delta\xi = \frac{(b_a)_x}{\gamma} \tag{2.29}$$

$$\delta\eta = \frac{(b_a)_y}{\gamma} \tag{2.30}$$

where $(b_a)_i$ is the bias in i^{th} accelerometer.

Based on the above equations, the level error estimation sensitivity to accelerometer bias is 0.06˚ per mg (milli-g). For the Crista IMU (MEMS IMU being used in this study), the accuracy of the coarse estimate of roll and pitch obtained in this way is on the order of 1.5˚-2˚ (see Table 1.1). Considering this accuracy level and knowing the fact that in the case of a land vehicle the roll and pitch generally remain within ± 5˚ (assuming vehicle is

on a relatively flat surface), they can be initialized with zeros (Shin & El-Sheimy 2004). The errors in the initialization can then be estimated through a Kalman filter, with either zero-velocity updates (ZUPTs) or updates from GPS.

2.2.4.2 Heading Alignment

An initial estimate of heading is determined by gyro compassing, which uses knowledge of the Earth rotation rate sensed by each gyro, under static conditions. The obtained angular increments from the gyros are rotated to the horizontal frame using Equation (2.31), and then the heading is computed by Equation (2.32) (Petovello 2003):

$$\Delta\bar{\theta}_{ib}^{h} = R_1(-\eta)R_2(-\xi)\Delta\bar{\theta}_{ib}^{b} \tag{2.31}$$

$$\psi = -\tan^{-1}\left(\frac{(\Delta\bar{\theta}_{ib}^{h})_x}{(\Delta\bar{\theta}_{ib}^{h})_y}\right) \tag{2.32}$$

However, this method for heading alignment is not feasible with low cost IMUs, since their gyro biases (turn-on bias and drifts) and noise typically exceeds the Earth rotation rate (Farrell & Barth 2001). An alternative approach for heading alignment is to fix the initial heading information from an external source. A potential source for such heading information is a magnetometer, which provides heading information by sensing the surrounding magnetic field. The accuracy assessment of one such magnetometer is presented in Appendix A. Another approach is to perform dynamic heading alignment using GPS velocities (Figure 2.8) (Salycheva 2004, Shin 2005).

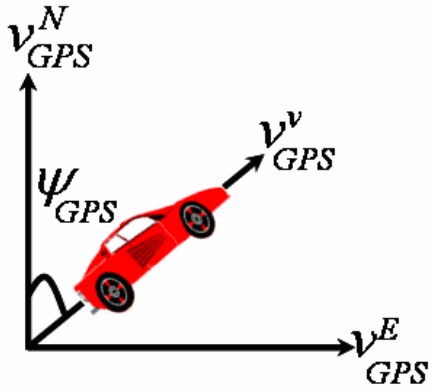

Figure 2.8: GPS Heading

Based on Figure 2.8, the heading from GPS velocities can be computed using Equation (2.33):

$$\psi_{GPS} = \tan^{-1}\left(\frac{v^E_{GPS}}{v^N_{GPS}}\right) \tag{2.33}$$

where v^E_{GPS} and v^N_{GPS} are the east and north GPS velocities.

The accuracy of the GPS-derived heading depends on the accuracy of the computed GPS velocities and the horizontal vehicle velocity through Equation (2.34):

$$\sigma^2_{\psi_{GPS}} = \frac{(v^E_{GPS})^2}{\left((v^E_{GPS})^2 + (v^N_{GPS})^2\right)^2}\sigma^2_{v^N_{GPS}} + \frac{(v^N_{GPS})^2}{\left((v^E_{GPS})^2 + (v^N_{GPS})^2\right)^2}\sigma^2_{v^E_{GPS}} = \frac{\sigma^2_{v_{GPS}}}{v^2_{GPS}} \tag{2.34}$$

where σ_X denotes the standard deviation of (X), and $v_{GPS} = \sqrt{(v^E_{GPS})^2 + (v^N_{GPS})^2}$ is the GPS velocity. Thus, the greater the vehicle velocity is, the better the heading accuracy. For this reason, GPS heading is calculated (and used) only when vehicle has sufficient speed (more than 5 m/s).

CHAPTER THREE : OVERVIEW OF ESTIMATION METHODS

This chapter provides an overview of the estimation and filtering theories relevant to this research. In particular, this chapter discusses the discrete linear and non-linear Kalman filters, which are used for estimating the state of interest. Principles of statistical testing of measurements are then presented at the end of the chapter. Much of the theory is taken from standard references such as Gelb (1974), Brown & Hwang (1997), and Grewal & Andrews (2001).

3.1 Estimation

Estimation is defined as a method to obtain a unique set of values for a set of unknown parameters, *x*, from a redundant set of observations, *z*. In order to obtain state estimates, a functional relationship between the unknown parameters and the observed quantities must be established (Gao 2004). Such a functional relationship (also referred to as measurement model) is given by Equation (3.1):

$$z(t) = H(t)x(t) + \eta(t) \tag{3.1}$$

where,

$H(t)$ is the design matrix of the system at time *t*, and

$\eta(t)$ is the measurement noise at time *t,* with a spectral density matrix *R(t).*

The above equation could be solved as a set of linear equations, if the number of observations, *m*, available is equal to number of unknown parameters, *n*. However, when there are redundant observations ($m>n$), then the estimator compute the solution which is

optimal in some sense. For instance, the least-square estimator in such a case provides a solution which minimizes the sum of squared residuals.

It follows from the above discussion, that the estimator such as least squares, computes the optimal state of the system using only knowledge of the measurement model. So, if the number of measurements available falls below the number of unknown parameters, such an estimator will not be able to compute the system state. However, if an estimator utilizes the information about the system state dynamics (if available) in computations, not only the system state can be determined in such situations, but in general, a better estimate of the desired parameters can be obtained. Such system dynamics (also referred to as process model) can be represented by Equation (3.2):

$$\dot{x}(t) = F(t)x(t) + G(t)w(t) \tag{3.2}$$

where, a 'dot' represents time derivative. The symbol,

$F(t)$ is the system dynamic matrix at time *t*,

$G(t)$ is the shaping matrix at time *t*, and

$w(t)$ is the process driving noise at time *t*, with spectral density matrix *Q(t)*.

The appearance of the process noise in Equation (3.2) illustrates the fact that the user knowledge about the system behaviour is limited. An example of an estimator which exploits both the knowledge of the system dynamics (Equation (3.2)) and the relationship between the states and the measurements (Equation (3.1)), to provide the optimal state of the system is a Kalman filter. In the context of this work, a Kalman filter is used.

Since the estimation algorithm is typically implemented on a computer, the discrete form of Equations (3.1) and (3.2) is more useful. The discrete form of Equation (3.2) is given by Equation (3.3):

$$x_{k+1} = \Phi_{k+1,k} x_k + w_k \tag{3.3}$$

where,

x_k is the state vector of the process at epoch t_k,

$\Phi_{k+1,k}$ is the state transition matrix from time t_k to t_{k+1}, and

w_k is the process driving noise at epoch t_k, with a covariance matrix Q_k.

The transition matrix, $\Phi_{k+1,k}$, can be obtained from the continuous time dynamic matrix, $F(t)$, assuming that the dynamic matrix is time invariant over the transition time interval. Even if this assumption is invalid, the errors can be mitigated by shortening the transition time interval (Petovello 2003). The relationship between the transition matrix and dynamic matrix can be expressed by Equation (3.4):

$$\Phi = e^{F\Delta t} = I + F\Delta t + \frac{(F\Delta t)^2}{2} + ... \tag{3.4}$$

where I is the identity matrix, and Δt is the transition time interval.

The process noise covariance matrix, Q_k, which accounts for uncertainty in the assumed process model, can be obtained by the integral of the continuous time spectral density matrix, $Q(t)$, and is given by Equation (3.5):

$$Q_k = \int_{t_k}^{t_{k+1}} \Phi_{k+1,\tau} G(\tau) Q(\tau) G^T(\tau) \Phi_{k+1,\tau}^T d\tau \tag{3.5}$$

The discrete form of the measurement model Equation (3.1) is given by Equation (3.6):

$$z_{k+1} = H_{k+1} x_{k+1} + \eta_{k+1} \tag{3.6}$$

where H_{k+1} is the design matrix of the system at time t_{k+1}, and η_{k+1} is the measurement noise at time t_{k+1}, with a covariance matrix R_{k+1}.

3.1.1 Kalman Filter Algorithm

A Kalman filter is a recursive algorithm that uses a series of prediction and measurement update steps to obtain an optimal estimate of the state vector which has a minimum variance. The Kalman filter algorithm assumes that the process to be estimated can be modeled in the form specified in Equation (3.3), and the measurement of the process is assumed to occur at discrete points in time in accordance with the relationship given in Equation (3.6). It further assumes that the process driving noise, w_k , and the measurement noise, η_k , have white noise characteristics which follows the conditions of zero mean, and zero correlation.

The equations in the Kalman filter algorithm fall under two groups. The first group of equations predicts the state (and the associated covariance) of the system, based on the current state and the assumed system model, to obtain an *a priori* estimates for the next time step, as stated by Equations (3.7) and (3.8) :

$$\hat{x}_{k+1}^- = \Phi_{k+1,k} \hat{x}_k^+ \tag{3.7}$$

$$P_{k+1}^{-} = \Phi_{k+1,k} P_k^{+} \Phi_{k+1,k}^{T} + Q_k \tag{3.8}$$

where the 'hat' represents the estimated quantity, the superscript '-' represents the predicted quantity (before measurement update), and the superscript '+' represents the updated quantity (after measurement update). The symbol P_k is the error covariance matrix associated with state vector at time t_k.

The second group of equations update the predicted states and covariance estimates with the available measurements, in accordance with the measurement model, using Equations (3.9) and (3.10):

$$\hat{x}_{k+1}^{+} = \hat{x}_{k+1}^{-} + K_{k+1} v_{k+1} \tag{3.9}$$

$$P_{k+1}^{+} = (I - K_{k+1} H_{k+1}) P_{k+1}^{-} \tag{3.10}$$

where K_{k+1} is the Kalman gain matrix at time t_{k+1}, and v_{k+1} is the innovation sequence at time t_{k+1}.

The innovation sequence, v_{k+1}, is the difference between the actual observation, z_{k+1}, and the predicted observation, $\hat{z}_{k+1}$, and thus represents the amount of new information introduced into the system by the actual measurements. It is computed as given by Equation (3.11):

$$v_{k+1} = z_{k+1} - \hat{z}_{k+1} = z_{k+1} - H_{k+1} \hat{x}_{k+1}^{-} \tag{3.11}$$

The Kalman gain matrix is a weighting factor, which indicates how much of the new information contained in the innovation sequence should be accepted by the system. As

such, the gain matrix is optimized to produce a minimum error variance, and is given by Equation (3.12) (refer Brown & Hwang (1997) for a detailed derivation):

$$K_{k+1} = P_{k+1}^{-} H_{k+1}^{T} (H_{k+1} P_{k+1}^{-} H_{k+1}^{T} + R_{k+1})^{-1} \tag{3.12}$$

The step-by-step Kalman filter algorithm is summarized in Figure 3.1.

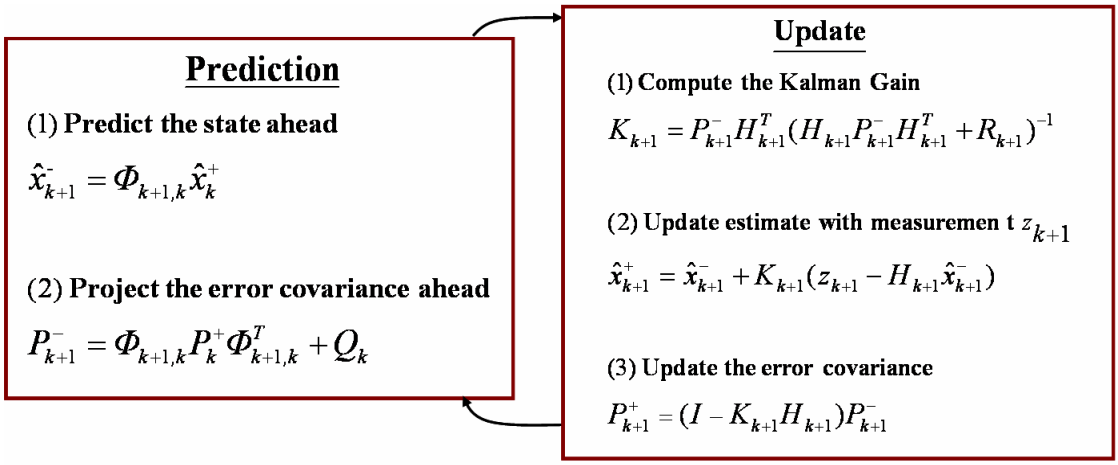

Figure 3.1: Discrete-time Kalman Filter Algorithm

3.1.2 Non-linear Kalman Filter

Some of the most successful applications of Kalman filtering have been in situations with non-linear dynamics or non-linear measurement relationships (Brown & Hwang 1997). The principle approach in such cases is to linearize the non-linear model first and then apply the standard Kalman filter to obtain the state of the system (Grewal & Andrews 2001). A non-linear process model and measurement model is stated by Equation (3.13) and Equation (3.14):

$$x_{k+1} = f(x_k, k) + w_k \tag{3.13}$$

$$z_{k+1} = h(x_{k+1}, k+1) + \eta_{k+1} \tag{3.14}$$

where *f* and *h* are known non-linear functions. For linearization, a nominal trajectory is selected, as given by Equation (3.15):

$$x_{k+1} = x^{*}_{k+1} + \delta x_{k+1} \tag{3.15}$$

where '*' represents the nominal state vector value, and 'δ' represents the perturbation from the nominal value.

Assuming that the perturbations are sufficiently small, the first order Taylor series expansion of Equations (3.13) and (3.14) is performed about the selected nominal trajectory to obtain Equations (3.16) and (3.17):

$$\delta x_{k+1} = \Phi_{k+1,k}\delta x_k + w_k \tag{3.16}$$

$$\delta z_{k+1} = H_{k+1}\delta x_{k+1} + \eta_{k+1} \tag{3.17}$$

Equation (3.16) forms a new linear process model, where the state vector is now replaced by the state error vector (perturbations). Similarly, Equation (3.17) is a new linear measurement model, where the measurement vector is replaced by measurement misclosures between the actual and predicted measurements. The transition matrix ($\Phi_{k+1,k}$) and the design matrix (H_{k+1}) in above equations are now a function of partial derivatives of the respective non-linear functions with respect to the state vector.

A filter where linearization is done about the predetermined nominal state vector is called a Linearized Kalman filter (LKF). However, a more common procedure is to derive the point of linearization from the last computed solution, $\hat{x}_k$, (instead of predetermined state

vector, x_k^*). This approach is used in the Extended Kalman filter (EKF). After the linearization step, a regular Kalman filter is applied to obtain the state error estimates, and the desired states are reconstructed through Equation (3.15).

3.2 Reliability Testing

In order to maintain the optimality of the computed states, a capability that prevents the erroneous measurements from entering the filter is required (Kaplan 1996). In the context of GPS/INS, faulty measurements are assumed to enter through GPS. GPS is susceptible to high-frequency faults possible due to the tracking of multipath signals, low C/N_o of the signal being received or poor satellite geometry. Errors in such faulty measurements are not captured in the functional relation (measurement model) and, since these errors are distinct from the ordinary measurement noise model, the filter will not be able to account for these blunders properly (Kuusniemi 2005). Thus, reliability testing of GPS measurements is of paramount importance for any GPS application (ibid).

Reliability typically refers to the ability to identify and reject errors (blunders) in the measurements. It is basically a pre-computation data screening step, which is performed by testing the misclosures between the predicted and the actual measurements (ibid). In the context of a Kalman filter, such misclosures are deemed the innovation sequence (Equation (3.11)), which has a property that it is zero mean and is normally distributed, as given by Equation (3.18), with a variance given by Equation (3.19):

$$v_{k+1} \sim N(0, \sigma_{v,k+1}) \tag{3.18}$$

$$\sigma_{v,k+1} = H_{k+1} P_{k+1}^{-} H_{k+1}^{T} + R_{k+1} \tag{3.19}$$

where N (p, q) means normal distribution with mean 'p' and variance 'q'. The symbol $\sigma_{v,k+1}$ is the innovation variance at time t_{k+1}.

The presence of any measurement outlier in the system will cause the innovation sequence to depart from the above defined properties (Gao 2004). So if a blunder vector, ∇, of dimension, d, is present in the measurement, the innovation sequence will be biased, and thus, can be assumed to follow a distribution as stated by Equation (3.20) (Teunissen & Salzmann 1989):

$$v_{k+1} \sim N(M_{k+1}\nabla_{k+1}, \sigma_{v,k+1}) \tag{3.20}$$

where M_{k+1} is the design matrix mapping blunder onto the observations at time t_{k+1}.

To detect the presence of these blunders, ∇, typically a two-step testing procedure is used. The first step is the global test in which a Chi-Square test is performed to determine any inconsistencies in the observation innovations. If the global test fails, a local test is applied (assuming single blunder) in order to isolate the outlier causing the inconsistency. A comprehensive discussion on these testing procedures could be found in Petovello (2003), Petovello et al (2003), Gao (2004), Mezentsev (2005), and Kuusniemi (2005). Once the outlier is isolated, it is excluded from the processing and then the local test is applied recursively on the remaining sub-sample to detect multiple outliers.

CHAPTER FOUR : GPS/INS INTEGRATION

Having reviewed major aspects of GPS and INS in previous chapters, this chapter discusses the theoretical and practical aspects of integrating the two systems. The chapter begins with a discussion of different integration strategies and approaches, followed by a discussion of different navigation Kalman filter designs (GPS-filter and INS-filter) required for integration. Then different approaches, based on using vehicle motion constraints to prevent the INS error degradation during the periods of GPS unavailability, are discussed. Various aspects, including the measurement model construction of each constraint measurements are discussed. Then an algorithm to incorporate external heading measurements into INS computations is derived. Finally, information about the software developed as part of this work is provided. It should be noted that all the algorithms discussed in this chapter are applicable for real-time implementation, although the performance of each will be evaluated through data processing in post-mission.

4.1 GPS/INS Integration

At the user level, GPS and INS are commonly integrated using either a *loosely coupled* or *tightly coupled* integration strategy. The specific choice of integration strategy, of these two strategies, depends on the type of application and operating environment. Both of these integration strategies basically differ by the type of information that is shared between the individual systems (Petovello 2003). For instance, a loosely coupled integration strategy involves blending processed measurements from GPS in INS computations, while a tightly coupled integration strategy operates on raw measurements from GPS. There are two basic implementation approaches for each integration strategy.

The first one, referred as *open loop*, deals with estimation of the INS errors using GPS information, and does not interfere with the operation of the INS. The second approach, called a *closed loop*, involves compensation of sensor errors within the calculation procedure of the INS mechanization scheme, using estimated errors from the Kalman filter (Nayak 2000). A comprehensive discussion of each integration strategy and each approach is provided in the following sections.

4.1.1 Loose Coupling

In this integration scheme, GPS and inertial processing is carried out in two separate, but interacting, filters (Ford et al 2001). Together these constitute a decentralized filter process; hence, this strategy is also referred as a decentralized integration strategy. The integration strategy is explained graphically in Figure 4.1.

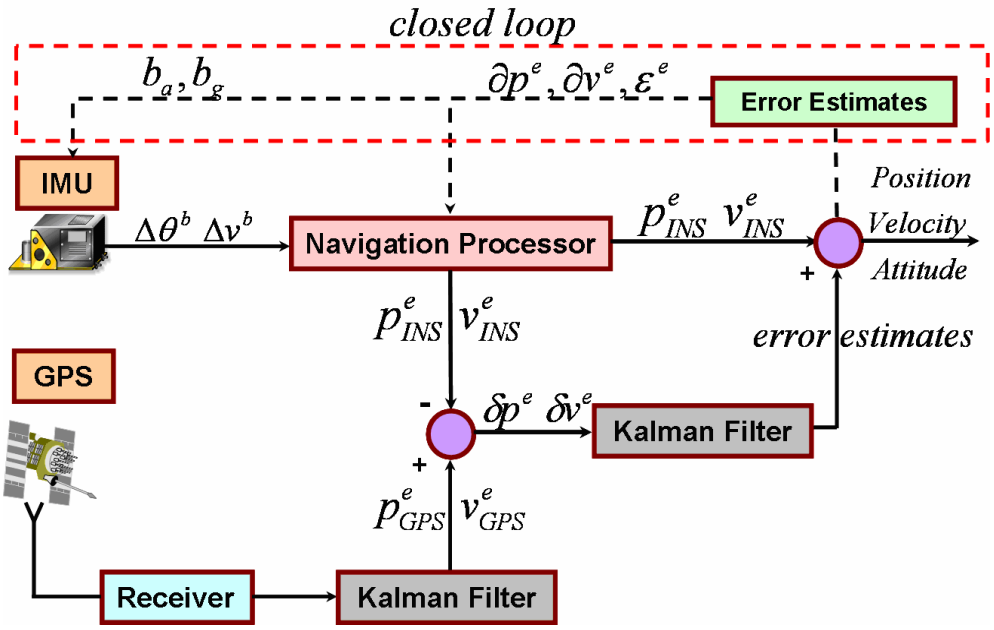

Figure 4.1: Loosely Coupled Integration Strategy

GPS measurements are processed independently in a GPS-only Kalman filter. Then the output of this filter is used periodically as input to the INS-only filter. The INS-only filter uses the difference between the GPS-derived position and velocity estimates and the INS mechanization-derived position and velocities as measurements to obtain the error estimates. The position/velocity covariance matrix from the GPS filter is used to construct the measurement noise matrix for the INS filter. The designs of the GPS- and INS-filters required for this integration strategy are discussed in Sections 4.2 and 4.3.

The loosely-coupled filtering approach has been popular due its simplicity of implementation and robustness. The robustness lies in the fact that if one of the systems fails, navigation can still be provided by other sensor. There are several disadvantages of this integration strategy, the primary being is its inability to provide measurement updates during periods of partial GPS availability (less than four satellites). However, this paradigm is changing as GPS is now increasingly being processed in a Kalman filter, which can predict the navigation solution based on partial GPS availability. The accuracy of this navigation solution, though, is typically poor, and the tightly coupled integration strategy is often seen to outperform this strategy under such situations. From a statistical view-point, Petovello (2003) identifies one specific problem with this implementation. Since it has two different Kalman filters, process noise has to be added to two different filters which ultimately impact the system performance. The extent of filtering is a function of the signal-to-noise ratio (also shown in ibid), which if decreased reduces the filtering capability of the system, thus limiting performance.

4.1.2 Tight Coupling

In this scheme, processing is carried out centrally in one common master filter; thereby this integration strategy is also termed as a centralized integration scheme. The integration strategy is shown graphically in Figure 4.2.

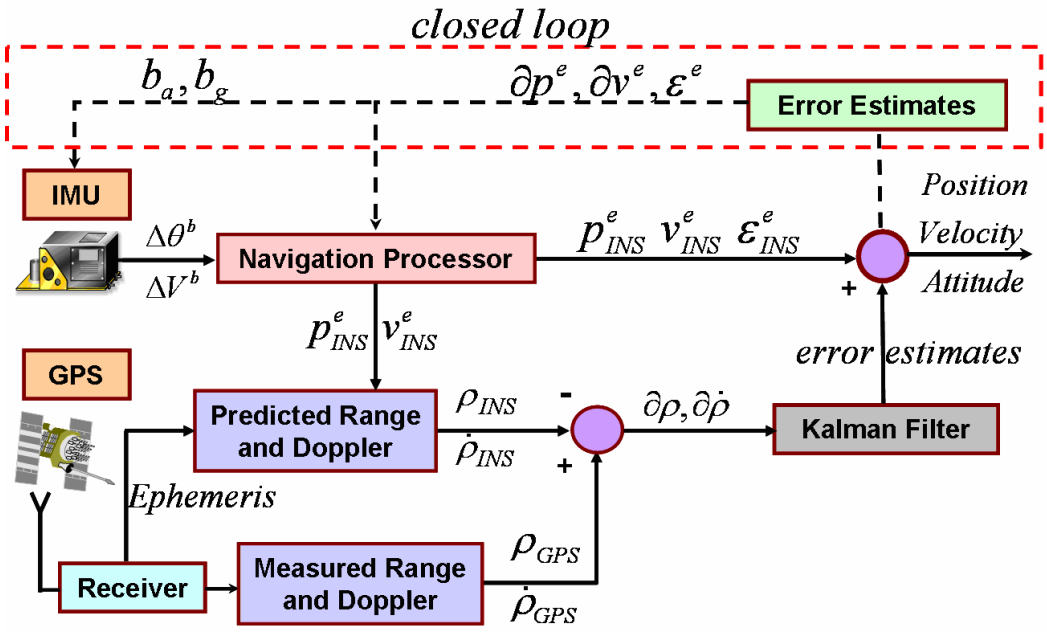

Figure 4.2: Tightly Coupled Integration Strategy

The GPS-derived raw pseudorange and Doppler measurement are combined with INS-predicted estimates of the pseudorange and Doppler measurements. The filter directly accepts residuals to obtain the INS error estimates (Knight 1999). These error estimates are then combined with INS derived navigation information, which finally forms the navigation output of the system.

This integration strategy is typically a preferred approach in urban canyons, primarily because it allows for reliable updating of the INS, even when the number of satellites is

less than four, which is a situation encountered frequently in such environments. In addition, this strategy offers enhanced reliability of the GPS measurements, as redundant information from two different sensors is used in the formulation of the reliability test statistic; leading to superior GPS fault detection and exclusion.

Although the arguments for choosing both forms of implementation have been balanced in literature, the tightly-coupled approach is currently gaining more weight mainly due to its added advantages in urban canyons. In this study however, both integration strategies are used, and thus a quantitative analysis of the performance of each strategy will be provided.

4.1.3 Implementation Approach

Typically, the two integration strategies are implemented using either an open loop (feed forward) approach or a closed loop (feedback) approach. In the open loop implementation, the INS mechanization operates independently without being aware of the existence of an estimator such as a Kalman filter. The Kalman filter estimates the errors in the mechanization-derived navigation information, corrects it, and then outputs it. The corrected parameters and estimated sensor biases and drifts are not sent back to the navigation processor. The INS error model is obtained by linearizing the mechanization equations in which the second order (and higher) terms are neglected. Without feedback, the mechanization error grows rapidly, which can make the neglected terms significant, and thus can introduce large errors into the integrated system. This kind of integration approach is valid for high end inertial sensors, which propagate relatively

small errors. However, a low cost MEMS IMU propagates large errors in a short time interval, and thus *on-the-fly* error compensation is required for the mechanization parameters.

In a closed loop integration scheme, a feedback loop is used (dotted line from the Kalman filter to the navigation processor in Figure 4.1 and Figure 4.2), which corrects the raw sensor output (using Equations (2.10) and (2.11)) and other mechanization parameters using the error estimates obtained from the Kalman filter. In this way, the mechanization propagates small errors thus maintaining the small error assumptions. The error states in this case must be reset to zero after every filter update.

4.2 GPS Filter

A GPS filter can be implemented using three different system models, namely, the position model, position-velocity (PV) model (constant velocity model), and position-velocity-acceleration (PVA) model (constant acceleration model). To this end, the position model estimates only the user's position, and thus is suitable only for stationary situations. Typically, in dynamic situations either of the PV or PVA model is used, where the user's position, velocity and/or acceleration is estimated. However, previous investigations have shown that there is no significant difference in the performance of the two models, particularly in a land vehicle environment (Schwarz et al 1989), and in general any of these two models can be used for GPS-based positioning. Thus, in this work the implemented filter uses the PV model whereby the filter estimates position and velocity errors with the latter being modeled as a random walk process. The choice of

random walk process is in accordance with the real-life physical situations, where the vehicular acceleration is usually brief and seldom sustained. The position and velocity states are parameterized in the WGS-84 ECEF-frame.

The measurement inputs to the GPS filter are the single differenced GPS observables, which mean that the filter state vector needs to be augmented with GPS receiver clock error states. Physically the clock error develops as the integral of the frequency error of the receiver clock oscillator offsets and clock drift (Brown & Hwang 1997). So, the clock error is described by two error states, clock offset and clock drift.

4.2.1 System Model

In the light of the above discussion, the system model for GPS can be considered to have navigation error states and sensor error states. The navigation error state vector is represented by Equation (4.1):

$$x_n = \left[\overbrace{\delta r_x^e \quad \delta r_y^e \quad \delta r_z^e}^{\delta r^e} \quad \overbrace{\delta v_x^e \quad \delta v_y^e \quad \delta v_z^e}^{\delta v^e} \right]^T \tag{4.1}$$

where, the superscript '*e*' represents the parameters in the ECEF frame, and the respective subscripts represents the corresponding directions. The symbol,

δr is the position error vector, and

δv is the velocity error vector.

Recall that the velocity errors are being modeled as random walk processes. Thus, the corresponding position and velocity error dynamic model can be given by Equation (4.2):

$$\begin{aligned} \delta\dot{r}^e &= \delta v^e \\ \delta\dot{v}^e &= \eta_v \end{aligned} \tag{4.2}$$

where the 'dot' represents the time derivative, and the symbol η_v is the process driving white noise with spectral density q_v.

The velocity error spectral density, q_v, is computed based on typical accelerations experienced in a land vehicle environment. The accelerations values were computed using kinematic GPS data collected in an open area environment, the standard deviation of which accelerations provides an estimate of the spectral density (Petovello 2003). The spectral density value was thus set as 1 m/s^2/√Hz for each dimension (ibid).

The corresponding sensor error state vector, which consists of clock offset and clock drift error states can be written as given by Equation (4.3):

$$x_s = \begin{bmatrix} ct & c\delta t \end{bmatrix}^T \tag{4.3}$$

where,

c is the speed of light (m/s),

t is the clock offset error state, and

δt is the clock drift error state.

The clock error states are defined in the units of range and range rates, by multiplying it by the speed of light, for compatibility with position and velocity states. The dynamic model for these errors can be written as shown in Equation (4.4):

$$\begin{aligned} c\dot{t} &= c\delta t + c\eta_t \\ c\dot{\delta t} &= c\eta_{\delta t} \end{aligned} \tag{4.4}$$

where,

η_t is the clock error driving noise with spectral density q_t, and

$\eta_{\delta t}$ is the clock drift error driving noise with spectral density $q_{\delta t}$.

For computing the clock error spectral densities, a standard clock stability model is used where the spectral densities are computed using Equations (4.5) and (4.6) (Brown & Hwang 1997, Mao et al 2002):

$$q_t = 2h_0 \tag{4.5}$$

$$q_{\delta t} = 8\pi^2 h_2 \tag{4.6}$$

where h_0, h_2 are Allan variance parameters that describe clock-drift (ibid).

Thus, the final system model for GPS is obtained by combining Equations (4.2) and (4.4), and is written in state-space form as given by Equation (4.7):

$$\underbrace{\begin{bmatrix} \delta\dot{r}^e \\ \delta\dot{v}^e \\ \dot{t} \\ \dot{\delta t} \end{bmatrix}}_{\dot{x}} = \underbrace{\begin{bmatrix} 0_{3\times3} & I_{3\times3} & 0 & 0 \\ 0_{3\times3} & 0_{3\times3} & 0 & 0 \\ 0_{1\times3} & 0_{1\times3} & 0 & 1 \\ 0_{1\times3} & 0_{1\times3} & 0 & 0 \end{bmatrix}}_{F} \underbrace{\begin{bmatrix} \delta r^e \\ \delta v^e \\ t \\ \delta t \end{bmatrix}}_{x} + \underbrace{\begin{bmatrix} 0_{3\times3} & 0 & 0 \\ I_{3\times3} & 0 & 0 \\ 0_{1\times3} & c & 0 \\ 0_{1\times3} & 0 & c \end{bmatrix}}_{G} \underbrace{\begin{bmatrix} (\eta_v)_{3\times1} \\ \eta_t \\ \eta_{\delta t} \end{bmatrix}}_{w} \tag{4.7}$$

The corresponding process noise spectral density matrix can be written as Equation (4.8):

$$Q(t) = \begin{bmatrix} (q_v)_{3\times3} & 0 & 0 \\ 0_{1\times3} & q_t & 0 \\ 0_{1\times3} & 0 & q_{\delta t} \end{bmatrix} \tag{4.8}$$

The discrete process noise matrix, Q_k, and the transition matrix, $\Phi_{k+1,k}$ (required for the Kalman filter algorithm) can be obtained by substituting the dynamic matrix, F, and the spectral density matrix, $Q(t)$, in Equations (3.4) and (3.5).

4.2.2 Measurement Model

The measured pseudorange (ρ) and Doppler ($\dot{\rho}$) observables are related to the user's position and velocity through the relation given by the Equations (4.9) and (4.10), respectively (Kaplan 1996):

$$\rho^i = \sqrt{(r^i_{s,x} - r_x)^2 + (r^i_{s,y} - r_y)^2 + (r^i_{s,z} - r_z)^2} + ct \tag{4.9}$$

$$\dot{\rho}^i = \frac{(r^i_{s,x} - r_x)(v^i_{s,x} - v_x) + (r^i_{s,y} - r_y)(v^i_{s,y} - v_y) + (r^i_{s,z} - r_z)(v^i_{s,z} - v_z)}{\rho^i} + c\dot{\delta t} \tag{4.10}$$

where, subscript '*s*' represent satellite specific information, and superscript '*i*' represents the i^{th} satellite.

These equations are non-linear, and thus need to be linearized to be used in the Kalman filter algorithm. Linearization is done using Equation (3.17), where the linearization point is the predicted state estimate at a particular epoch (i.e. $\hat{x}_k^-$). The corresponding design

matrices, $H(\rho)$ and $H(\dot{\rho})$, relating the pseudorange and Doppler observations to the error states are given by Equations (4.11) and (4.12):

$$H(\rho)=\begin{bmatrix} \frac{\partial\rho^1}{\partial r_x} & \frac{\partial\rho^1}{\partial r_y} & \frac{\partial\rho^1}{\partial r_z} & 0 & 0 & 0 & 1 & 0 \\ .. & .. & .. & .. & .. & .. & .. & .. \\ \frac{\partial\rho^N}{\partial r_x} & \frac{\partial\rho^N}{\partial r_y} & \frac{\partial\rho^N}{\partial r_z} & 0 & 0 & 0 & 1 & 0 \end{bmatrix}_{m_1\times 8} \tag{4.11}$$

$$H(\dot{\rho})=\begin{bmatrix} \frac{\partial\dot{\rho}^1}{\partial r_x} & \frac{\partial\dot{\rho}^1}{\partial r_y} & \frac{\partial\dot{\rho}^1}{\partial r_z} & \frac{\partial\dot{\rho}^1}{\partial v_x} & \frac{\partial\dot{\rho}^1}{\partial v_y} & \frac{\partial\dot{\rho}^1}{\partial v_z} & 0 & 1 \\ .. & .. & .. & .. & .. & .. & .. & .. \\ \frac{\partial\dot{\rho}^N}{\partial r_x} & \frac{\partial\dot{\rho}^N}{\partial r_y} & \frac{\partial\dot{\rho}^N}{\partial r_z} & \frac{\partial\dot{\rho}^N}{\partial v_x} & \frac{\partial\dot{\rho}^N}{\partial v_y} & \frac{\partial\dot{\rho}^N}{\partial v_z} & 0 & 1 \end{bmatrix}_{m_2\times 8} \tag{4.12}$$

where,

$\left.\frac{\partial}{\partial r_b}\right|_{b=x..z}$ is the partial derivative with respect to the position error vector, and

$\left.\frac{\partial}{\partial v_b}\right|_{b=x..z}$ is the partial derivative with respect to the velocity error vector.

Thus the final design matrix can be written as Equation (4.13):

$$H=\begin{bmatrix} H(\rho) \\ H(\dot{\rho}) \end{bmatrix}_{(m_1+m_2)\times 8} \tag{4.13}$$

The measurement misclosures are computed using Equation (4.14):

$$\delta z=\begin{bmatrix} \Delta\rho \\ \Delta\dot{\rho} \end{bmatrix}_{(m_1+m_2)\times 1}-\begin{bmatrix} \Delta\tilde{\rho} \\ \Delta\tilde{\dot{\rho}} \end{bmatrix}_{(m_1+m_2)\times 1} \tag{4.14}$$

where, the sign '~' represents the predicted measurements computed based on filter-predicted estimates of position and velocity, and 'Δ' represents single difference observations.

The measurement noise covariance matrix can be computed in different ways. One commonly used approach is to assign equal weights to all measurements (typically 1 to 10 m); however, this approach can result in relatively noisier satellite measurements corrupting the state estimates (Hide 2003). As satellites get lower in the sky, the received signal power decreases and multipath increases (Misra & Enge 2001). Also, the residual differential errors are likely to be larger for lower elevation satellites; specifically the tropospheric and ionospheric errors (refer to Section 2.1.3). Therefore, low elevation satellites are expected to provide measurements with larger errors as compared to high-elevation satellites. Thus one approach is to weight measurements based on the satellite elevation angle.

Different researchers have used different relations to predict the measurement errors based on the satellite elevation angle. For instance, Xin-Xiang (1996) and Satirapod & Wang (2000) used an exponential function relating satellite elevation angle and predicted measurements error. Petovello (2003) computed the standard deviation of the measurement errors at the zenith, and scaled it by $1/\sin(e)$, where e is the satellite elevation angle, for satellites at lower elevation angles. In this work, the latter approach is used.

4.3 INS Filter

The INS mechanization discussed in Section 2.2.2 process the raw measurements obtained from INS without accounting for their inherent errors. To correct for these errors, an INS filter must be set up which provides an estimate of the errors in the INS output. This is typically accomplished through measurement updates from GPS, using knowledge of the inertial sensor error development over time (Hide 2003). The corresponding design of the system and measurement models required for Kalman filter algorithm are discussed in the following sections.

4.3.1 System Model

A basic INS filter generally consists of nine navigation error states, including three positions, three velocities and three attitude error states. However, due to errors in the inertial sensor measurements, the system state vector need to be augmented by the sensor error states, where the number of error states depends on the inertial sensor error characteristics.

4.3.1.1 Navigation Error States

The inertial navigation error state behaviour is obtained by the perturbation of the mechanization equations (Equation (2.9)). This perturbation analysis is well documented in a number of publications, such as Savage (2000), Rogers (2000), Farrell & Barth (2001), Shin (2001), and El-Sheimy (2004); hence the full derivation of the error equations is not shown here. The obtained error model is represented by series of differential equations as stated in Equation (4.15) (El-Sheimy 2004):

$$\begin{aligned}
\delta\dot{r}^e &= \delta v^e \\
\delta\dot{v}^e &= N^e \delta r^e - 2\Omega_{ie}^e \delta v^e - F^e \varepsilon^e + R_b^e \delta f^b \\
\dot{\varepsilon} &= -\Omega_{ie}^e \varepsilon^e + R_b^e \delta w^b
\end{aligned} \tag{4.15}$$

where, "dots" denote the time derivatives and the superscripts '*e*' and '*b*' denote the ECEF and body frames, respectively. The symbol,

δr is the position error state vector ($\delta r_x, \delta r_y, \delta r_z$),

δv is the velocity error state vector ($\delta v_x, \delta v_y, \delta v_z$),

F is the skew symmetric matrix of specific force (f_x, f_y, f_z),

ε is the misalignment error state vector ($\varepsilon_x, \varepsilon_y, \varepsilon_z$),

N is the tensor of the gravitational gradients,

Ω_{ie} is the skew symmetric matrix of the Earth rotation rate relative to inertial space,

R_b^e is the rotation matrix from the body frame to the ECEF frame,

δf is the accelerometer sensor errors ($\delta f_x, \delta f_y, \delta f_z$), and

δw is the gyro sensor errors ($\delta w_x, \delta w_y, \delta w_z$).

This error model is termed as the *phi*-angle error model in the literature.

4.3.1.2 Inertial Sensor Error States

The inertial sensor measurement equation is given by Equation (2.25). Typically, the sensor turn-on biases, scale factor errors and non-orthogonality errors for high-end IMUs (navigation or tactical grade) are negligible (refer to Table 1.1). For these IMUs the measurement could be considered to have just the bias-drift (δb_i) and noise (η_i). The

inertial sensor measurement equation (Equation (2.25)) could therefore be reduced to Equation (4.16) (for high-end IMUs) (Petovello 2003, Zhang 2003):

$$\begin{aligned} \delta f &= \tilde{f} - f = \delta b_a + \eta_a \\ \delta w &= \tilde{w} - w = \delta b_g + \eta_g \end{aligned} \tag{4.16}$$

The spectral density, q_i, of the sensor measurement noise, η_i, is computed based on methods introduced in Section 2.2.3.1.

The bias-drift, δb_i, can be modeled as any appropriate noise process; however, the most commonly used is the First order Gauss Markov process given by Equation (4.17):

$$\begin{aligned} \dot{\delta b_a} &= -\frac{1}{\tau_a}\delta b_a + \eta_{ba} \\ \dot{\delta b_g} &= -\frac{1}{\tau_g}\delta b_g + \eta_{bg} \end{aligned} \tag{4.17}$$

where,

τ_i is the correlation time, and

η_{bi} is the Gauss-Markov process driving noise with spectral density q_{bi}.

The Gauss-Markov model parameters, τ_i and σ_i, are obtained by computing the auto-correlation function of the raw static data (Gelb 1974, Nassar 2003). This method of obtaining the model parameters is termed as auto-correlation analysis. The spectral density, q_{bi}, of the process driving noise, η_{bi}, is computed based on the Gauss-Markov model parameters, using Equation (4.18):

$$q_{bi} = \sqrt{\frac{2\sigma_i^2}{\tau_i}} \tag{4.18}$$

where σ_i is the Gauss-Markov temporal standard deviation.

Equations (4.15) and (4.17) together form the process model for a 15 state filter, consisting of nine navigation error states and six sensor error states. This filter herein will be referred to as a *15-state filter*. The state space model for this 15-state filter is thus given by Equation (4.19):

$$\underbrace{\begin{bmatrix} \delta\dot{r}^e \\ \delta\dot{v}^e \\ \dot{\varepsilon} \\ \delta\dot{b}_a \\ \delta\dot{b}_g \end{bmatrix}}_{\dot{x}} = \underbrace{\begin{bmatrix} 0_{3\times3} & I_{3\times3} & 0_{3\times3} & 0_{3\times3} & 0_{3\times3} \\ N^e_{3\times3} & -2(\Omega^e_{ie})_{3\times3} & -F^e_{3\times3} & (R^e_b)_{3\times3} & 0_{3\times3} \\ 0_{3\times3} & 0_{3\times3} & -(\Omega^e_{ie})_{3\times3} & 0_{3\times3} & (R^e_b)_{3\times3} \\ 0_{3\times3} & 0_{3\times3} & 0_{3\times3} & (-1/\tau_a)_{3\times3} & 0_{3\times3} \\ 0_{3\times3} & 0_{3\times3} & 0_{3\times3} & 0_{3\times3} & (-1/\tau_g)_{3\times3} \end{bmatrix}}_{F} \underbrace{\begin{bmatrix} \delta r^e \\ \delta v^e \\ \varepsilon \\ \delta b_a \\ \delta b_g \end{bmatrix}}_{x} + \underbrace{\begin{bmatrix} 0_{3\times3} & 0_{3\times3} & 0_{3\times3} & 0_{3\times3} \\ (R^e_b)_{3\times3} & 0_{3\times3} & 0_{3\times3} & 0_{3\times3} \\ 0_{3\times3} & (R^e_b)_{3\times3} & 0_{3\times3} & 0_{3\times3} \\ 0_{3\times3} & 0_{3\times3} & I_{3\times3} & 0_{3\times3} \\ 0_{3\times3} & 0_{3\times3} & 0_{3\times3} & I_{3\times3} \end{bmatrix}}_{G} \underbrace{\begin{bmatrix} \eta_a \\ \eta_g \\ \eta_{ba} \\ \eta_{bg} \end{bmatrix}}_{w} \tag{4.19}$$

The corresponding process noise spectral density matrix is given by Equation (4.20):

$$Q(t) = \begin{bmatrix} (q_a)_{3\times3} & 0_{3\times3} & 0_{3\times3} & 0_{3\times3} \\ 0_{3\times3} & (q_g)_{3\times3} & 0_{3\times3} & 0_{3\times3} \\ 0_{3\times3} & 0_{3\times3} & (q_{ba})_{3\times3} & 0_{3\times3} \\ 0_{3\times3} & 0_{3\times3} & 0_{3\times3} & (q_{bg})_{3\times3} \end{bmatrix} \tag{4.20}$$

However, the sensor errors in low cost MEMS inertial sensors are high, especially for the IMU considered herein (Crista). In this case, the sensor scale factor errors and the turn-on biases are very high (refer to Table 1.1). Although deterministic in nature (refer to Section 2.2.3) these errors typically vary from one turn-on to another for low cost sensors. Practically, it is not feasible to calibrate them every time the sensor is turned on, so a solution to this problem is to include these errors as part of the functional model and to estimate them in a Kalman filter. Thus, the measurement equation for the MEMS sensors is now written as Equation (4.21) (Park 2004):

$$\begin{aligned} \delta f &= f.S_a + b_a + \eta_a \\ \delta w &= w.S_g + b_g + \eta_g \end{aligned} \tag{4.21}$$

where,

S_i is the scale factor error, and

b_i is the sensor bias which is the combination of sensor turn on bias ($b_{i,tob}$) and the bias-drift (δb_i).

The bias-drift is again modeled as a Gauss Markov process, as stated by Equation (4.17). The model parameters were obtained through auto-correlation analysis, conducted with the static data collected with the Crista IMU. The obtained model parameters are listed in Table 4.1. The table also lists the computed sensor noise spectral densities for the Crista IMU (as discussed in Section 2.2.3.1).

Table 4.1: Sensors Random Noise Spectral Density and Gauss Markov Parameters for Crista IMU

	Gyros			***Accelerometers***		
	Noise	***Gauss Markov Parameters***		***Noise***	***Gauss Markov Parameters***	
	(°/h/ √Hz)	$\sigma\ (^\circ/h)$	$\tau\ (s)$	(g/√Hz)	$\sigma\ (m/s^2)$	$\tau\ (s)$
X	226.06	211.06	381.92	280 e-6	0.007	227.46
Y	177.07	204.64	375.23	400 e-6	0.007	210.78
Z	165.22	161.31	297.37	280 e-6	0.009	364.82

The inertial sensor turn on bias, $b_{i,tob}$, remains constant for a particular run. These biases are therefore modeled as random constant processes in the filter, as given by Equation (4.22):

$$\begin{aligned} \dot{b}_{a,tob} &= 0 \\ \dot{b}_{g,tob} &= 0 \end{aligned} \tag{4.22}$$

The standard deviation for these errors, which is needed to model them as random constant processes, is obtained through static testing in lab, and are listed in Table 4.2.

The sensor scale factor errors, S_i, change slowly with time, and thus can be modeled as first order Gauss Markov processes, assuming large correlation times (Scherzinger 2004). This is represented mathematically by Equation (4.23):

$$\begin{aligned} \dot{S}_a &= -\frac{1}{\tau_{sa}}(S_a) + \eta_{sa} \\ \dot{S}_g &= -\frac{1}{\tau_{sg}}(S_g) + \eta_{sg} \end{aligned} \tag{4.23}$$

The correlation time, τ_{si}, to model these errors in the Kalman filter was chosen to be five hours, which is defined empirically (ibid). The temporal standard deviation values, σ_{si}, were obtained using the specifications provided by the company. The corresponding process driving noise power, q_{si}, can be computed by substituting the assumed standard deviation and correlation time values in Equation (4.18). The model parameters used for each sensor in MEMS IMU is listed in Table 4.2.

Table 4.2: Turn on Bias and Scale Factor Model Parameters for Crista IMU

	Gyros			***Accelerometers***		
	Turn On Bias	**Scale Factor**		**Turn On Bias**	**Scale Factor**	
	$\sigma\,(^{\circ}/h)$	$\sigma_{sg}\,(PPM)$	$\tau_{sg}\,(s)$	$\sigma\,(m/s^2)$	$\sigma_{sa}\,(PPM)$	$\tau_{sa}\,(s)$
X	4230	10000	18000	0.480	10000	18000
Y	1800	10000	18000	0.260	10000	18000
Z	1800	10000	18000	0.480	10000	18000

Equation (4.15), combined with Equations (4.17), (4.22), and (4.23) form a 27 state filter consisting of nine navigation error states and eighteen sensor error states. This filter herein will be referred to as the *27-state filter*. The state space model and the process noise spectral density matrix for this filter are obtained by augmenting Equations (4.19) and (4.20) by Equations (4.24) and (4.25), respectively:

$$\underbrace{\begin{bmatrix} \dot{b}_{a,tob} \\ \dot{b}_{g,tob} \\ \dot{S}_a \\ \dot{S}_g \end{bmatrix}}_{\dot{x}} = \underbrace{\begin{bmatrix} 0_{3\times3} & 0_{3\times3} & 0_{3\times3} & 0_{3\times3} \\ 0_{3\times3} & 0_{3\times3} & 0_{3\times3} & 0_{3\times3} \\ 0_{3\times3} & 0_{3\times3} & (-1/\tau_{sa})_{3\times3} & 0_{3\times3} \\ 0_{3\times3} & 0_{3\times3} & 0_{3\times3} & (-1/\tau_{sg})_{3\times3} \end{bmatrix}}_{F} \underbrace{\begin{bmatrix} b_{a,tob} \\ b_{g,tob} \\ S_a \\ S_g \end{bmatrix}}_{x} + \underbrace{\begin{bmatrix} 0_{3\times3} & 0_{3\times3} \\ 0_{3\times3} & 0_{3\times3} \\ I_{3\times3} & 0_{3\times3} \\ 0_{3\times3} & I_{3\times3} \end{bmatrix}}_{G} \underbrace{\begin{bmatrix} \eta_{sa} \\ \eta_{sg} \end{bmatrix}}_{w} \tag{4.24}$$

$$Q(t) = \begin{bmatrix} (q_{sa})_{3\times3} & 0_{3\times3} \\ 0_{3\times3} & (q_{sg})_{3\times3} \end{bmatrix} \tag{4.25}$$

The discrete process noise matrix and the corresponding transition matrix can be obtained through Equations (3.4) and (3.5).

4.3.1.3 Aiding Sensor Error States

Since the processing is centralized in a tightly coupled integration scheme, the INS filter in that case must account for all the GPS states as well (Petovello 2003). The position and velocity error states are common in both the filters (see Equations (4.7) and (4.19)), so the INS filter needs to be augmented by just the receiver clock error states, which is achieved by transferring the last two rows of Equations (4.7) to Equation (4.19). Thus in a tightly coupled integration strategy, the 15- and 27-state INS filters turns to 17- and 29-state filters, respectively. However, to maintain clarity of discussion, these filters are still referred to as the 15- and 27-state filters, thereby referring only to INS specific states. Since GPS acts as an aiding source to the INS, the error states corresponding to GPS in the INS filter are termed as aiding sensor error states. It should be noted that the INS filter for the loosely coupled integration scheme remains unchanged, as the processing is decentralized in this case.

4.3.2 Measurement Model

The measurement model for the INS filter depends on the type of integration strategy being used, and are discussed in the following sections.

4.3.2.1 Loose Coupling

The INS-only filter uses the difference between the GPS-derived position and velocity estimates, and the INS mechanization-derived position and velocities as measurements to obtain the error estimates. Thus, the measurement design matrix and the misclosure vector can be written as given by Equations (4.26) and (4.27):

$$H(LC) = \begin{bmatrix} I_{3\times3} & 0_{3\times3} & 0_{3\times(n-6)} \\ 0_{3\times3} & I_{3\times3} & 0_{3\times(n-6)} \end{bmatrix} \tag{4.26}$$

$$\delta z = \begin{bmatrix} r^e_{GPS} - r^e_{INS} \\ v^e_{GPS} - v^e_{INS} \end{bmatrix}_{6\times1} \tag{4.27}$$

where n is the number of states in the INS filter.

The measurement noise for the INS-filter is formed by transferring the 'complete' position/velocity covariance matrix from the GPS-only filter to the INS-filter. This ensures that the correlation between the GPS processed position and velocities are properly accounted through the off-diagonal terms present in the covariance matrix (Kaplan 1996).

4.3.2.2 Tight Coupling

The measurement model for the INS-only filter in a tightly coupled integration strategy is the same as the measurement model derived earlier for GPS-only filter, i.e. Equations (4.11) through (4.14), with the only difference being the linearization point. The nominal trajectory for linearization is now obtained from the INS mechanization computed position and velocity information, rather than the predicted estimates. The poor

measurement updates are again detected through the statistical testing procedure discussed in Section 3.2.

4.3.2.3 INS Prediction

The measurements updates to the INS-filter come from GPS, so if a GPS outage occurs, the INS will operate in prediction mode. The update step in the Kalman filter, in such a scenario, is skipped and the filter predicts the system statistic based on Equations (3.7) and (3.8). During this period, the position, velocity, and attitude output of the system is the output of the INS mechanization directly. Thus, the performance of the integrated system depends largely on the quality of the IMU and the quality of the sensor error compensation, during GPS outages.

4.4 Vehicle Motion Constraints

Based on the discussion in Section 4.3.2.3, it is apparent that the performance of an INS will degrade in the absence of GPS measurements. The degradation with low cost MEMS IMUs is particularly severe owing to their large sensor errors and noise levels. Under such a situation, several land vehicle motion attributes can be used to prevent INS error accumulation. The idea is to derive the observations from constraint equations reflecting the behaviour of a land vehicle. The first set of constraint equations are termed as velocity constraints, which constrain the vehicle to move in a forward direction. The second constraint equation is termed as a height constraint which is derived from the fact that the height does not change much in land vehicular environment, particularly over short time periods. Further details about each motion constraint are provided in the following sections.

4.4.1 Velocity Constraints

The vehicle velocity constraints are derived assuming that the vehicle does not slip, which is a close representation for travel in a constant direction. A second assumption is that the vehicle stays on the ground, i.e. it does not jump of the ground. If both assumptions are true, then the velocity of the vehicle in the direction perpendicular to the movement of the vehicle must be zero (Sukkarieh 2000), as shown in Figure 4.3.

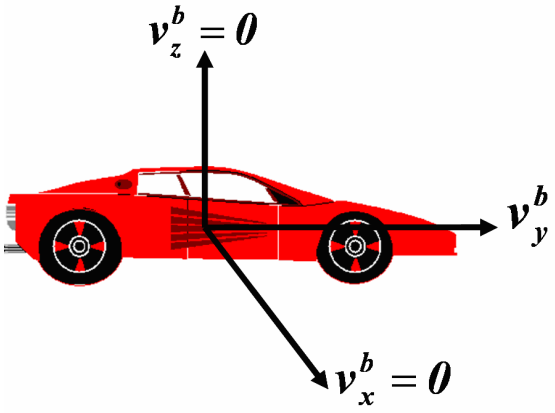

Figure 4.3: Vehicle Velocity Constraints

Thus, assuming that the Y axis of the IMU points in the direction of the vehicle forward velocity vector, the above concept can be described mathematically by Equation (4.28):

$$\begin{aligned} v_x^b &= \eta_x \\ v_z^b &= \eta_z \end{aligned} \tag{4.28}$$

where η_i is the measurement noise value denoting any possible discrepancies in the above stated assumptions for a particular direction (x or z). The magnitude of the noise is chosen to reflect the extent of the expected constraint violations (Sukkarieh 2000).

The proposed and implemented algorithm is to use GPS when it is available with INS to provide navigation information, and when a GPS outage occurs a complementary Kalman filter is used to combine the INS- and constraints-derived velocity measurements to keep the position and velocity errors bounded. The structure of the Kalman filter when constraints are used is shown in Figure 4.4, while the measurement model is derived in the following section.

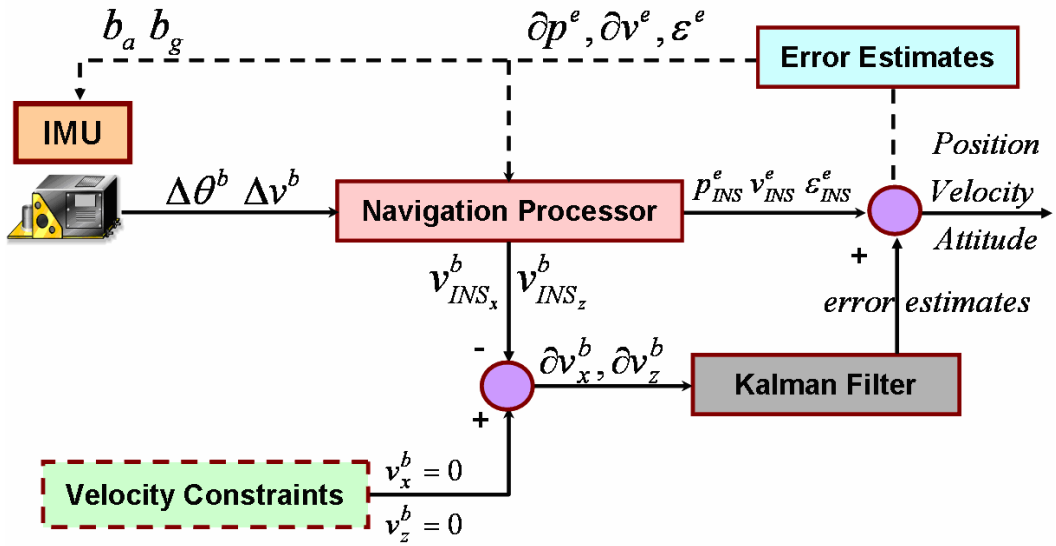

Figure 4.4: Velocity Constrained Navigation Block Diagram

4.4.1.1 Measurement Model

To set the right component of the velocity vector to zero, the INS velocity needs to be transformed from the mechanization frame (ECEF frame) to the body frame, which can be done using the relationship given in Equation (4.29):

$$v^b = (R^e_b)^T v^e \tag{4.29}$$

In order to relate these measurements to the system states, Equation (4.29) was perturbed to obtain Equation (4.30), which could further be reduced to Equation (4.31):

$$v^b + \partial v^b = ((I + E^e)R_b^e)^T (v^e + \partial v^e) \tag{4.30}$$

$$\partial v^b = R_e^b (\partial v^e - E^e v^e) \tag{4.31}$$

where E^e is the skew-symmetric matrix of misalignment error states.

After some obvious transformations, Equation (4.31) can be rewritten as Equation (4.32), which forms the body frame velocity error equation:

$$\partial v^b = R_e^b \partial v^e + R_e^b (v^e \times) \varepsilon^e \tag{4.32}$$

As noted from Equation (4.32) the misclosures in the body frame velocity components are related to the ECEF frame velocity error states, and to the attitude error states through the rotation matrix. The first and last rows of Equation (4.32) form the measurement design matrix, as given by Equation (4.33):

$$H(v^b) = \begin{bmatrix} 0_{1\times3} & R_{11} & R_{12} & R_{13} & R_{12}v_z^e - R_{13}v_y^e & R_{13}v_x^e - R_{11}v_z^e & R_{11}v_y^e - R_{12}v_x^e & 0_{1\times(n-9)} \\ 0_{1\times3} & R_{31} & R_{32} & R_{33} & R_{32}v_z^e - R_{33}v_y^e & R_{33}v_x^e - R_{31}v_z^e & R_{31}v_y^e - R_{32}v_x^e & 0_{1\times(n-9)} \end{bmatrix} \tag{4.33}$$

The measurement misclosures can be computed using Equation (4.34):

$$\begin{bmatrix} \delta v_x^b \\ \delta v_z^b \end{bmatrix} = \begin{bmatrix} 0 \\ 0 \end{bmatrix} - \begin{bmatrix} v_{INS_x}^b \\ v_{INS_z}^b \end{bmatrix} \tag{4.34}$$

The measurement noise for these measurements is computed based on a projection of the forward velocity in the lateral and up directions due to the misalignment angles (Shin 2001). This method is explained graphically in Figure 4.5. If v_y^b is the forward velocity, the velocity component that gets projected in the lateral/up direction because of the

misalignment angle, θ, is $v_y^b \sin\theta$. The measurement standard deviation computed in this way, assuming $v_y^b = 18 - 20\ m/s$ and $\theta = 2 - 3^\circ$, is around 1 m/s.

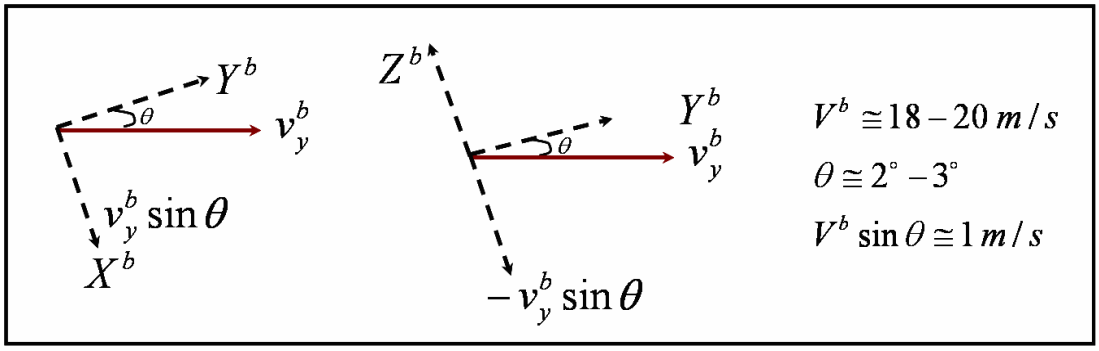

Figure 4.5: Computation of Velocity Constraints Standard Deviation (adapted from Shin 2001)

4.4.2 Height Constraints

Since a vehicle generally always stays on a road, the height solution does not typically vary by more than few tens of metres in a small region. So, a predefined fixed height value can be used as a constraint measurement or else the best height solution computed before going into a GPS outage can be used as the height constraint measurement. The use of such measurements not only provides improvements in the height solution, but can also improve the overall horizontal solution during GPS unavailability (Lachapelle et al 2003). A three dimensional position fix traditionally requires observations to four satellites to solve for the horizontal position, vertical position and the receiver clock offset. If the height component is treated as a known parameter (obtained from constraints), then the remaining unknowns can be solved with one less satellite. This can improve the coverage in urban canyon environments, and thus can potentially help to

improve the overall horizontal solution accuracy. However, a realistic measurement uncertainty value must be chosen for these measurements, because any errors in the height solution will ultimately skew the horizontal solution (MacGougan 2003). The filter design when height is constrained is shown in Figure 4.6.

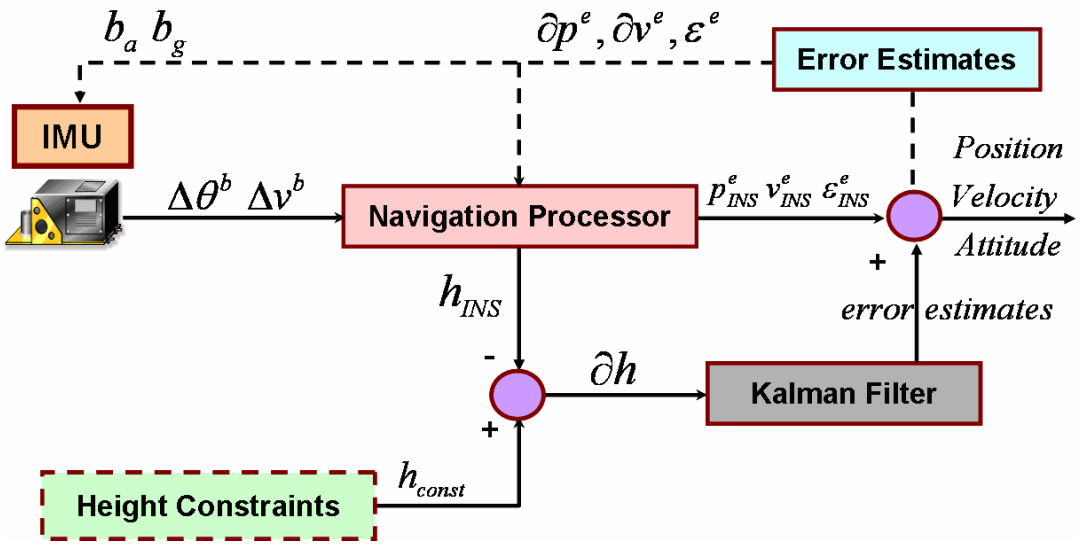

Figure 4.6: Height Constrained Navigation Block Diagram

This Kalman filter uses the differences between the INS-derived height and the virtual height measurements to compensate for INS errors. The system error states are in the ECEF frame, while the measurement is in the LLF. So, the relation between the measurements and system states is not linear, and thus, a measurement model is required which is derived in the following section.

4.4.2.1 Measurement Model

The measurement model is obtained by perturbing the equations relating the geodetic and Cartesian coordinates, which is given by Equation (4.35) (Farrell & Barth 2001):

$$
\begin{aligned}
r_x &= (N+h)\cos\lambda\cos\phi \\
r_y &= (N+h)\cos\lambda\sin\phi \\
r_z &= (N(1-e^2)+h)\sin\lambda
\end{aligned}
\tag{4.35}
$$

where,

r_x, r_y, r_z	are the Cartesian coordinates,
ϕ, λ, h	are the latitude, longitude and height,
N	is the Prime Vertical radius, and
e	is the eccentricity.

For brevity, the complete derivation is omitted, and only the end result is shown, which is given by Equation (4.36):

$$
\begin{bmatrix} \delta r_x \\ \delta r_y \\ \delta r_z \end{bmatrix} = \underbrace{\begin{bmatrix} A\cos\phi\cos\lambda - (N+h)\sin\phi\cos\lambda & -(N+h)\cos\phi\sin\lambda & \cos\lambda\cos\phi \\ A\cos\phi\sin\lambda - (N+h)\sin\phi\sin\lambda & (N+h)\cos\phi\cos\lambda & \sin\lambda\cos\phi \\ A(1-e^2)\sin\phi + N(1-e^2)\cos\phi + h\cos\phi & 0 & \sin\phi \end{bmatrix}}_{H} \begin{bmatrix} \delta\phi \\ \delta\lambda \\ \delta h \end{bmatrix} \tag{4.36}
$$

where 'δ' represents the perturbations and A is a term given by Equation (4.37):

$$
A = \frac{-ae^2\sin\phi\cos\phi}{\sqrt{(1-e^2\sin^2\phi)^3}} \tag{4.37}
$$

The final measurement design matrix is given by the last row of the inverse of the H matrix in Equation (4.36), and is given by Equation (4.38):

$$
H(h) = \begin{bmatrix} (H)^{-1}_{3,1} & (H)^{-1}_{3,2} & (H)^{-1}_{3,3} & 0_{1\times(n-3)} \end{bmatrix} \tag{4.38}
$$

The misclosure vector is computed using Equation (4.39):

$$
\delta h = \begin{bmatrix} h_{const} - h_{INS} \end{bmatrix} \tag{4.39}
$$

The measurement noise matrix for these measurements depends on how the virtual height measurements are derived. If the height is fixed to a predefined value, then the measurement noise depends on knowledge of the actual height variation for a particular region. If the height is constrained to a value computed just before going into a GPS outage, then the measurement noise can be set to a relatively low value (0.5-1 m), assuming a short outage duration (30-40 s).

Figure 4.5 and Figure 4.6 depict the navigation block diagrams when a complete GPS outage occurs. However, if the GPS outage is partial, the navigation block diagram is more aptly represented by Figure 4.7 (assuming a tightly coupled GPS/INS integration scheme).

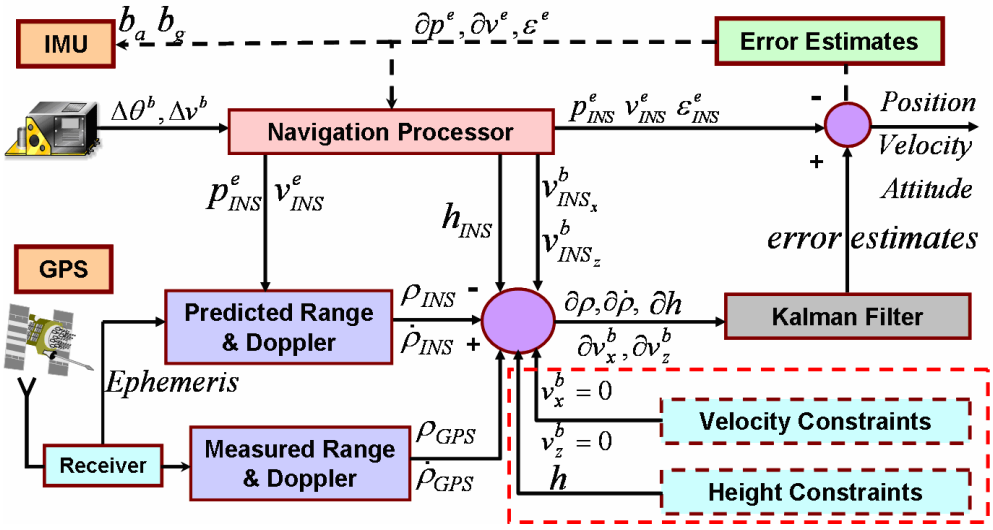

Figure 4.7: Filter Designs When Constraints are used

In this case the measurement design matrix is represented by a combination of Equations (4.13), (4.33) and (4.38). The misclosures vector is constructed using Equations (4.14), (4.34) and (4.39).

4.5 External Heading Aiding

To facilitate the dynamic alignment of an INS (using heading from GPS as per Equation (2.33)), or else to incorporate external heading measurements into the INS computations (for instance from a magnetometer), a heading error dynamics equation is required which relates the measurements to the system error states. Such an error equation is derived based on the knowledge that heading is computed using Equation (2.19), (repeated here for convenience):

$$\hat{\psi} = \tan^{-1}\left(\frac{(R_b^l)_{1,2}}{(R_b^l)_{2,2}}\right) \tag{4.40}$$

The rotation matrix from the b-frame to the l-frame is given by Equation (4.41):

$$R_b^l = R_e^l \times R_b^e \tag{4.41}$$

Given Equation (4.41), Equation (4.40) in terms of misalignment error states can be rewritten as Equation (4.42):

$$\hat{\psi} = \tan^{-1}\left(\frac{N_\psi}{D_\psi}\right) = \tan^{-1}\left(\frac{n_1\varepsilon_x + n_2\varepsilon_y + n_3\varepsilon_z + n_4}{d_1\varepsilon_x + d_2\varepsilon_y + d_3\varepsilon_z + d_4}\right) \tag{4.42}$$

where, ' N_ψ ' and ' D_ψ ' represent the numerator and denominator, respectively. The terms $n_{1..4}$ and $d_{1..4}$ are computed as follows:

$$n_1 = (R_e^l)_{13}(R_b^e)_{22} - (R_e^l)_{12}(R_b^e)_{32} \qquad d_1 = (R_e^l)_{23}(R_b^e)_{22} - (R_e^l)_{22}(R_b^e)_{32}$$
$$n_2 = (R_e^l)_{11}(R_b^e)_{32} - (R_e^l)_{13}(R_b^e)_{12} \qquad d_2 = (R_e^l)_{21}(R_b^e)_{32} - (R_e^l)_{23}(R_b^e)_{12}$$
$$n_3 = (R_e^l)_{12}(R_b^e)_{12} - (R_e^l)_{11}(R_b^e)_{22} \qquad d_3 = (R_e^l)_{22}(R_b^e)_{12} - (R_e^l)_{21}(R_b^e)_{22}$$
$$n_4 = (R_e^l)_{11}(R_b^e)_{12} + (R_e^l)_{12}(R_b^e)_{22} + (R_e^l)_{13}(R_b^e)_{32} \quad d_4 = (R_e^l)_{21}(R_b^e)_{12} + (R_e^l)_{22}(R_b^e)_{22} + (R_e^l)_{23}(R_b^e)_{32}$$

In light of Equation (4.42), the heading error equation can be expressed as Equation (4.43):

$$\delta\hat{\psi} = \frac{\partial\hat{\psi}}{\partial\varepsilon_x}\varepsilon_x + \frac{\partial\hat{\psi}}{\partial\varepsilon_y}\varepsilon_y + \frac{\partial\hat{\psi}}{\partial\varepsilon_z}\varepsilon_z \tag{4.43}$$

such that,

$$\frac{\partial\hat{\psi}}{\partial\varepsilon_x} = \frac{N_\psi n_1 - D_\psi d_1}{N_\psi^2 + D_\psi^2}, \qquad \frac{\partial\hat{\psi}}{\partial\varepsilon_y} = \frac{N_\psi n_2 - D_\psi d_2}{N_\psi^2 + D_\psi^2}, \qquad \frac{\partial\hat{\psi}}{\partial\varepsilon_z} = \frac{N_\psi n_3 - D_\psi d_3}{N_\psi^2 + D_\psi^2}.$$

The measurement design matrix for external heading measurements can thus be written as given by Equation (4.44):

$$H(\psi) = \left[0_{1\times3} \quad 0_{1\times3} \quad \frac{\partial\hat{\psi}}{\partial\varepsilon_x} \quad \frac{\partial\hat{\psi}}{\partial\varepsilon_y} \quad \frac{\partial\hat{\psi}}{\partial\varepsilon_z} \quad 0_{1\times(n-9)} \right] \tag{4.44}$$

The misclosures vector is computed using Equation (4.45):

$$\delta\psi = \left[\psi_{GPS/External} - \psi_{INS}\right] \tag{4.45}$$

4.6 Software Development

The GPS/INS integrated system software for data processing was developed in a C++ class environment. The software has a GPS processing module, an INS processing module, an integration module, an error compensation module, and a backward smoothing module.

The GPS processing module uses the filter design discussed in Section 4.2 for computing the navigation solution. Processing can either be done in single-differenced or double-differenced mode. All of the results presented in this thesis were generated using single

differencing mode (Section 2.1.3). The INS module implements the INS mechanization as discussed in Section 2.2.2. The INS filter state model is flexible in nature, where different sensor error characterization states can be switched on or off depending on the quality of the IMU being used (Section 4.3).

The integrated navigation module implements both loosely (Section 4.1.1) and tightly coupled (Section 4.1.2) integration schemes for reducing the inertial and GPS data, using a closed loop approach (Section 4.1.3). The error compensation module utilizes the vehicle motion constraints during GPS outages, as discussed in Section 4.4. The logic switches in the software allows the filter to switch between various filter designs (Figure 4.1, Figure 4.2, Figure 4.7, etc.), depending on GPS availability.

The backward smoothing module of the software uses the Rauch-Tung-Streibel (RTS) (discussed in Chapter Seven) smoother to smooth the forward solution. The smoother is run once the forward filter processing is over (i.e. post mission).

CHAPTER FIVE : OPEN AREA RESULTS

This chapter quantifies the performance of the integrated system for open area applications. The chapter begins with a description of the field tests where the specific details about the test set-up, sensors, operating environment and the procedures adopted for data collection are discussed. The results obtained with open area data set are then presented which includes the position/velocity error results obtained through integration of DGPS with MEMS and tactical grade IMU using various integration strategies and filters. The performance of the error compensation algorithms is evaluated by simulating the GPS outages through the rejection of GPS satellites in post-processing.

5.1 Field Test Description

Field test runs were carried out in Calgary, Alberta in January 2005 over a period of four days. The tests were carried out in different operating conditions, characterized based on GPS satellite visibility.

5.1.1 Sensors and Equipments

As stated earlier, the MEMS IMU being used in this study is the Crista IMU from Cloud Cap Technology Inc. This IMU is designed to optimize both price and performance in a GPS/INS integration system (Crista- Interface/Operation Document 2004), and is available in single quantities for under $2000 US. It is a six axis measurement system consisting of three MEMS gyroscopic rate sensors and accelerometers providing temperature compensated inertial data, at a rate greater than 200 Hz. It has a built-in GPS pulse per second (PPS) interface which facilitates the accurate time synchronization of

IMU and GPS data. The IMU is small in size (2.05”x 1.50”x1.00”) and weighs only 36.8 grams.

Apart from the MEMS IMU, a navigation grade Honeywell Commercial IMU (CIMU embedded into the Applanix POS/LS system) and a tactical grade Honeywell HG1700 IMU (embedded into the NovAtel BDS system) are also used. So the inertial data was collected with three different grades of IMUs. The motivation behind using the CIMU was to be able to generate a precise reference solution to facilitate a comparative analysis. The HG1700 IMU was used to allow for a performance comparison with the MEMS IMU. The HG1700 and CIMU data were time tagged internally by the GPS receivers (embedded) in the BDS and POS/LS systems before being output. This eliminates any significant timing errors between the GPS and IMU data (Petovello et al 2003). The Crista IMU data was time tagged through a PPS signal from the OEM4 receiver to its PPS interface. The IMUs are shown in Figure 5.2 while technical characteristics of each IMU were presented earlier in Table 1.1.

The GPS reference station (for differential GPS) was equipped with a dual-frequency NovAtel OEM4 receiver connected to high performance NovAtel 600 antenna, and was set up at different places for different test runs. At the remote station, a total of four NovAtel 600 GPS antennas were used. These antennas were arranged in a rectangular pattern, as shown in the test setup shown in Figure 5.1 and Figure 5.2.

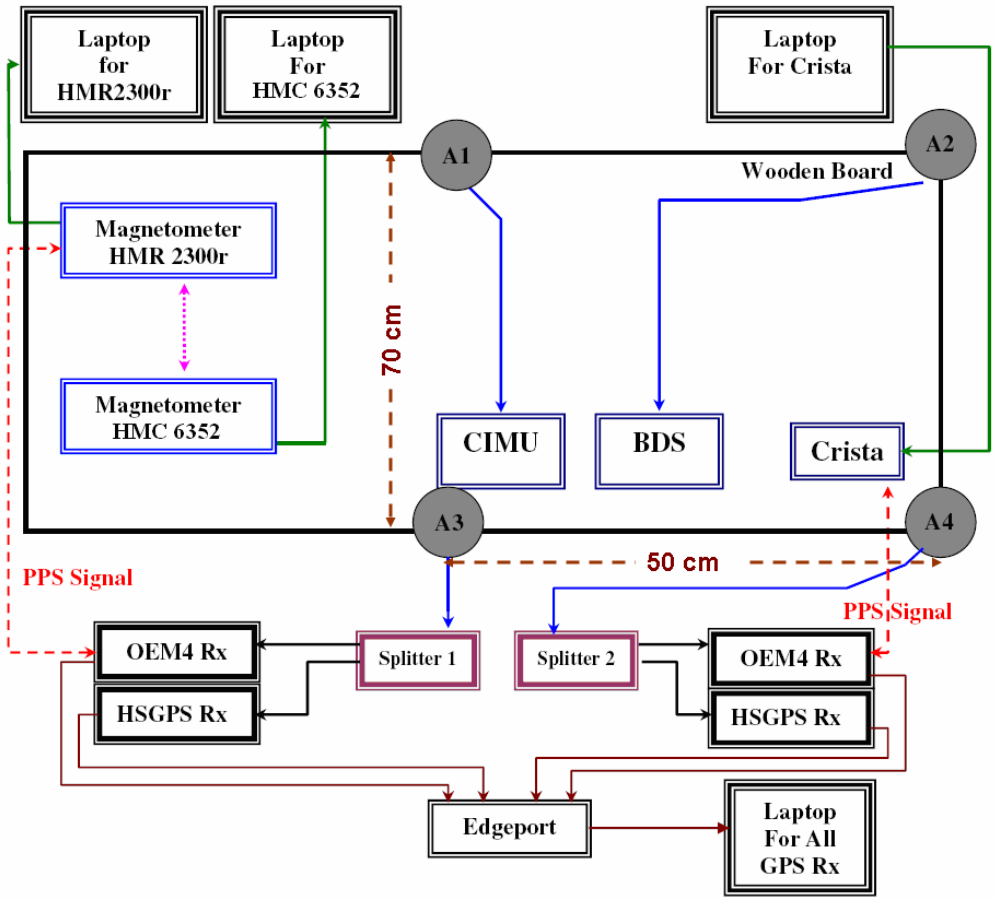

Figure 5.1: Remote Station Setup for Data Collection

Two of the antennas were connected to the OEM4 receiver embedded in the POS/LS (A1) and BDS system (A2). The other two antennas A3 and A4 were each connected to one OEM4 and one SiRF High Sensitivity XTrac receiver, through a signal splitter. The primary reason for using two separate NovAtel OEM4 receivers (connected to A3 and A4) was to time tag the Crista and magnetometer data, through their PPS interface. The OEM4 receiver connected to A3 collected data at 10 Hz, while the one at A4 collected at 1 Hz. Both XTrac receivers collected data at 1 Hz.

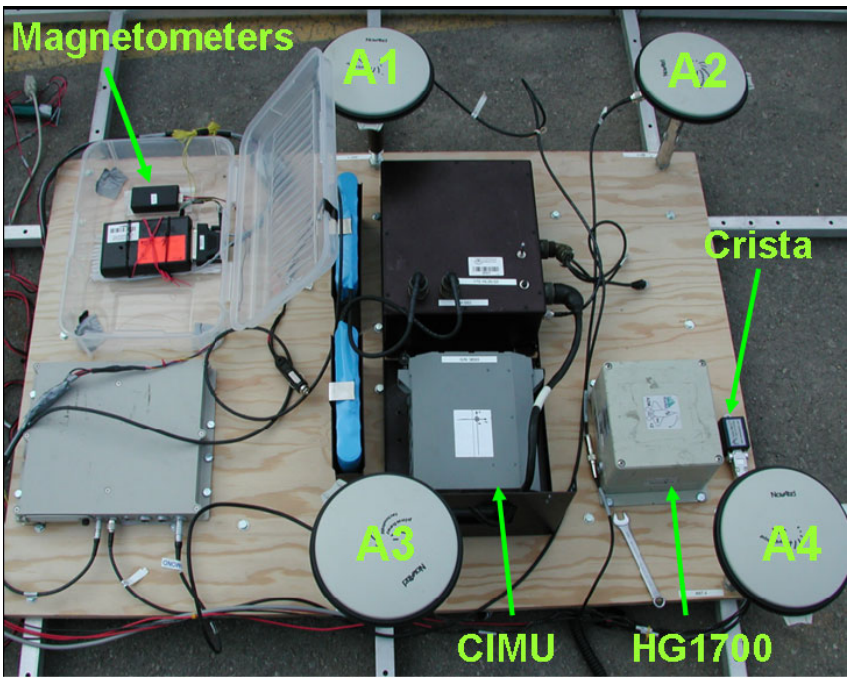

Figure 5.2: Test Set Up

Each sensor was fixed rigidly on a wooden board which was mounted on the top of the University of Calgary's test van (Dodge Grand Caravan) in an attempt to reduce the length of the lever arms between the GPS antenna and the INS. Data collection for each test began with a static initialization period of about 12-15 minutes followed by about 20–25 minutes of driving. Static data was collected in the beginning to facilitate the initial alignment of the IMUs. The total duration of each test was 35-40 min. For the test results presented in this thesis, the OEM4 receiver connected to Antenna A4 is used to integrate with all the IMUs, unless specified otherwise.

5.1.2 Open Area Test Description

Several tests were carried out to the West of the Calgary, near the Springbank Airport, which is a relatively open area with a clear view of the sky, and thus provided good

satellite visibility (Figure 5.3). One data set will be used for results discussion in this chapter. The GPS reference station for this test was set up at one of the accessible pillars in the test area.

Figure 5.3: Open Area Test Environment

The test run trajectory was designed to have a lot of turns as well as straight route travels to represent different dynamics a land vehicle may have. The trajectory is shown in Figure 5.4. Also shown is the zoomed version of some portions of the trajectory for visibility. The total distance traveled was 6-7 km, and the baseline length to the reference station varied between 0-2 km. The distance of the vehicle from the reference station is small, thus, the residual, baseline-dependent, errors after GPS differential corrections will be small.

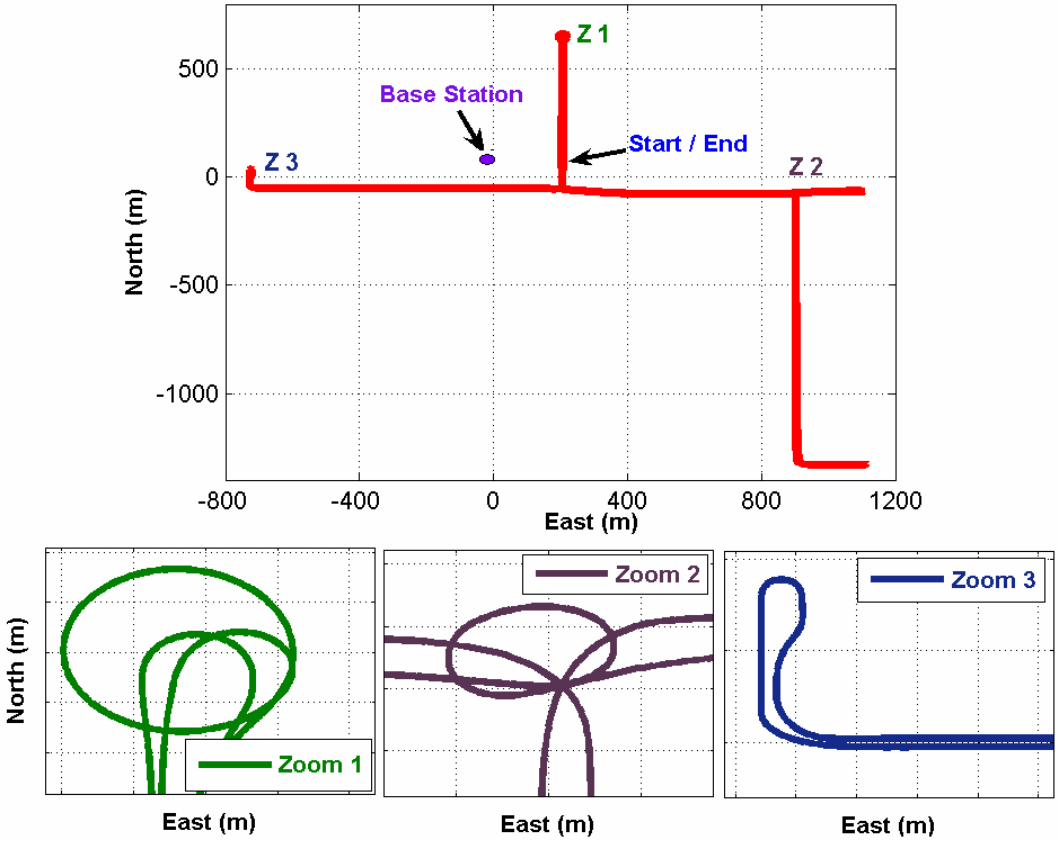

Figure 5.4: Open Area Test Trajectory

5.2 Reference Navigation Solution

To facilitate a performance comparison analysis, a reference navigation solution is required. Here, the integrated solution obtained using the navigation grade CIMU was used as the reference. The CIMU data was processed using the Position and Orientation System Post Processing Package (POSPac), from Applanix Corporation. The software compensates for sensor and environmental errors, and computes the optimally accurate, blended, and smoothed navigation solution (PosPac Product Manual, Applanix Corporation 2001). All the three GPS measurements, namely code, Doppler, and carrier phase measurements were used in the processing. The navigation solution obtained in this

way is therefore accurate to better than 1.5 cm (horizontal) and 4 cm (vertical), and hence will be used as reference for all the analysis presented herein. The obtained reference trajectory was shown earlier in Figure 5.4.

5.3 GPS-Only Solution

In order to assess the performance of the integrated system, it is necessary to examine the performance of the aiding source, which is primarily GPS. Thus, this section quantifies the accuracy of the navigation solution available from the OEM4 receiver. The data was processed with the GPS-module of the developed software, which uses single-differenced GPS pseudorange and Doppler measurements.

The availability of the GPS solution is 100 % as the data was collected under benign operational conditions, with the average number of satellites tracked being around 9. Figure 5-5 shows the satellite geometry and number of satellites available for computing a solution during the selected test run. The horizontal and vertical Dilution of Precision (DOP) values are seen to be less than two for the majority of time, implying good satellite geometry. A few jumps can be seen which is caused by loss of lock on one of the satellites, which demonstrates the DOPs correlation with satellite visibility.

Table 5.1 presents a statistical summary of the position and velocity errors in the GPS-only solution. As can be seen, the horizontal position error in the GPS-only solution remains within 39 cm with a maximum value of 1 m, while the horizontal velocity error is around 9 cm/s with a maximum value of 24 cm/s. Given the quality of the OEM4

receiver (refer to Section 2.1.3.6) and the operating conditions, the sub-metre level accuracies with pseudorange/Doppler measurements are not surprising. Since, the accuracy of the integrated system depends on the accuracy of the GPS solution; a similar accuracy level can be expected from the integrated solution as well.

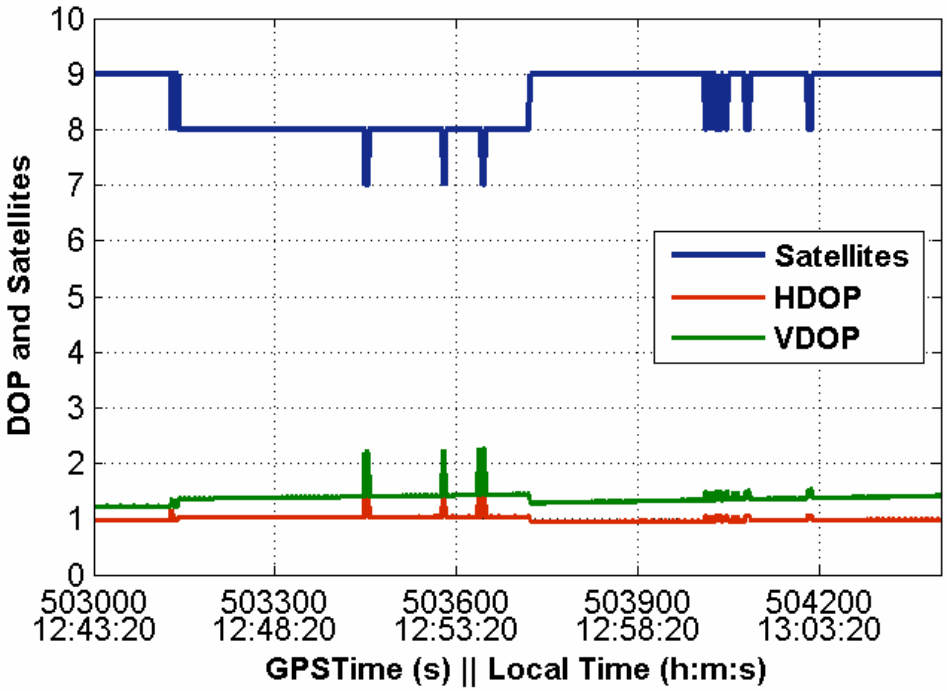

Figure 5.5: Satellite Geometry and Availability

Table 5.1: OEM4: GPS-only RMS Position and Velocity Errors

Max	***North***	***East***	***Up***	***2D***	***3D***
Position (m)	0.89	0.96	0.77	1.02	1.17
Velocity (m/s)	0.243	0.178	0.281	0.244	0.286
RMS	***North***	***East***	***Up***	***2D***	***3D***
Position (m)	0.27	0.29	0.31	0.40	0.5
Velocity (m/s)	0.068	0.060	0.059	0.091	0.108

5.4 Analysis Strategy

The results presented in this thesis are all obtained through processing with the developed GPS/INS integration software described earlier in Section 4.6. The following performance parameters for both Crista and HG1700 IMU will be investigated in this chapter:

- Position/velocity/attitude accuracy using loosely and tightly coupled integration scheme, in a closed loop integration approach. This analysis is conducted under full satellite visibility, i.e. under ideal GPS conditions, and thus also serves to verify the validity of different algorithms and the integration strategy implementation.

- Accuracy of the stand-alone INS when complete GPS outages occur under varying vehicle dynamics. Since the satellite visibility is good (see Figure 5.5), GPS outages will be simulated by rejecting satellites during processing. Processing will be done with and without vehicle motion constraints. This helps to assess the improvements that can be achieved through constrained navigation.

- Accuracy of the integrated system under partial GPS outages, with and without vehicle motion constraints. A partial outage is defined as the periods when GPS satellite signals are blocked such that fewer than four satellites are available. The results when two- and three-satellites are available for updating the INS will be presented.

The results are primarily discussed in terms of position and velocity errors which are computed using the reference solution (obtained as discussed in Section 5.2). Since the reference trajectory is accurate to the centimetre-level, the resulting position difference is almost entirely due to errors in the designed integrated system. The error results are mostly discussed in the RMS sense, where 1D, 2D, and 3D RMS errors are computed. The corresponding probability level for each accuracy measure is listed in Table 5.2.

Table 5.2: Performance Parameters Probability Level (van Digglen 1998)

Dimension	*Accuracy Measure*	*Probability (%)*
1D	RMS	68
2D	RMS	63 – 68
3D	RMS	61 – 68

5.5 GPS/INS Integration Results

This section discusses the results obtained through integration of the OEM4 receiver with the Crista and HG1700 IMUs. The results are divided into several sections as per the analysis strategy outlined in Section 5.4.

5.5.1 No GPS Outage Results

The results presented in this section are obtained when pseudorange/Doppler derived GPS updates are available at the rate of 1 Hz. The output rate of the INS is set to 10 Hz, which means there is one GPS update for every ten INS outputs. Between GPS updates, the INS operate in prediction mode (refer to Section 4.3.2.3). However, given such a short duration of INS prediction (< 1 s), the GPS availability is considered to be continuous. The Crista IMU data is processed with the 15-state and 27-state filters,

whereas for the HG1700, a simple 15-state filter is used. This serves to quantify the possible benefits that can be gained through 27-state filter. The 27-state filter is not used with the HG1700 IMU, as the turn-on biases and scale factor errors for this IMU are negligible (refer to Table 1.1). Each IMU dataset is processed using both the closed-loop loosely coupled and tightly coupled integration schemes. This helps in the performance comparison of the two integration strategies under favourable operational conditions.

5.5.1.1 Position Accuracy

Figure 5.6 compares the position RMS errors obtained with the Crista and HG1700 IMUs, with the loosely coupled integration strategy (Figure 4.1). Table 5.3 lists the corresponding position RMS errors.

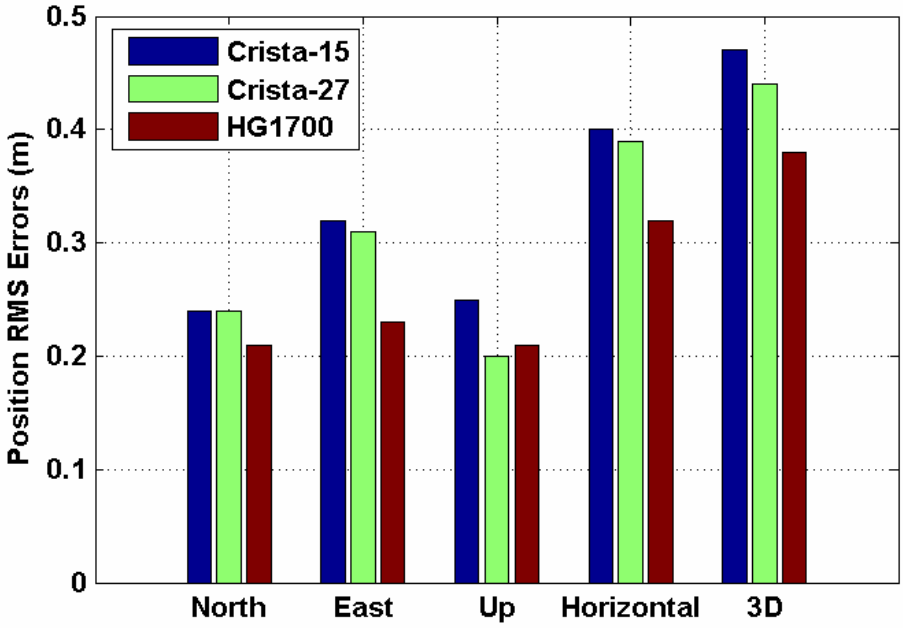

Figure 5.6: 2D Position RMS Error Comparison (LC)

Table 5.3: Position RMS Errors (LC)

LC	*North*	*East*	*Up*	*2D*	*3D*
Position	***(m)***	***(m)***	***(m)***	***(m)***	***(m)***
Crista 15	0.24	0.32	0.25	0.40	0.47
Crista 27	0.24	0.31	0.20	0.39	0.44
HG1700	0.21	0.23	0.21	0.32	0.38

Since the GPS availability is good throughout the run, the INS navigation parameters get corrected continuously, which prevented the errors from accumulating which in turn leads to a sub-metre level of accuracy using both IMUs. The horizontal position errors in the solution obtained from the Crista IMU remains within 39 cm and that for the HG1700 within 32 cm. The obtained accuracy is actually limited by the accuracy of the GPS pseudorange/Doppler solution and the type of IMU used.

In the case of the Crista IMU, the performance improves very little with the 27-state filter as compared to the 15-state filter. The errors are seen to reduce by just 1 cm (2D) and 3 cm (3D). This is because of the continuous correction of the INS errors, which does not allow errors to grow to a level to indicate any significant improvement in performance. The performance of the 27-state filter could be best quantified during GPS outages which will be subsequently discussed. Although from Figure 5.7, it can be noted that the trajectory became smoother when a 27-state filter is used. Since the filter operates in prediction mode between GPS updates, with a 15-state filter, the error during this period accumulates at a faster rate because of improper sensor error compensation, leading to a saw tooth like behaviour which combined with azimuth errors, gets more pronounced at

turns. However with a 27-state filter, the errors are well compensated which prevented error accumulation leading to a smoother and more accurate trajectory.

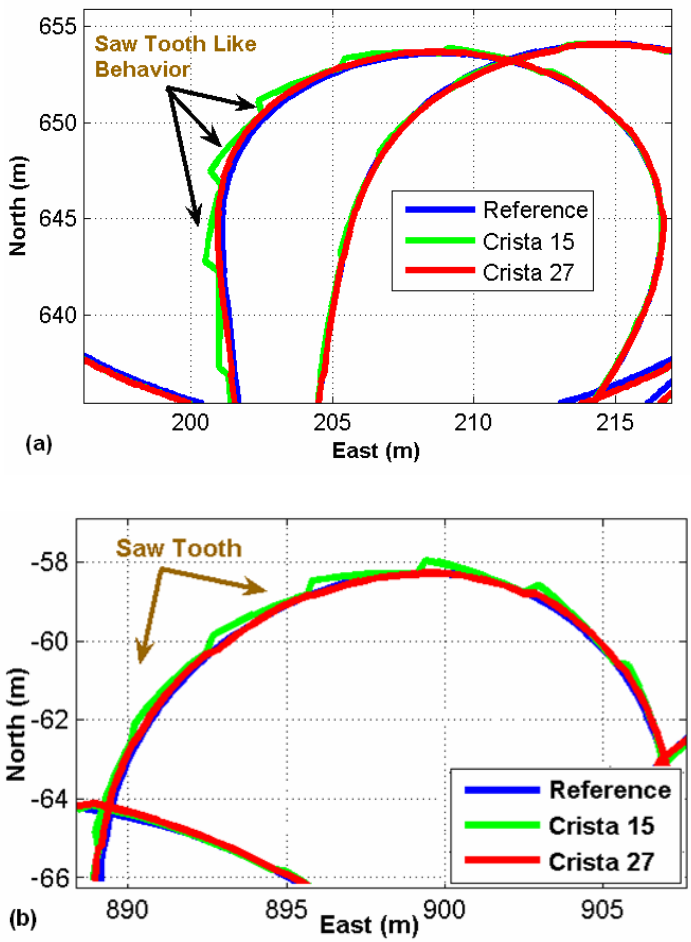

Figure 5.7 (a-b): Part of Trajectory Zoomed Around Turns (LC)

Alternatively, the improvement brought to the integrated system by the 27-state filter can be assessed by looking at the Kalman filter innovation sequence, which is the difference between the INS predicted position and the GPS computed position (in the case of loose coupling, i.e. Equation (4.27)), and is shown in Figure 5.8. The innovation sequence basically signifies the combined errors of INS and GPS (Hide 2003). However, as discussed in Section 5.3, the GPS satellite availability is good during the test run, and the

GPS accuracies are supposedly consistent through the test run, so any inconsistency in the innovations are assumed to be the contribution of INS. The position innovation sequence with a 27-state filter is smaller as compared to the 15-state filter, indicating un-modeled errors in the latter. Some spikes can be noted which primarily occur during turning manoeuvres and are mainly due to un-modeled bias and scale factor errors. These spikes are not visible with a 27-state filter indicating superior performance.

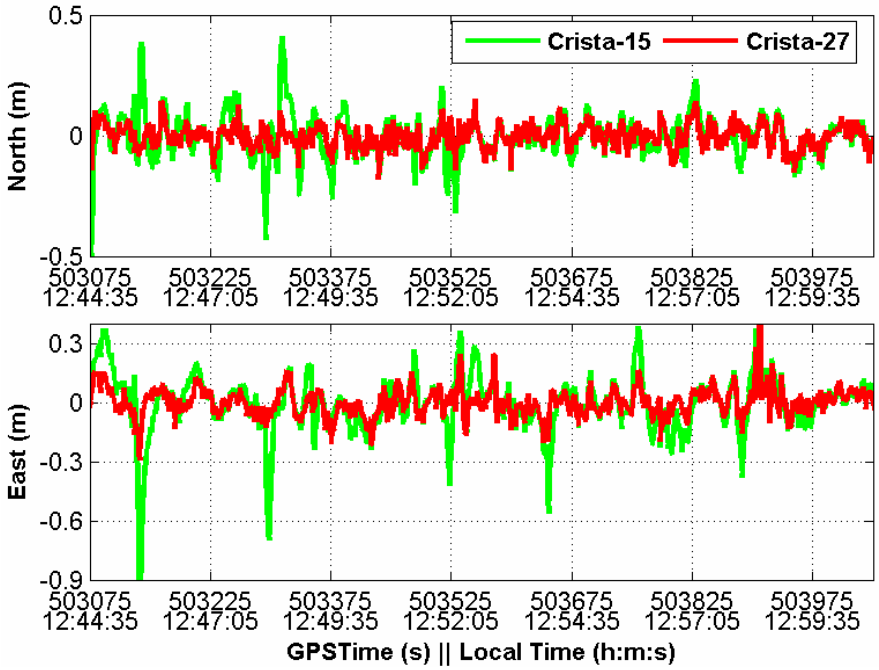

Figure 5.8: Position Innovation Sequences (LC)

Table 5.4 lists the position RMS errors obtained with the Crista and HG1700 IMUs, with a tightly coupled integration strategy (Figure 4.2). The error results for this strategy are similar to the loosely coupled case (refer to Table 5.3), with differences limited to mm-level.

Table 5.4: Position RMS Errors (TC)

LC	*North*	*East*	*Up*	*2D*	*3D*
Position	***(m)***	***(m)***	***(m)***	***(m)***	***(m)***
Crista 15	0.24	0.32	0.23	0.40	0.46
Crista 27	0.23	0.31	0.20	0.39	0.44
HG1700	0.22	0.23	0.22	0.32	0.39

5.5.1.2 Velocity Accuracy

This section quantifies the velocity errors under benign operational conditions. Although velocity results follow from the position errors, since positions are obtained through the integration of velocities, these errors are discussed separately for completeness and clarity. Table 5.5 lists the velocity errors obtained with loose coupling.

Table 5.5: Velocity RMS Errors (LC)

	North	*East*	*Up*	*2D*	*3D*
Velocity	***(m/s)***	***(m/s)***	***(m/s)***	***(m/s)***	***(m/s)***
Crista 15	0.113	0.099	0.070	0.150	0.166
Crista 27	0.073	0.055	0.052	0.091	0.105
HG1700	0.015	0.014	0.014	0.021	0.025

As can be seen, the HG1700 IMU horizontal velocity is accurate to few a centimetres, while with the Crista 15-state filter, these errors are up to the decimetre level. In comparison to GPS-only velocity accuracies (see Table 5.1) these errors are quite large, and thus indicate un-modeled errors. With the 15-state filter the accelerometer data is contaminated with unresolved sensor errors. Therefore, between GPS updates the error increases rapidly leading to large errors in the velocity solution. This fact is also

confirmed by the velocity innovation sequences (Figure 5.9) which is specifically large for the 15-state filter, having frequent spikes. With the 27-state filter, the innovations are smaller and also the velocity results improve. The errors reduce by about 6 cm/s which are an improvement of about 40 % relative to the 15-state filter.

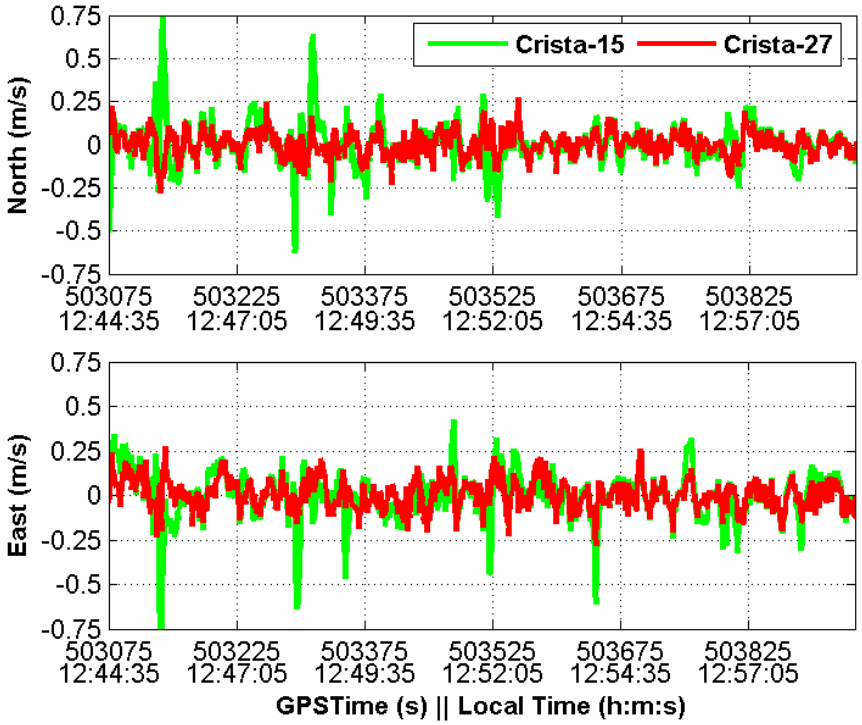

Figure 5.9: Velocity Innovation with Crista IMU (LC)

In the case of the HG1700 IMU, the magnitude of the innovations remains within ±10 cm/s throughout, which can be seen in Figure 5.10 (note the change in scale relative to Figure 5.9). This indicates that the predictions made by the INS are very accurate such that very little new information is provided by GPS into the system. Thus, the velocity accuracies depend more on INS and lesser on GPS, leading to superior accuracies than GPS.

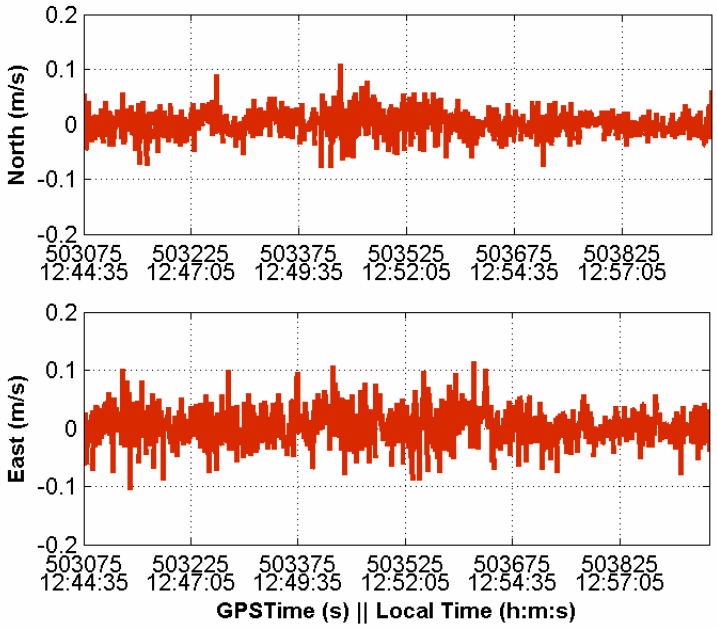

Figure 5.10: Velocity Innovations with HG1700 IMU (LC)

As in the case of the position error, the trends and magnitude of velocity errors in the tightly coupled case are similar to the loosely coupled case, which can be noted from Table 5.6.

Table 5.6: Velocity RMS Errors (TC)

	North	***East***	***Up***	***2D***	***3D***
Velocity	***(m/s)***	***(m/s)***	***(m/s)***	***(m/s)***	***(m/s)***
Crista 15	0.111	0.097	0.066	0.148	0.162
Crista 27	0.073	0.053	0.052	0.090	0.104
HG1700	0.015	0.015	0.014	0.021	0.026

5.5.1.3 Attitude Accuracy

This section discusses the attitude error under benign operating conditions. The roll and pitch were initialized with a value of 1˚ (defined empirically); while the initial heading

value was fixed through values obtained from other high grade IMUs. Figure 5.11 shows the attitude errors obtained through the 27-state filter.

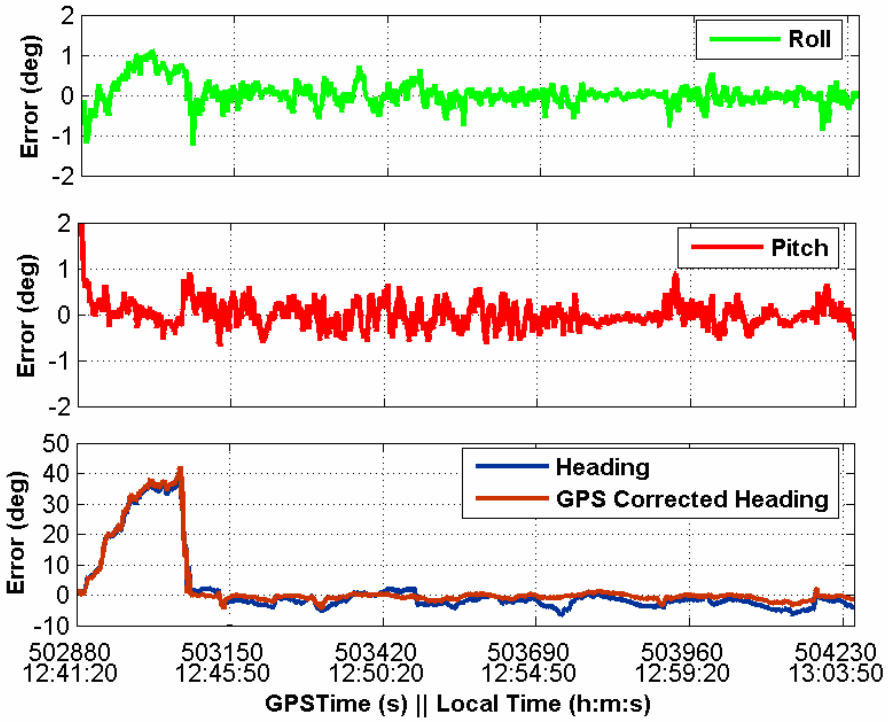

Figure 5.11: Crista IMU Attitude Errors (27-state, LC)

As can be noted, in roll and pitch, the initial errors are at the 1˚- 2˚ level. This is because their initial value was fixed. However, as soon as ZUPTs/GPS updates become available, these values converge such that the error stays near zero. In the case of heading, the error increases rapidly until the GPS time 503060 s and it converges after that. This is because for approximately 180 s into the processing, the vehicle remains stationary. In the absence of horizontal acceleration, the heading errors are not-observable and thus the error grows. When the vehicle starts moving (at GPS time 503060 s) the heading converges within 25-30 s; however, the converged value, owing to large sensor noise and poor observability, is seen to have large errors.

One way to improve heading estimation accuracy, and to expedite the heading convergence, is to explicitly use GPS-derived heading (Equations (2.34)) as the external heading measurement. The results obtained through GPS-derived heading are also plotted in Figure 5.14. Figure 5.12 specifically shows the heading errors during the first 150 s, after the vehicle starts moving.

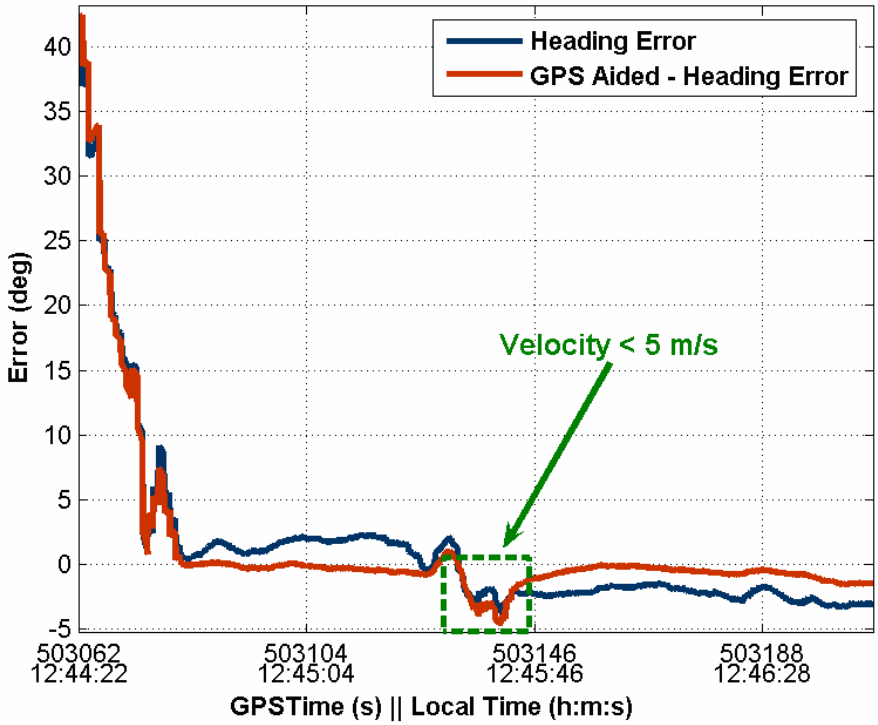

Figure 5.12: Heading Error Zoomed (showing first 150 s)

As can be seen, although both the headings converge around the same time, the convergence is more accurate when GPS-derived heading is used. To this end, the regular addition of a GPS-derived heading significantly reduces the INS drift in the heading estimation. Unfortunately, these GPS-derived measurements are available only intermittently, i.e. whenever the vehicle speed exceeds 5 m/s. During periods of lower velocity, the error increases which is evident from Figure 5.12.

Table 5.7 presents a statistical summary of attitude errors for various integration systems. The table shows that the use of the 27-state filter provides significant improvements over the 15-state filter. However, relative to a tactical grade HG1700 IMU, these errors are still very high. The table also shows that GPS can effectively be used to prevent drift in heading estimation. The errors are reduced by about 50-70 % with different filters when GPS-derived headings are used as external measurements.

Table 5.7: Attitude RMS Errors (LC)

RMS	***Roll***	***Pitch***	***Heading***	***GPS Heading Aiding***
Processing	***deg (˚)***	***deg (˚)***	***deg (˚)***	***deg (˚)***
Crista 15	0.486	0.493	5.37	1.65
Crista 27	0.205	0.243	2.68	1.16
HG1700	0.026	0.027	0.17	-

5.5.2 Complete GPS Outage Simulation Results

The advantages of integrating GPS with INS generally come into play when GPS signals are blocked and/or subject to degradation due to multipath. To demonstrate the ability of inertial sensors during these times, eight 30 s GPS gaps were simulated in the data by artificially omitting the satellites during post processing. These gaps were carefully selected to represent varying vehicle dynamics, including outages on straight route travel (three) and during turns (five). The periods of simulated GPS outages are marked in Figure 5.13.

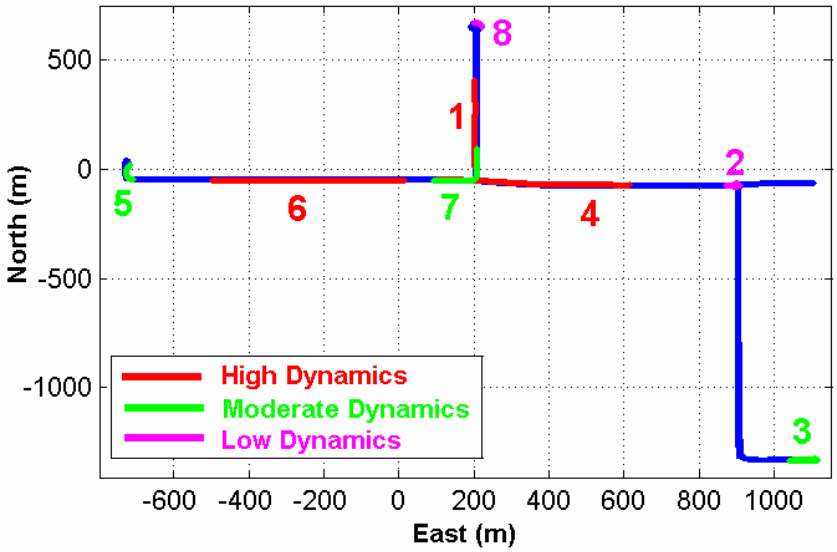

Figure 5.13: Trajectory with Simulated Data Outages

To begin the analysis, the Crista IMU data was first processed with both the 15- and 27-state filters (using tightly coupled integration strategy) without using the vehicle motion constraints. The purpose was to obtain a baseline performance of the integrated systems during GPS gaps. The results obtained using the vehicle motion constraints (discussed in next section) could then be compared to this performance to assess the percentage improvements in the navigation solution. HG1700 data is also processed with identical outage conditions to facilitate a comparative analysis with the Crista IMU.

To assess the positioning capability of each IMU during data outages, the position errors are computed (with respect to the reference solution) as a function of time since the last GPS update for each simulated outage. Using the resulting eight error time series (i.e. one for every outage simulated), the RMS time series across all data gaps was computed. In this way, a statistical assessment of the error as a function of time is obtained (Petovello 2003).

5.5.2.1 No Constraints

During GPS gaps, the filter works in prediction mode and thus the performance of integrated system is defined primarily by the INS. The effectiveness of INS during this period depends on the vehicle dynamics, the quality of the sensor error compensation, and the time-span of the GPS outage. Figure 5.14 shows the position errors for each IMU during individual outages.

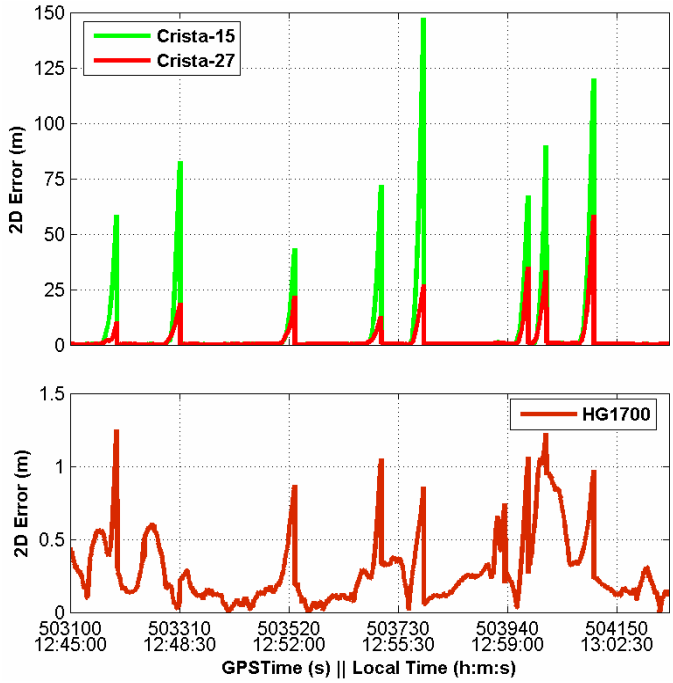

Figure 5.14: Position Errors during Individual Outages (30 s)

In the absence of the aiding source, errors in the INS velocity start to grow. Since the velocities are integrated to obtain positions, the position error grows. As can be seen in Figure 5.14, the performance of the Crista IMU with a 15-state filter degrades rapidly during GPS outages, with maximum horizontal errors varying from 40 m to up to 150 m over different outages. However, with the 27-state filter these errors are confined to a

maximum of 10-60 m, thus indicating substantial improvements over the 15-state filter. Figure 5.15 shows the RMS position error (as a function of time) computed across all the outages. As noted, the maximum RMS error with a 15-state filter goes up to 92 m (2D) in 30 s without GPS updates. With a 27-state filter these errors are reduced to less than 31 m, marking an improvement by about 67 % over the 15-state filter.

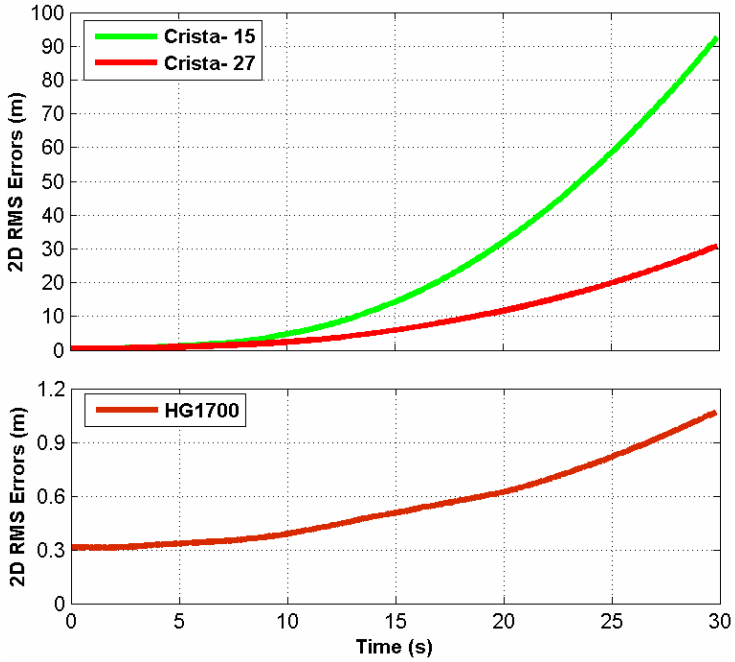

Figure 5.15: RMS Position Error Computed Across all Outages (30 s)

The primary reason for the difference in performance of the two filters is seen to be the tilt error. During a GPS outage, the IMU measurements are mechanized to obtain the vehicle attitude and velocity solutions. The attitude solution during a GPS outage depends largely on the quality of the gyro measurements. These measurements have a large error, which with a 15-state filter does not get compensated leading to large errors in the attitude estimates. The errors in the heading estimate cause velocity error growth because of the projection of the forward velocity component in the lateral directions,

while the errors in roll and pitch (tilt errors) contribute to the velocity errors by projecting the very strong gravity signal ($9.8\ m/s^2$) in the horizontal direction (refer to Appendix B for a discussion on the north, east, and up velocity error dynamics). Since the error in velocity is integrated to obtain position, this eventually leads to large errors in the position solution (Equation (2.24)). Figure 5.16 shows the tilt errors with the 15- and 27-state filters. As can be seen, in the absence of GPS the errors in roll and pitch accumulate, reaching the 3-4˚ level in 30 s with a 15-state filter. However, with a 27-state filter these errors are limited to less than 1˚. This difference is thus the main reason for the superior performance of the 27-state filter.

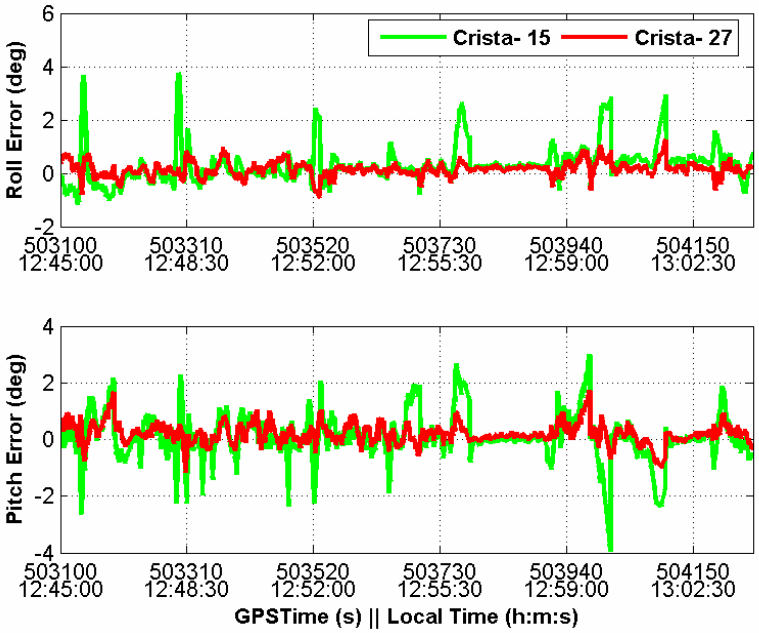

Figure 5.16: Tilt Errors with Crista IMU

The performance of the HG1700 IMU is significantly superior as compared to the Crista IMU with maximum errors limited to around 1.1 m after a 30 s outage duration. This is

due to the high quality Ring Laser Gyro (RLG) sensors which keep the attitude errors, and thus the position errors, bounded in the absence of GPS.

Similar trends are seen in the velocity errors as in the case of the position errors, which is expected. Figure 5.17 shows the RMS velocity errors computed across all outages. Since accelerations are integrated just once to obtain velocity, the velocity errors grow linearly which is apparent from the plot. The maximum RMS error seen with the 15-state filter is about 8 m/s, while with a 27-state filter these errors reduce to less than 3 m/s providing similar improvements as in the case of position results. With the HG1700 IMU, the maximum error remains within 7 cm/s for an outage duration of 30 s. These results are seen to be commensurate with previous investigations done with this IMU (e.g. Petovello 2003).

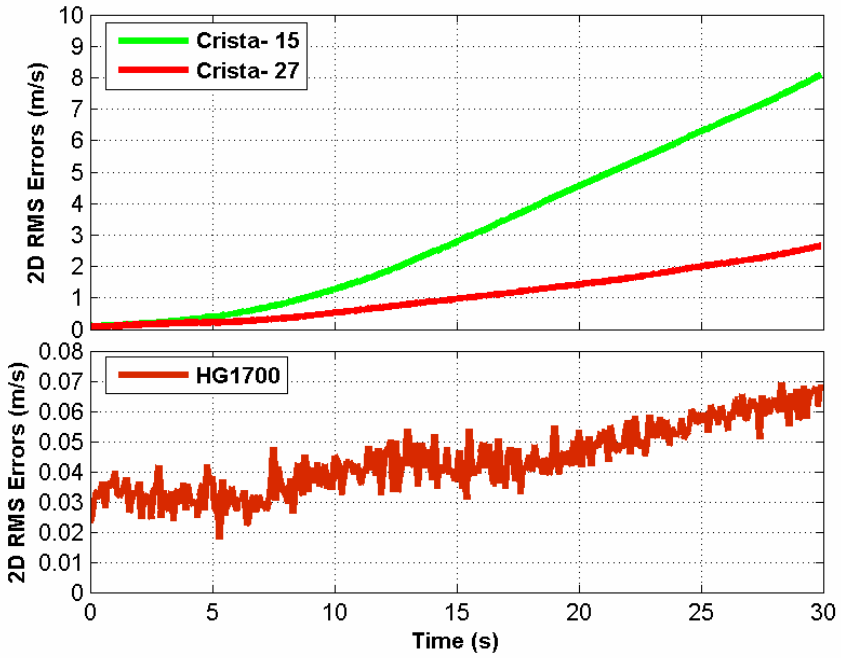

Figure 5.17: RMS Velocity Errors Across all Outages (30 s)

While the inclusion of extra error states in the integration filter of the DGPS/MEMS INS system provided significant improvements over a conventional filter, the error levels in the position and velocity solution are still high, and thus further improvements are desired. As discussed previously, one way to improve the system performance is to use vehicle motion constraints, the results of which are discussed in the following section.

5.5.2.2 Vehicle Motion Constraints

The outage conditions chosen for this analysis are identical as in the previous section (see Figure 5.13). The analysis is done with the Crista IMU only, as the error levels in the HG1700 are very small. The data is processed with both 15- and 27-state filters. First the results obtained when velocity constraints are used are presented, followed by the results obtained through height constraints.

Vehicle Velocity Constraints

Figure 5.18 shows results when comparing the horizontal position error of both filters when vehicle velocity constraints are used. The scale of Figure 5.18 is increased to match the scale of Figure 5.14 to allow for a closer analysis of the improvements when velocity constraints are used. The standard deviation of the constraint measurements was chosen to be 1.0 m/s (based on Figure 4.5).

As can be seen in Figure 5.18, the performance improved significantly when vehicle velocity constraints are used, with maximum horizontal errors limited to 8 – 50 m over different outages, with the 15-state filter. The performance of the 27-state filter is again

superior relative to the 15-state filter, with maximum errors for all the outages reduced to less than 21 m.

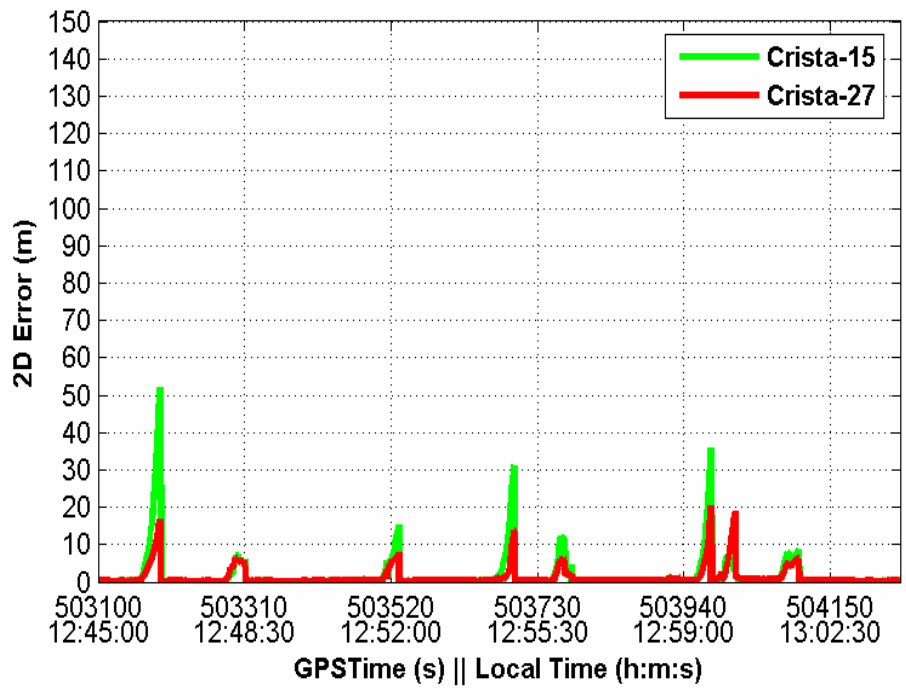

Figure 5.18: Position Errors during Individual Outages with Velocity Constraints

Figure 5.19 shows the RMS position errors computed across all outages, while Figure 5.20 shows the velocity errors. The dotted lines in the figures repeat the results seen previously with no constraints case, while the solid lines are the results with velocity constraints. As can be seen, the maximum of the RMS position errors across all the outages reduce to less than 25 m with the 15-state filter which is an improvement of about 73 % as compared to the same filter without constraints. For the 27-state filter, the maximum error is limited to 13 m, which is an improvement of 58 % compared to the 27-state filter without constraints. Similar improvements are seen in the velocity errors as well, which is now reduced to a maximum of 2.4 and 1.1 m/s with the 15- and 27-state

filters, respectively. Since the velocity error results are generally analogous to position error results, these errors will not be discussed in the further analysis.

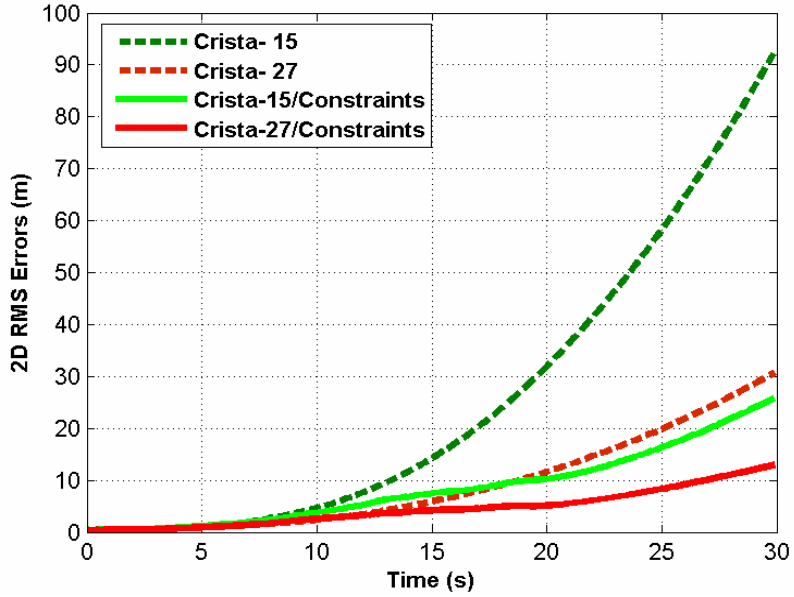

Figure 5.19: RMS Position Errors with Velocity Constraints Computed Across all Outages (30 s)

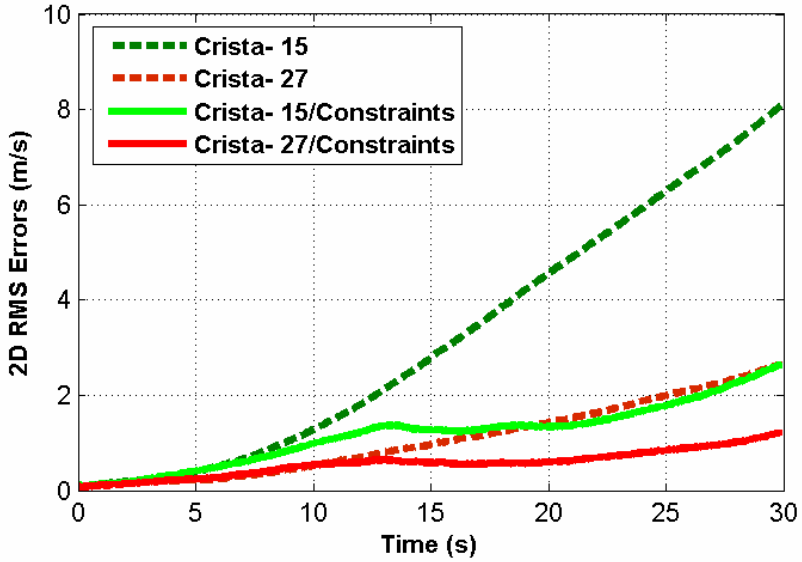

Figure 5.20: RMS Velocity Errors with Velocity Constraints Computed Across all Outages (30 s)

It is noted from Figure 5.19 and Figure 5.20, that the improvements are less at the beginning of outages (first 5-7 s). After careful investigation, it was found that the velocity measurement noise value, which was chosen to be 1.0 m/s, is the reason for the lower initial improvements. The filter predicted accuracy of the velocity remains better than that at the beginning of the outage, such that the Kalman filter does not weight the measurements as high relative to the predicted value, leading to lower improvements during this period.

Since the vehicle velocity constraint measurements are available only in the lateral and up directions, typically the vehicle's forward velocity is not observable (Sukaarieh 2000). To verify this fact, the body frame velocities are plotted in Figure 5.21. The figure shows the velocities obtained through the 27-state filter for the case when the constraints are used, and when not used.

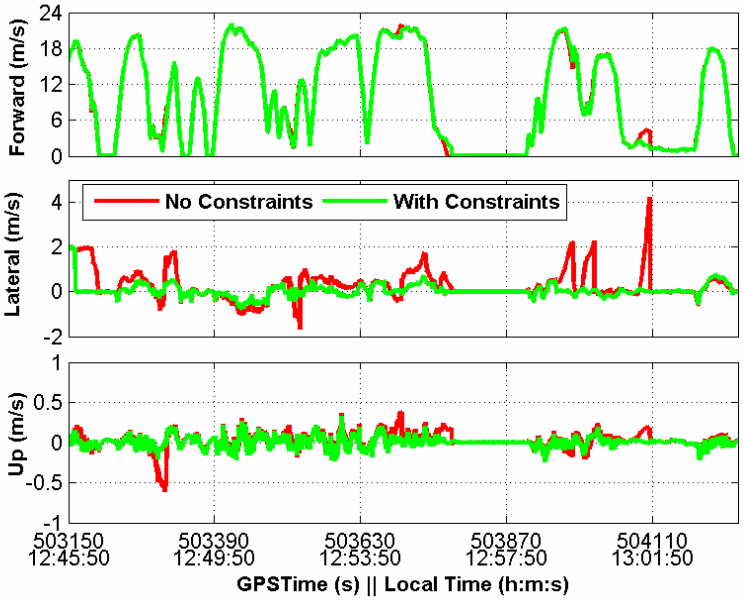

Figure 5.21: Body Frame Velocity with and without Velocity Constraints (27-state)

As can be noted, the use of velocity constraints primarily reduces the errors in the lateral and up velocities. Although small improvements in the forward direction can also be noted relative to the 'no constraints' case which is shown more explicitly in Figure 5.22. This is believed to be because of improvements in the attitude estimation, specifically the estimation of roll and pitch (tilt), which are shown in Figure 5.23. It was noted earlier in Equation (4.32) that the constraint measurements in the body frame are related to velocity errors and attitude errors. Consequently, the use of constraints helps to improve the estimation of attitude as well. Also, since a strong coupling exists between the north velocity and pitch, and east velocity and roll (El-Sheimy 2004), any improvement in velocity estimation shows in the estimation of roll and pitch. Therefore, the use of constraints provides small improvements in the forward direction as well. Further, to prevent error degradation in the forward direction an odometer is typically used alongside velocity constraints (e.g. Sukkarieh 2000 and Shin 2005)

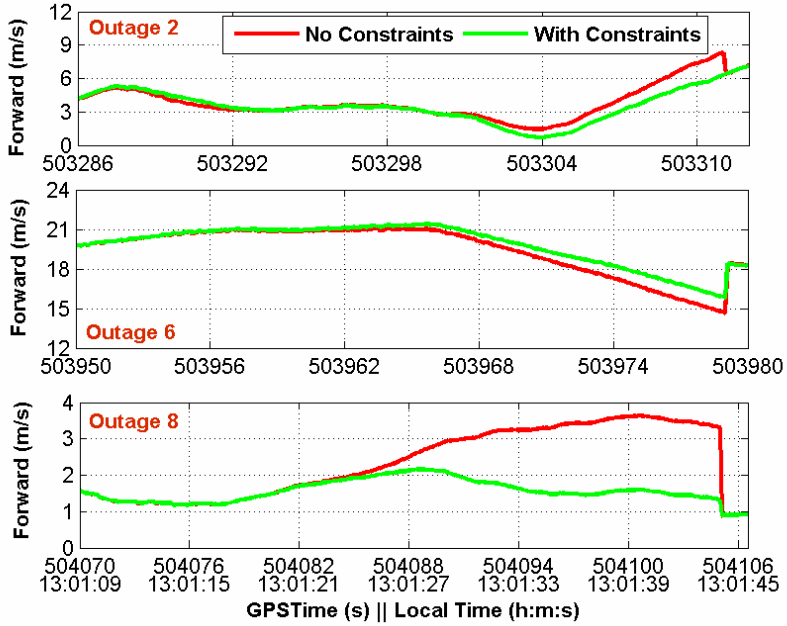

Figure 5.22: Forward Velocity over Different Outages with and without Constraints

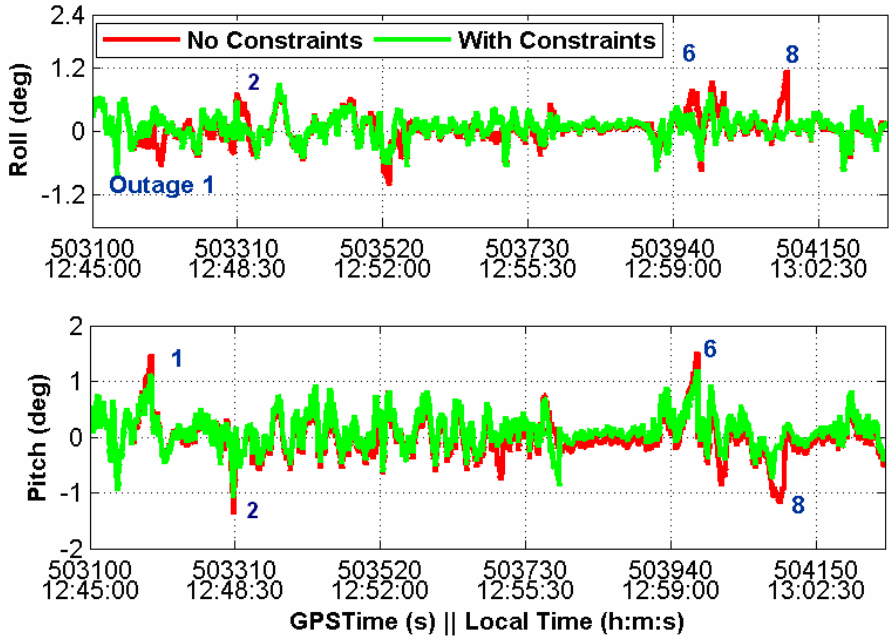

Figure 5.23: Roll and Pitch with and without Velocity Constraints (27-state)

It should be noted that which velocity component (north or east) gets an advantage from these constraints depends on the heading of the vehicle. For instance, if the vehicle is moving north, the lateral direction gets approximately aligned with east, and thus velocity errors in the east direction get constrained, consequently, it leads to more improvements in the east position accuracy relative to north.

Vehicle Height Constraints

The height constraint measurement is obtained through fixing the height to the best height solution computed before encountering the outages. Since, the outage duration is short (30 s) the variation in height is assumed to be small, and thus relatively low standard deviation of measurement is chosen, i.e. 0.5 m. Figure 5.24 shows the

horizontal RMS position errors Again, the dotted line is the case when constraints are used, while the solid line is the result with height constraints.

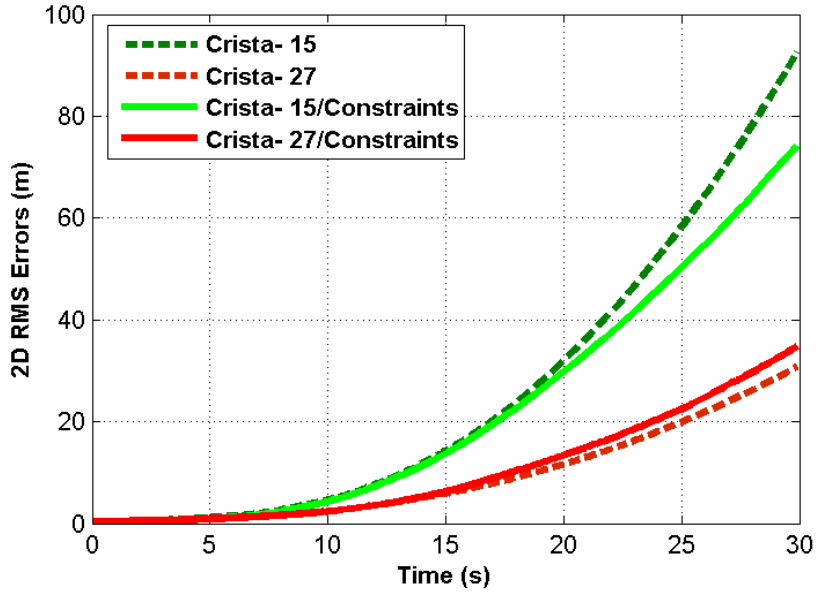

Figure 5.24: RMS Position Errors with Height Constraints Computed Across all Outages (30 s)

As can be seen, the improvements with height constraints are small with the 15-state filter. The maximum RMS errors reduce to about 74 m, which is an improvement of only 20 %. This is because the outages are complete. The height constraints are specifically useful under partial outage conditions, where it helps by directing the gain because of the presence of a few satellites in the estimation of the horizontal position and receiver clock parameter. In contrast, the performance of the 27-state filter with height constraints degraded by about 4 m (RMS value). Although not significant, the percentage degradation relative to the no constraints case is 13 %.

5.5.2.3 Performance Summary

Figure 5.25 shows the maximum position errors for each IMU and each filter with and without constraints over different outage durations. Table 5.8 summarises the maximum of the RMS position errors for each processing mode in each dimension, and Table 5.9 compares the percentage improvements in each mode compared to the basic 15-state filter.

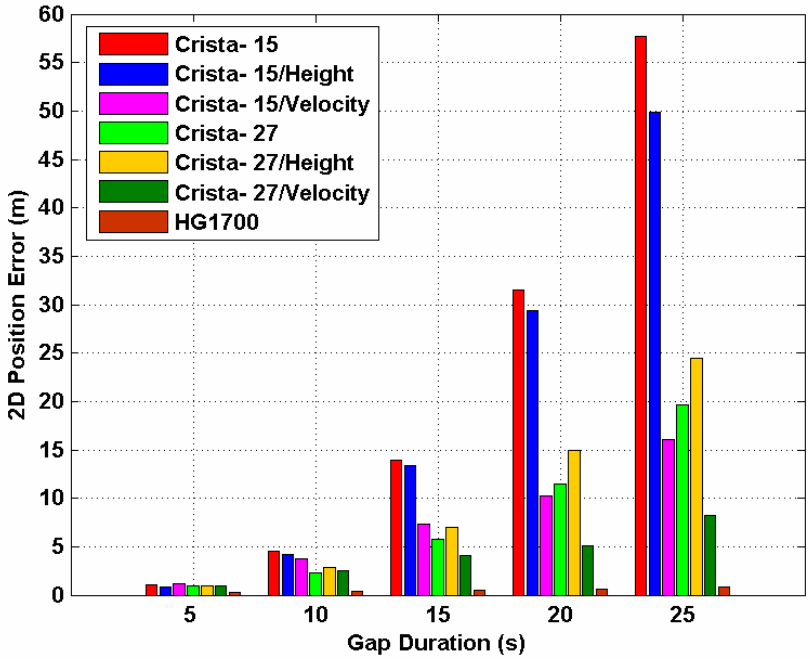

Figure 5.25: Horizontal Position Errors over Different Outage Durations

From Figure 5.25, the Crista IMU is seen to keep the maximum 2D position errors within 5 m for approximately 11 s with the basic 15-state filter, and 14 s with the 27-state filter (without constraints). Furthermore, the maximum errors remain within 10 m for about 13 and 19 s with the 15- and 27-state filters, respectively. When velocity constraints are added, the corresponding time limit increases to 20 and 28 s for the 15- and 27-state filters. From an LVNS design standpoint, a velocity constraints-aided DGPS/MEMS INS

system can sustain accuracy levels required for emergency/fleet management applications (10 m level) for approximately 20-28 s in the absence of GPS signals. It should be noted that the errors discussed here are the maximum of the RMS errors computed across all eight outages, and not the RMS errors during the outage. The average RMS errors (2D) during the 30 s outages vary from about 32 m with a 15-state filter to 4.8 m with a velocity constraints-aided 27 state filter, as listed in Table 5.10.

Table 5.8: Maximum of RMS Position Error Time Series Computed Across all Outages

30 s Gaps	*North*	*East*	*Up*	*2D*	*3D*
Position	*(m)*	*(m)*	*(m)*	*(m)*	*(m)*
Crista- 15	67.80	62.91	5.17	92.50	92.64
Crista- 15 / Height	43.22	60.10	2.94	74.03	74.09
Crista- 15 / Velocity	18.40	17.86	2.53	25.64	25.76
Crista- 27	21.83	21.57	4.33	30.69	30.99
Crista- 27 / Height	21.92	26.95	2.97	34.74	34.87
Crista- 27 / Velocity	8.22	9.958	1.40	12.91	12.99
HG1700	0.75	0.76	0.61	1.08	1.23

Table 5.9: Percentage Improvement in 2D Error in Each Processing Compared to 15-State Filter

30 s Gaps	*Crista- 15 / Height*	*Crista- 15 / Velocity*	*Crista- 27*	*Crista- 27 / Height*	*Crista- 27 / Velocity*
% (2D)	20.1	72.3	66.8	63.1	86.0

Table 5.10: RMS Position Errors during GPS Outages Averaged over all Outages

30 s Gaps	*North*	*East*	*Up*	*2D*	*3D*
Position	***(m)***	***(m)***	***(m)***	***(m)***	***(m)***
Crista- 15	21.72	23.14	2.09	31.74	31.81
Crista- 15 / Height	14.55	21.93	1.17	26.32	26.34
Crista- 15 / Velocity	5.37	5.92	1.02	7.99	8.06
Crista- 27	7.94	6.77	1.59	10.43	10.55
Crista- 27 / Height	8.12	10.51	1.14	13.28	13.33
Crista- 27 / Velocity	2.83	3.81	0.518	4.75	4.78
HG1700	0.39	0.36	0.37	0.53	0.65

5.5.3 Partial GPS Outage Simulation Results

Having quantified the stand-alone performance of the INS with and without constraints, this section now shows the ability of the MEMS and tactical grade INSs under partial GPS outage conditions. Partial outages are simulated in two ways. First, 30 s partial outages are simulated over the same periods during the trajectory as the complete outage cases (see Figure 5.13). Such outage conditions were simulated by raising the satellite elevation mask angle to 45-65˚ (over different outages), for those specific periods on the trajectory. Then further to see the upper bound of the system performance under partial outages, several satellites were rejected such that the outage remains throughout the trajectory (instead of just 30 s).

5.5.3.1 Partial Outage over 30 s Duration

Two cases are considered for this analysis. First the elevation mask angle is raised during each simulated outage such that each outage has exactly three satellites available for updating the INS. Then the mask angle is raised further to reduce the number of satellites

to two during each outage. For brevity, the Crista IMU data is processed only with 27-state filter, as the results with the 15-state filter are typically poor. A tightly coupled integration strategy is used because of its specific advantages under partial GPS availability (refer to Section 4.1). Data is processed with and without vehicle motion constraints for each case.

Figure 5.26 shows the RMS horizontal position error time series computed across all outages for each processing case, and for each IMU. The dotted line in the figure shows the results of the complete GPS outage case, to allow for direct comparison. Table 5.11 summarizes the corresponding position error statistics.

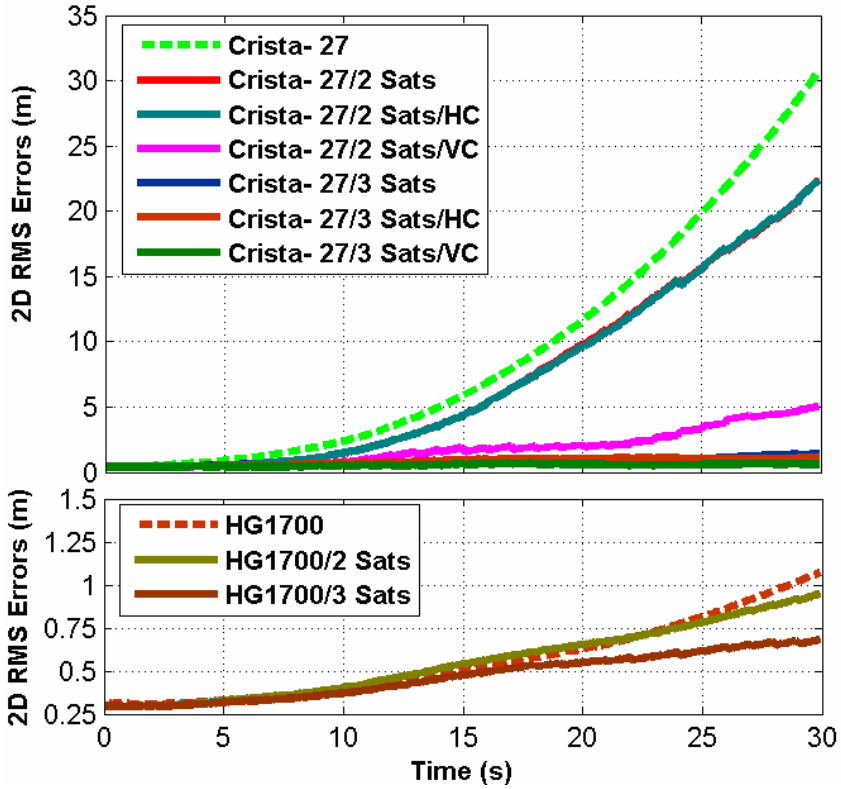

Figure 5.26: Horizontal Position Error during Partial Outages (30 s)

Table 5.11: Maximum of RMS Position Computed Across all Outages (Partial, 30 s)

30 s Gaps	*North*	*East*	*Up*	*2D*	*3D*
Position	***(m)***	***(m)***	***(m)***	***(m)***	***(m)***
Crista- 27	21.83	21.57	4.33	30.69	30.99
Crista- 27 /2 Sats.	19.17	11.54	3.72	22.37	22.68
Crista- 27 /2 Sats./ Height	18.97	11.77	2.76	22.33	22.50
Crista- 27 /2 Sats./ Velocity	4.90	1.12	1.52	5.00	5.21
Crista- 27 /3 Sats.	1.34	0.60	3.69	1.39	3.94
Crista- 27 /3 Sats./ Height	1.07	0.59	2.87	1.13	3.08
Crista- 27 /3 Sats./ Velocity	0.54	0.58	1.41	0.69	1.54
HG1700	0.75	0.76	0.61	1.08	1.23
HG1700/2 Sats.	0.78	0.53	0.54	0.95	1.09
HG1700/3 Sats.	0.42	0.54	0.49	0.68	0.84

During partial GPS outages, the performance of the inertial sensors primarily depends on the sensor error characteristics, and the geometry of the visible satellites. Due to the underdetermined estimation process, the errors in the INS do not get corrected properly and thus, accumulate. However, the rate of error accumulation is damped by the presence of a few satellites. As can be noted, the maximum errors for the MEMS INS reduce to around 22 m when updates from two satellites are available, which is better by about 27 % relative to the complete outage case. The overall influence of these partial updates on INS is seen to be small. For instance, the horizontal error stays less than 5 m for about 17 s and 10 m for about 20 s, with updates from two satellites, which is better by only 3 and 1 s relative to the full outage conditions (refer to Figure 5.25). When three satellites are available, the INS performed significantly well, such that the horizontal RMS error is limited to a maximum of 1.4 m, which is superior to the complete outage case by about

96 %. Similar trends are seen with the HG1700 IMU as well, where the errors reduce to about 95 cm (improvement of 12 %), and 68 cm (improvement of 37 %) for the two and three satellite cases, respectively.

As with the complete outage case, the use of vehicle motion constraints provided significant improvements in the performances of the MEMS INS in both the two- and three-satellite cases. When velocity constraints are added with two-satellites, the horizontal error reduces to a maximum of 5 m, which is an improvement of about 84 %. The percentage improvements are similar to the complete outage cases. However, with only height constraints the performance does not improve much, which is again a similar behaviour as the complete outage case, where the performance was seen to degrade slightly.

With three satellites plus velocity constraints, the MEMS INS provided sub-metre level accuracies. The errors are limited to a maximum of 69 cm, which is an improvement by about 50 % over the three-satellite, no constraint, case. This performance is similar to the performance of the HG1700 IMU with three-satellites (no constraints). In contrast to the two-satellite case, the use of only height constraints also improved system performance, such that the maximum error is now reduced to 1.1 m, which is an improvement of about 21 % compared to the no constraint case. The addition of height constraints with three-satellites improves redundancy, such that the three-satellite case becomes as good as the four-satellite case, thus providing more improvements relative to the two-satellite case.

The percentage improvements with height constraints in general are small relative to the case when velocity constraints are used.

5.5.3.2 Partial Outage Through Out

In this case the satellites are rejected from processing, such that only three-satellites are available throughout data processing. Data from both IMUs (Crista and HG1700) is processed, without constraints (Case I), with height constraints (Case II), with velocity constraints (Case III), and with both height and velocity constraints simultaneously (Case IV).

Figure 5.27 shows the trajectory obtained with the Crista IMU for Case I and Case IV processing, while Figure 5.28 shows the corresponding trajectory with the HG1700 IMU. Table 5.12 lists the statistical summary of the position errors for each IMU, in each case.

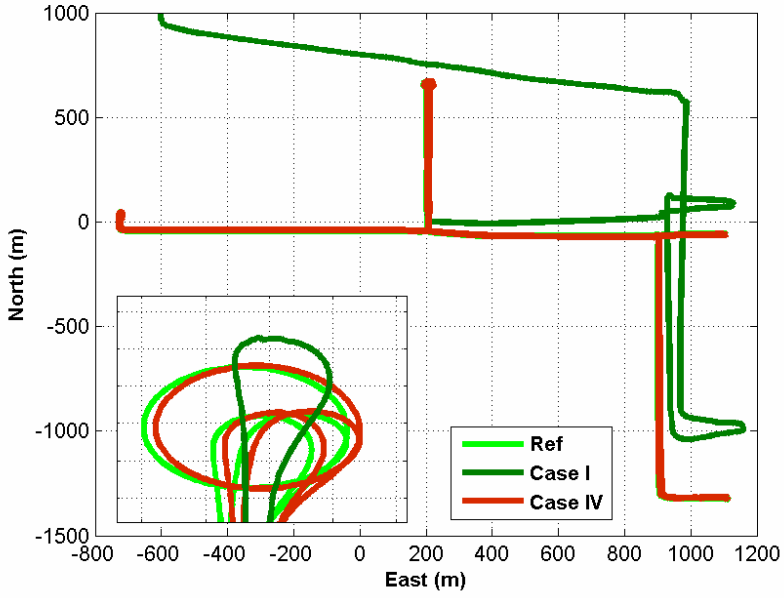

Figure 5.27: Crista IMU Trajectory under Partial GPS Outages (Three satellites, 27-state)

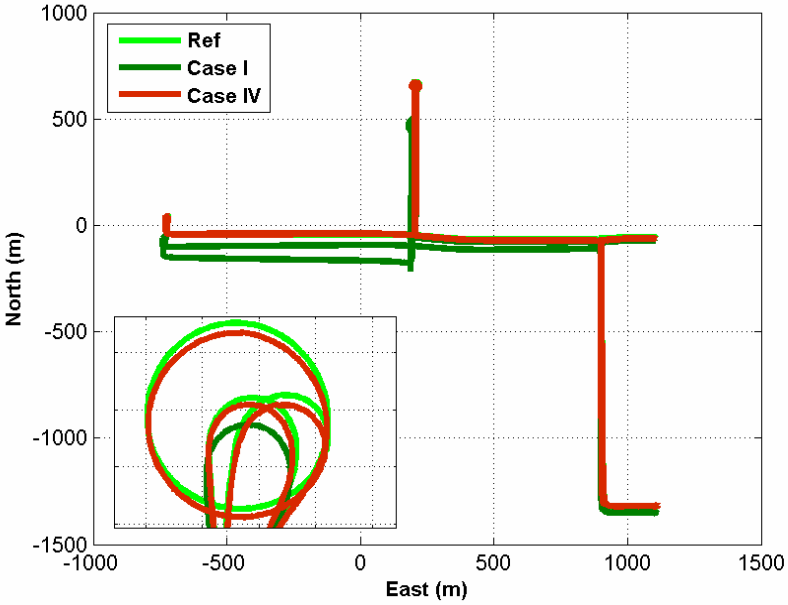

Figure 5.28: HG1700 IMU Trajectory under Partial GPS Outages (Three satellites, 15-state)

Table 5.12: RMS Position Errors during Partial GPS Outages (Three Satellites)

Position	***North***	***East***	***Up***	***2D***	***3D***
Crista -27	***(m)***	***(m)***	***(m)***	***(m)***	***(m)***
Case I	1694.9	134.71	1922.9	1700.2	2566.8
Case II	3.61	0.56	4.81	3.66	6.04
Case III	2.89	0.49	4.38	2.93	5.27
Case IV	2.79	0.48	4.29	2.83	5.14
HG1700	***(m)***	***(m)***	***(m)***	***(m)***	***(m)***
Case I	101.38	8.11	115.37	101.71	153.80
Case II	3.29	0.57	4.82	3.34	5.86
Case III	2.34	0.43	3.53	2.38	4.26
Case IV	2.31	0.42	3.48	2.35	4.22

As shown in Figure 5.27, in Case I (i.e. without constraints) with the Crista IMU, the obtained trajectory follow the reference trajectory for the first few minutes, but a continuous error accumulation leads to a divergence of trajectory. The horizontal RMS errors reach up to the kilometre level by the end of the trajectory. Although not shown explicitly, the Crista IMU is seen to keep the horizontal error below 5 m for about 52 s into the processing, while less than 10 m for about 70 s. These results are about four times better relative to the full outage case (refer to Figure 5.25). In contrast, the performance of the tactical grade IMU is significantly superior relative to the MEMS IMU, which is actually expected. The trajectory (Figure 5.28, Case I) follows the reference trajectory closely for longer periods, and diverges only at the end. The HG1700 IMU is seen to keep the horizontal error less than 5 m for about 135 s, while less than 10 m for about 200 s. The overall RMS horizontal error with the HG1700 IMU is limited to around 100 m.

The performance improved significantly when velocity/height constraints are added to the INS filter. In Case II when height constraints are added, the horizontal RMS error gets reduced to about 3.7 m for the Crista IMU, and to less than 3.5 m with the HG1700 IMU. The performance improved further when velocity constraints are used with three satellites (Case III). When both constraints are added simultaneously to the filter (i.e. Case IV), the performance improved only slightly over Case III. The horizontal RMS error in this case reduces to 2.8 m with the Crista IMU, and 2.3 m with the HG1700 IMU. These results are significant considering that the partial outage lasted throughout the trajectory, which is about 20 min. Also it can be noted from the listed statistics that,

although accuracies with the HG1700 IMU are significantly better when no constraints are used, with constraints the performance of both IMUs is similar such that the error differences are limited to less than 50 cm.

5.6 Results Summary

The results presented in this chapter compared the performance of MEMS and tactical grade IMU based GPS/INS integrated system, using a clean data set collected in an open environment. The IMUs used were the MEMS-based Crista IMU and tactical grade HG1700 IMU. DGPS updates were derived from NovAtel OEM4 receiver data. Two different integration strategies, namely the loosely and tightly coupled approaches, and two different integration filters, a basic 15-state filter and a 27-state filter, were used to investigate the performance of the MEMS IMU. The following points summarize the results found in this chapter:

1. Under good satellite coverage, the pseudorange/Doppler derived DGPS updates limited the time-dependent INS growth, such that both the INSs provided sub-metre level position accuracies (2D, RMS).
2. Both loosely coupled and tightly coupled integration strategies provided similar accuracies under full satellite coverage, with differences limited to the mm-level.
3. Under full satellite coverage, the proposed 27-state filter for the MEMS INS, improved upon the performance relative to the 15-state filter, such that the obtained trajectory became smoother and more accurate.

4. The velocity errors were analogous to the position errors, and the results followed the same trend in terms of performances of different integration strategies and different filters.
5. The attitude estimates from the MEMS INS are poor; specifically the poorly observed heading errors were large. In contrast, the attitude estimates provided by the tactical grade INS was accurate to few arc-min.
6. The use of GPS-derived heading provided significant improvements in the MEMS INS heading estimation. Improvements of up to 50-70 % were seen with different INS filters.
7. Under full GPS outage situations, the MEMS INS accumulated errors rapidly. The horizontal errors reached up to 92 m in 30 s with a 15-state filter.
8. The 27-state filter provided significant improvements in the stand-alone INS performance. The improvements seen were about 67 % during the complete outages of 30 s.
9. The MEMS INS prediction accuracies were seen to be poor primarily because of the large errors in tilt estimation during GPS outages.
10. The tactical grade INS performed significantly superior relative to the MEMS INS, where the horizontal position error remained around 1 m for the outage duration of 30 s.
11. The remedy to improve the MEMS INS performance under a full outage situation is to use vehicle motion constraints.
12. The use of vehicle height constraints under full GPS outage did not provide much improvement in the INS error estimation.

13. The use of vehicle velocity constraints provided significant improvements during periods of complete GPS outages. In the case of the MEMS INS, with a 15-state filter the horizontal error was reduced to a maximum of 25 m while with a 27-state filter it was reduced to a maximum of 13 m, for the outage duration of 30 s. The improvements were thus in the range of 73-85 % relative to the no constraint cases.
14. The INS forward velocity component (in the body frame) is not directly observable through velocity constraints. Velocity constraints were seen to aid in attitude estimation which indirectly helps to control the errors in the forward direction.
15. Under partial GPS outages, with two satellites available, the performance of the MEMS INS degraded almost as rapidly as the no satellite case. The INS errors remained within 5 m for about 17 s, which is just 3 s better than the case when no satellites were available. The overall the performance improved by about 27 % (for a partial outage duration of 30 s).
16. The use of velocity constraints with two satellites provided substantial improvements in the MEMS INS performance, such that the maximum horizontal error gets limited to 5 m, for a (partial) outage duration of 30 s. The use of height constraint had little or no effect on INS performance under this scenario (two-satellite).
17. With three satellites available, the MEMS INS kept the horizontal errors within 1.5 m for an outage duration of 30 s. When partial outages are simulated throughout the trajectory (approximately 20 minutes), the INS was seen to keep horizontal errors within 5 m for about 52 s, which is four times superior to the full outage case. The overall horizontal RMS errors reached the km-level by the end of trajectory.

18. Using three satellites and velocity constraints, the MEMS INS provided sub-metre level accuracies, for a (partial) outage duration of 30 s. Height constraints also improved performance by about 21 % relative to the no constraint case.
19. The tactical grade INS provided sub-metre level accuracies, with both the two- and three-satellite cases, for a 30 s outage duration. When a partial outage is simulated throughout the trajectory (three-satellites), the INS was seen to keep errors within 5 m for about 130 s. The overall horizontal RMS errors were limited to around 100 m, indicating considerably superior performance relative to the MEMS INS.
20. When height and velocity constraints are used (individually and simultaneously) with only three satellites throughout the trajectory, both the MEMS and tactical grade INSs provided accuracies at the few metre level. The performance of the MEMS INS was thus found to be comparable to the performance of the tactical grade INS, under such an operating scenario.
21. The use of only velocity constraints during partial outages provided a higher improvement relative to only height constraints. The use of both constraints simultaneously provided only small improvements over the case when only velocity is constrained.

CHAPTER SIX : URBAN AREA RESULTS

Having quantified the performance of the designed integrated system under benign operational conditions, this chapter is focused on a performance analysis under more realistic operational conditions, i.e. urban and semi-urban areas. The chapter begins with the urban area test description followed by the corresponding test results with the Crista and HG1700 IMUs. The results from the semi-urban tests are then presented.

6.1 Urban Area

The test set-up used for data collection was same as the one described in Section 5.1. The tests were carried out in the Calgary downtown area.

6.1.1 Test Description

Data collection began with a static initialization in a parking lot located in a relatively open area (between 3rd and 4th Avenues on 8th Street) for about 12-15 minutes. The vehicle was then driven into the core downtown area, for about 20-25 min, where the vehicle followed the trajectory shown in Figure 6.1. The total duration of the test was 35-40 min. The speed of the vehicle varied from 0-50 km/h, with frequent stops due to the traffic lights. The total distance travelled was 5-6 km. The reference station for this test was set up at the CCIT building at the University of Calgary, thus the baseline length to the reference station varied between 5 and 6 km.

The city downtown has a variety of medium (60 – 100 m) to tall (150 – 200 m) buildings, as can be seen in Figure 6.2. There were several underpasses (four between Centre Street and 4th Street, on 4th Avenue) located on the test route, which could cause severe signal

blockage. Figure 6.3 shows the number of satellites tracked by the GPS receiver at the reference station, and the corresponding satellites tracked at the rover station. A 120 s moving average of the number of satellites acquired by each receiver is also shown.

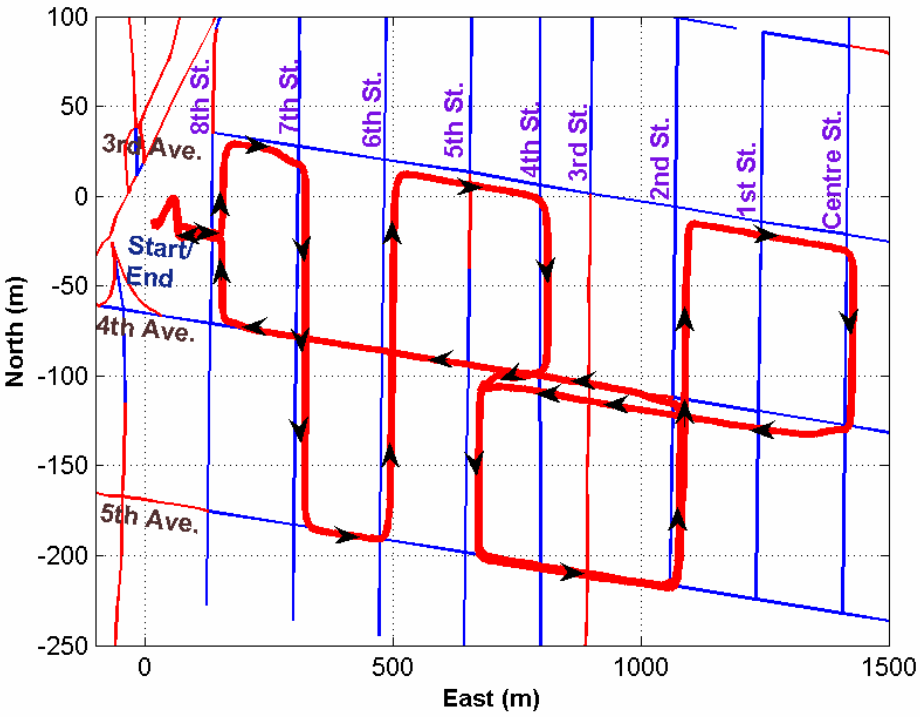

Figure 6.1: Urban Area Test Trajectory

Figure 6.2: Urban Area Testing Environment

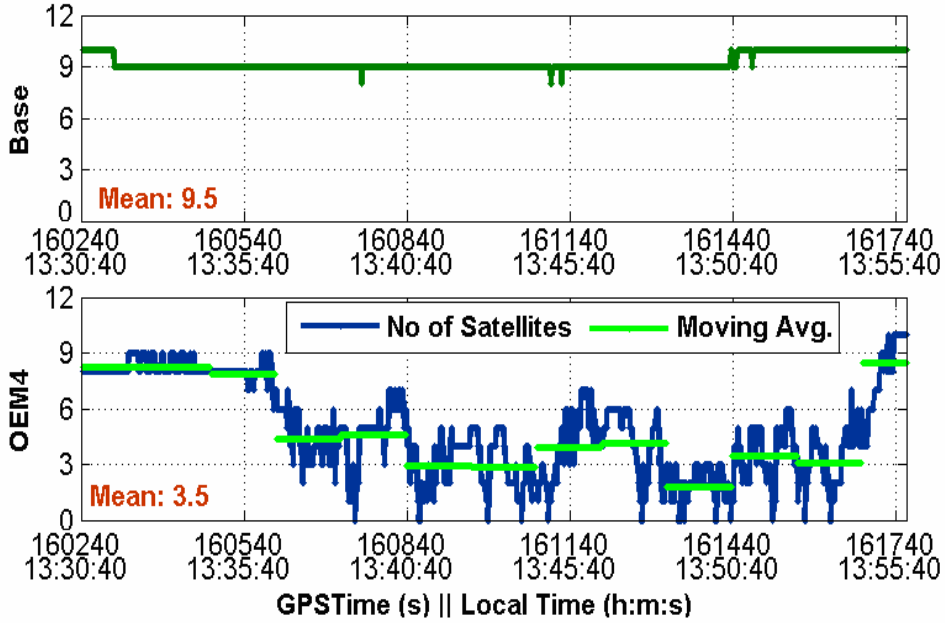

Figure 6.3: Urban Area Test: Satellites Tracked at Reference and Rover Station

As can be seen in the figure, the number of satellites at the beginning and end is around eight, as the system was initialized in a relatively open area. During the actual run in the core downtown area, the number of satellites tracked by the rover receiver varied between 0 and 7. The number of satellites was below four for about 50 % of the time, with an average value of 3.5. This satellite visibility caused poor geometry, which along with multipath errors, created a very demanding environment for GPS-based navigation.

To detect measurement outliers, the innovation-based outlier detection scheme (refer to Section 3.2) was used. Because of the statistical testing, many measurement outliers were identified and rejected during processing, so the GPS measurement availability degrades further relative to the one shown in Figure 6.3. The typical measurement availability over different portions of the trajectory is shown in Figure 6.4. For the clarity of discussion,

different regions of the trajectory are marked from A through E, where region A represents the area between 7th and 8th Streets, and 3rd and 4th Avenues. The rest of the markings follow the same rule.

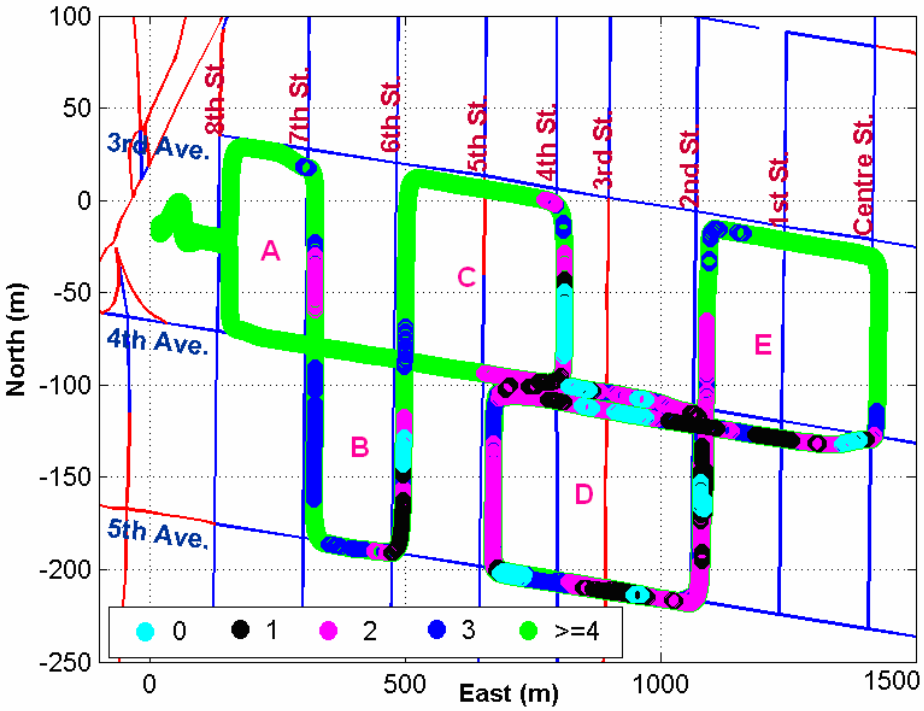

Figure 6.4: GPS Pseudorange Observation Availability over the Test Trajectory

As noted from Figure 6.4, the GPS observation availability is good at the beginning when the vehicle was moving in region A, with only moderate signal blockage encountered in the south-east corner of this region. The first complete GPS outage was encountered in region B on 6th Street and which lasted for about 9-10 s. The largest complete GPS outage was encountered in the south-east corner of region C (on 4th Street) and it had a 15 s duration. The most challenging portion of the trajectory is region D where the GPS availability is poor (less than four observations) for almost 100 % of the time. The test vehicle takes two loops in this area, one while going towards Centre Street, and another

when moving away from Centre Street. Region E features moderate GPS conditions with one complete outage in the south-east corner of a 3-5 s duration. Table 6.1 lists the observation availability statistics over the test run.

Table 6.1: GPS Observation Availability in Urban Area Test with OEM4 Receiver

Number of Obs.	*Pseudorange*	*%*	*Doppler*	*%*
0	50	4.2	50	4.2
1	91	7.6	91	7.6
2	255	21.3	237	19.7
3	210	17.5	147	12.3
4+	593	49.4	674	56.2
Total	**1199**	**100**	**1199**	**100**

The table shows that GPS observations are not available at all for about 50 epochs out of 1199 epochs, which is about 4.2 % of the total run time. Furthermore, the number of GPS observations is less than four for about 606 epochs, implying challenging GPS conditions for about 51 % of the time.

6.1.2 Reference Navigation Solution

The reference solution for this analysis is again obtained through the integration of the navigation grade CIMU with a geodetic grade OEM4 receiver. Processing was carried out with the POSPac software. The solution obtained in this way is therefore expected to be accurate to the sub-metre level (Table 6.2). The obtained trajectory was shown previously in Figure 6.1.

Table 6.2: Smoother Estimation Error (CIMU/OEM4)

Smoother Estimation Error (m)	*Max.*	*RMS*
Horizontal	0.76	0.42
Vertical	0.67	0.40

6.1.3 GPS-Only Solution

This section discusses the accuracy and availability of the GPS-only solution from the OEM4 receiver in urban canyon conditions. To facilitate this analysis, pseudorange and Doppler based GPS-only results were obtained from two sources:

- A solution was obtained using the C^{3}NAVG^2™ software, developed by the PLAN Group of the University of Calgary, which uses the least squares (LSQ) method (Petovello et al 2000). The use of an epoch-by-epoch LSQ solution is advantageous for the analysis of measurement errors as no smoothing occurs.
- The GPS-only solution was obtained through the GPS module of the developed software, which uses an Extended Kalman filter (EKF).

Figure 6.5 and Figure 6.6 show the trajectory obtained from the LSQ and EKF solutions. The trajectory is plotted on the digital map of Calgary, which is accurate to the sub-metre level. A constant separation is visible between the digital map and the computed solution, which is actually expected since the digital map lines represent the centre of the road while the vehicle typically moves in a lane. GPS results are discussed in terms of *solution availability*, which is defined as the percentage of time during which the solution is available while maintaining a Horizontal Dilution of Precision (HDOP) value below five.

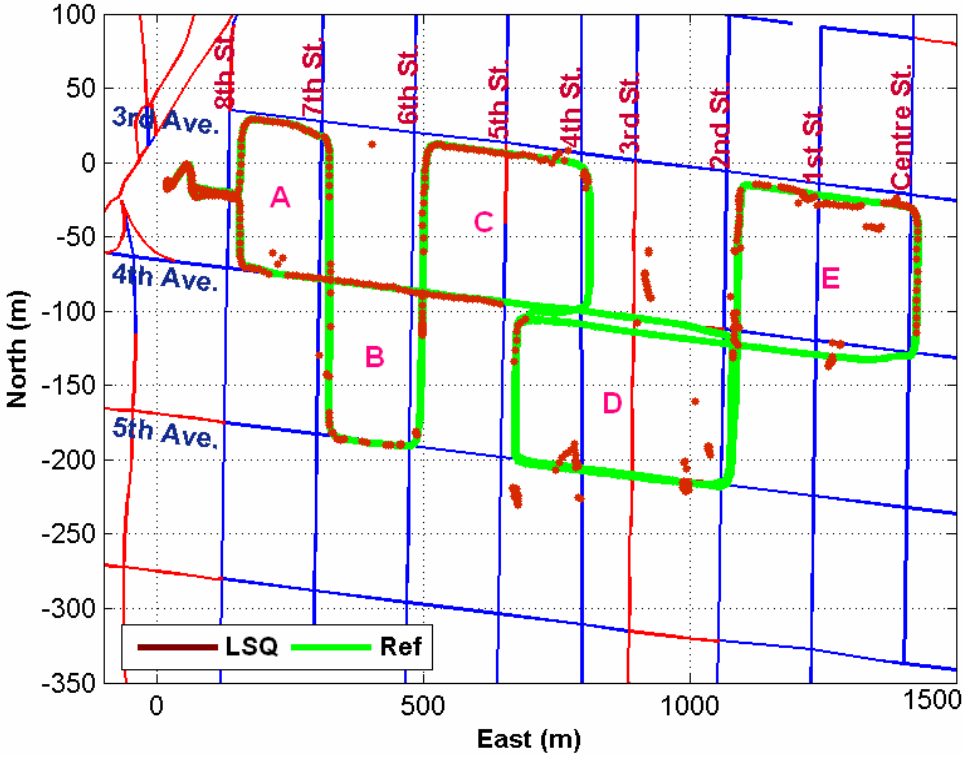

Figure 6.5: GPS-Only Solution (LSQ)

As can be noted, the solution availability is very poor, with a 47 % availability in urban canyon conditions with the LSQ approach. This is because LSQ is not able to generate a solution when the number of satellites falls below four, which is the case for about 51 % of the time (see Table 6.1 and Figure 6.4). Also, since the data was collected in urban canyons, where satellites are visible only at higher elevation angles, the HDOP values were greater than five for many epochs (see Figure 6.7), in which case the solution was discarded. The obtained trajectory agrees well with the satellite availability shown in Figure 6.4. However, it can be noted that although the availability of the solution is poor (LSQ), the solution is fairly accurate when available. This is because the OEM4 is a geodetic grade receiver which provides good quality measurements even in urban environments.

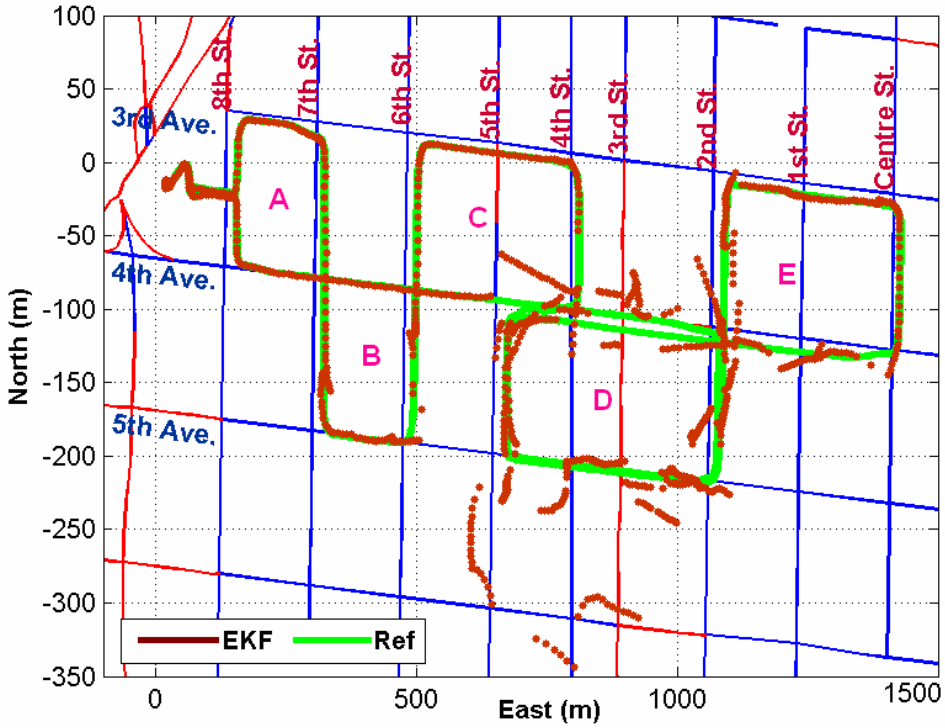

Figure 6.6: GPS-Only Solution (EKF)

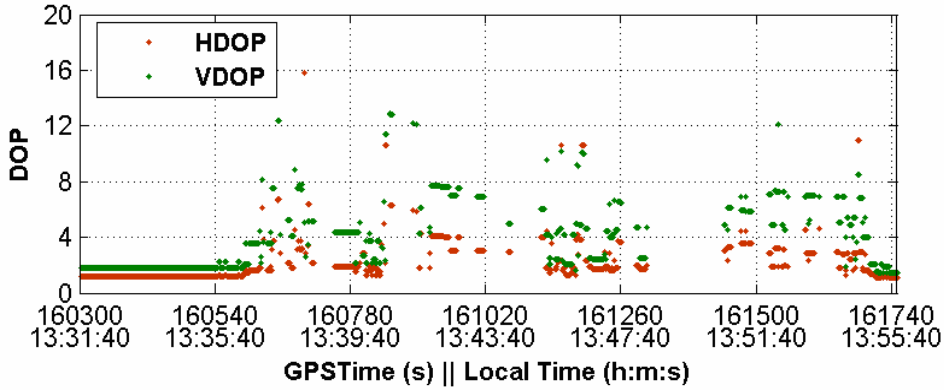

Figure 6.7: Horizontal and Vertical Dilution of Precision

The availability improves substantially when an EKF is used. The advantage of using a Kalman filter over LSQ is that the filter can predict the navigation solution based on the designed system model (Section 4.2.1) and statistics, when GPS conditions are poor. Since the solution is often predicted, drift characteristics can be noted at various points in the trajectory. The solution availabilities in regions A, B, C and E are increased, with

accuracies of better than 10 m for majority of the time; however, large drift errors can be seen in region D which is clearly the worst portion of the trajectory in terms of GPS satellite visibility. A jump in the solution can be seen in the south-west corner of region D. The reason for this jump may be multipath which is typically severe and highly variable in urban canyons. Since the satellite geometry is also degraded, it makes it harder for the reliability testing algorithm to detect these errors based on GPS-only statistics. Specifically, if GPS-only filter predicts the solution for a while, and a multipath error occurs, then it is likely that such an error will pass undetected through processing.

6.1.4 GPS/INS Integration Results

The results are divided into two sections. The first section discusses the results obtained from the designed DGPS/MEMS INS (Crista) integrated system, along with the results obtained when vehicle motion constraints are used. The second section compares the performance of the MEMS INS with the tactical grade INS (HG1700).

It is understood that when the GPS system is integrated with INS, the solution availability will be 100 % as the navigation solution is bridged by INS prediction during GPS outages. However, the *availability*, as defined in the previous section, is not the best indicator of system performance, as INS predictions may have large errors. So, a parameter termed '*Integrated System Availability (ISA)*' is defined, where the integrated solution at a particular epoch is termed available if the error in the horizontal solution at that epoch is less than a certain threshold value. Thus, based on typical accuracies expected in different land vehicle applications, three threshold values are used in this

thesis, 5, 10 and 20 m. Thus, the corresponding availability parameter is termed as *ISA-5, ISA-10,* and *ISA-20,* where an *ISA-5* of 80 % means that 80 % of the epochs have horizontal errors less than 5 m. Apart from the ISA, the maximum and RMS position errors will also be discussed.

6.1.4.1 Integration with Crista IMU

This section discusses the results obtained from the integration of the Crista IMU with the OEM4 GPS receiver data. The data is processed under four cases:

- ***Case I*** – This case represents a pure GPS/INS case with no vehicle motion constraints being used. The results obtained through both loosely coupled (Figure 4.1) and tightly coupled (Figure 4.2) integration strategies will be shown. Based on this discussion, one integration strategy will be chosen for further discussion of results in other cases.
- ***Case II*** – In this case, a vehicle height constraint is used. Height will be constrained to the best height solution computed before encountering poor GPS availability.
- ***Case III*** – In this case, vehicle velocity constraints are used. The constraints are used only during the periods of poor GPS conditions.
- ***Case IV*** – In this case, both height and velocity are constrained simultaneously during poor GPS availability.

Case I – OEM4/Crista Integration

This section discusses the results of Case I processing, i.e. the pure GPS/INS integration case. Figure 6.8 and Figure 6.9 show the trajectory obtained through tightly coupled and loosely coupled integration strategies, with the 27-state INS filter.

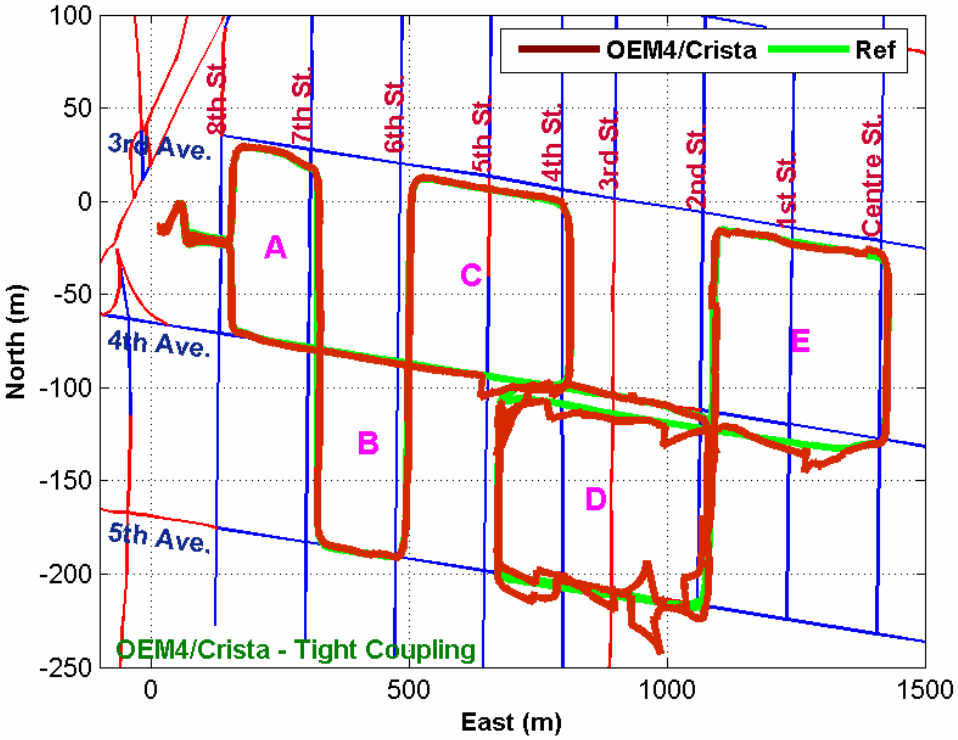

Figure 6.8: Case I – OEM4/Crista Solution – Tight coupling (27-state)

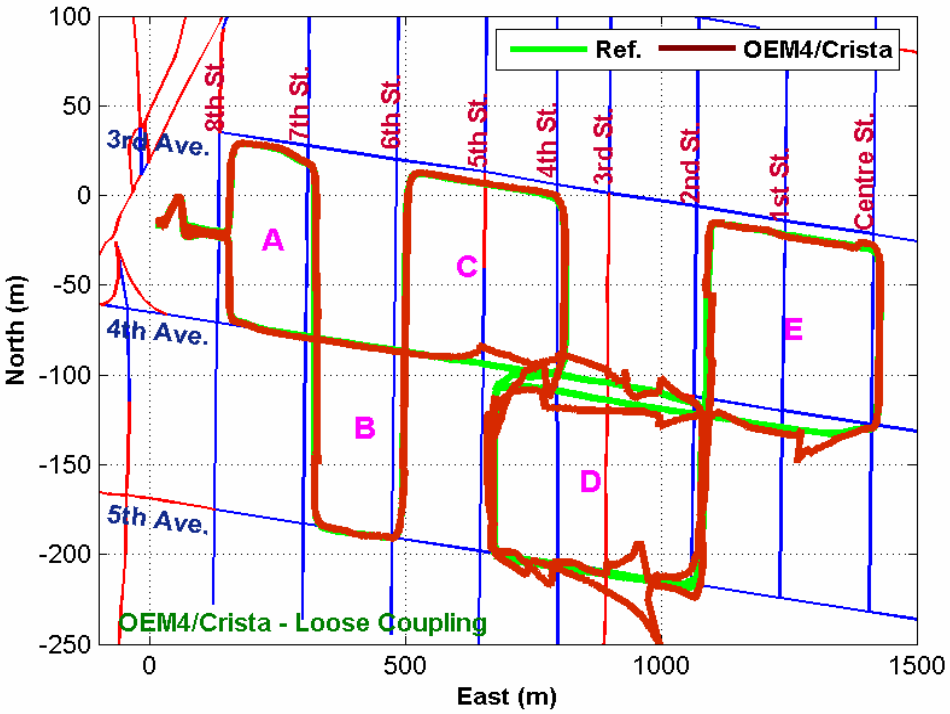

Figure 6.9: Case I – OEM4/Crista Solution – Loose coupling (27-state)

As can be noted from the figures, the Crista IMU successfully bridges the partial and complete GPS outages encountered in regions A, B and C, with both integration strategies, such that the horizontal position error remains within the 1-4 m during these portions of the trajectory. It can be noted from Figure 6.6 that the GPS-only filter is able to predict the navigation solution (during partial outages) quite accurately in these regions, by virtue of the finding that the loosely coupled integration strategy seems to be performing as good as tightly coupled integration strategy. The INS predictions are seen to bridge the biggest complete GPS outage (of 15 s) in the south-east corner of region C completely without any apparent degradation in trajectory. This performance can be attributed to superior sensor error compensation with a 27-state filter. This is evident more explicitly from Figure 6.10 which compares the performance of 15- and 27-state filter specifically in the south-east corner of region C.

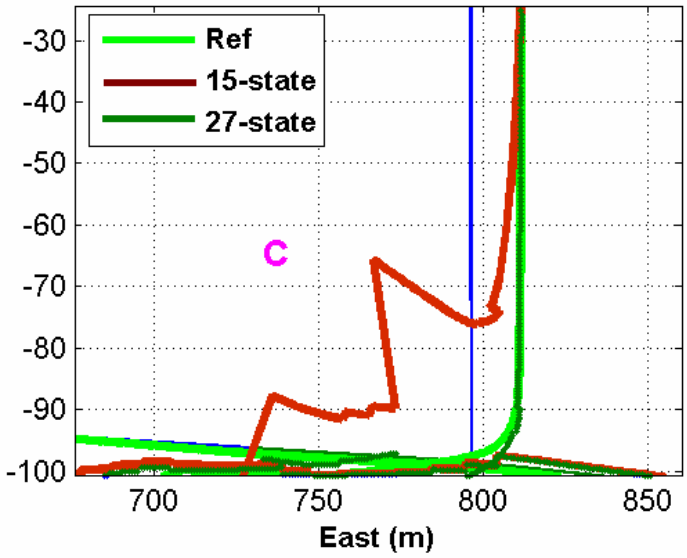

Figure 6.10: 15-state vs. 27-state: South-East Corner of Region C

Since the error levels are small initially, the obtained trajectory is stacked on top of the reference trajectory, until the vehicle entered region D. The performance of the system degrades slightly in this area. Since the GPS satellite visibility is poor, the navigation solution obtained in this region primarily depends on the INS solution, and the disagreement with the true trajectory is due to the accumulation of errors during the INS prediction process in the absence of GPS. The specific advantage of the tightly coupled integration scheme during partial GPS outages becomes evident in this region, which owing to centralized processing, is able to provide superior updates to the INS, such that the amount of error accumulation is reduced relative to loose coupling. The quality of predictions of the GPS-only filter is quite poor in this region (see Figure 6.6) which explains the poor performance of loose coupling. It should be noted that the jump visible in the south-west corner of region D in the GPS-only solution (Figure 6.6) is not visible in either of the integrated solutions (Figure 6.8 and Figure 6.9). The statistical testing within the INS filter is able to filter out the poor measurement updates more efficiently, which demonstrates the enhanced reliability of the integrated system relative to the GPS-only system.

Table 6.3 shows the maximum horizontal position error with each strategy and each filter. Table 6.4 lists the position RMS errors in each dimension for each processing mode, while Table 6.5 lists the corresponding availability statistics for the integrated system. The overall performance of the system can be considered reasonable, specifically with the tightly coupled integration scheme and the 27-state filter. As can be seen, the maximum error reached during the trajectory is about 41 m, with errors remaining less

than 20 m for the majority of time (see Table 6.5). The horizontal RMS errors seen during the trajectory is around 5.7 m.

Table 6.3: Maximum Position Errors (Case I)

Max.	***15-state LC***	***27-state LC***	***15-state TC***	***27-state TC***
2D (m)	55.99	44.80	51.68	40.62

Table 6.4: Position RMS Errors (Case I)

Position (m)	***North***	***East***	***Up***	***2D***	***3D***
15-state LC	5.84	4.47	10.61	7.35	12.91
27-state LC	5.22	4.39	7.61	6.82	10.22
15-state TC	5.14	4.14	6.45	6.60	9.23
27-state TC	4.82	2.97	6.16	5.66	8.37

Table 6.5: Integrated System Availability (%)

Processing	***ISA-5***	***ISA-10***	***ISA-20***
15-state LC	66.8	87.4	95.3
27-state LC	73.2	89.3	95.9
15-state TC	76.7	90.0	96.7
27-state TC	78.6	92.1	98.7

The results presented in this section clearly indicate that the tightly coupled integration scheme (with the 27-state filter) offers improved performance within urban canyons, over any other processing mode, and thus, will be used henceforth.

Case II – OEM4/Crista/Height Constraints

This section presents the results obtained from Case II processing. The standard deviation of the height constraint measurement was set as 0.5 m. Figure 6.11 shows the obtained trajectory.

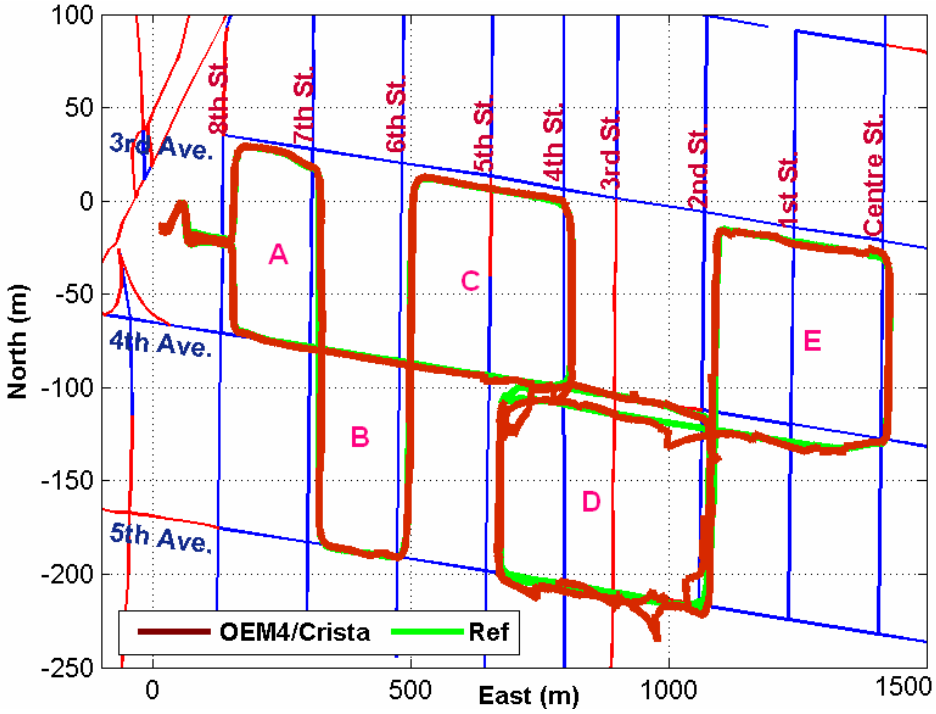

Figure 6.11: Case II – OEM4/Crista/Height Constraints

The improvements in the trajectory can be seen relative to Case I (see Figure 6.8). Specifically, the solution drifts observed in regions C and E on 4th Avenue in Case I are reduced significantly. Also, improvements can be seen along 4th and 5th Avenues in region D. The primary reason for these improvements is again improved redundancy. Since adding height provides an additional measurement, the GPS availability improves for about 17 % of the epochs (see Table 6.1) leading to improved performance. Also, since height was constrained, the accuracy of the height solution improved significantly

with errors reduced from 6.2 m to 2.6 m, which is an improvement of about 58 %. The maximum horizontal error seen over the trajectory is now reduced to less than 29 m, which is an improvement of about 29 % relative to Case I. Also, the RMS horizontal position error is reduced to 4.6 m marking an improvement of about 18 % against Case I.

Case III – OEM4/Crista/Velocity Constraints

This section presents the results when vehicle velocity constraints are added to the system. The addition of these constraints provides two additional measurements to the system, which directly aids the lateral and up INS velocities (refer to Section 5.5.2.2). Since in the absence of GPS, INS velocities are integrated to obtain a position solution, any improvement in the velocity solution ultimately leads to an improved position solution. Figure 6.12 shows the obtained trajectory.

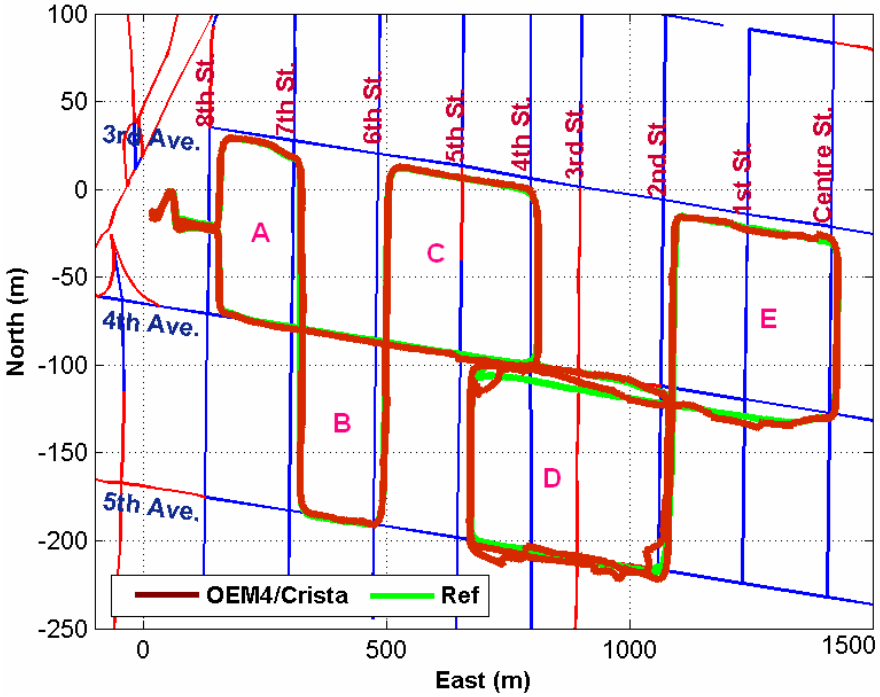

Figure 6.12: Case III – OEM4/Crista/Velocity Constraints

The trajectory improved significantly as compared to Case I, particularly in region D where the GPS availability is poor. The computed trajectory follows the reference trajectory very closely, except for a small disagreement in the north-west and south-east corners of region D. However, the extent of this disagreement is reduced relative to Case I. The maximum horizontal errors seen are now reduced to about 17 m which is an improvement of about 58 % as compared to Case I. The RMS horizontal error registered in this case is 3.7 m which is an improvement of about 35 %.

Case IV – OEM4/Crista/Height/Velocity Constraints

This section presents the results when both velocity and height constraints are added to the system. Thus, there are three additional measurements available to the system, two derived from velocity constraints and one from a height constraint. Figure 6.13 shows the obtained trajectory. Figure 6.14 compares the performances of Cases I and IV specifically in region D, and Figure 6.15 compares the corresponding horizontal position errors. Table 6.6 summarizes the position error statistics of each case considered, while Table 6.7 lists the improvements achieved relative to Case I. Table 6.8 lists the availability statistics of the integrated system.

The solution obtained in this case represents the best case solution that can be obtained from the current design of the DGPS/MEMS INS system. Improvements in this case over Case III are small (as in the case of open area analysis, see Section 5.5.3.2), so trajectory differences are not apparently visible from a comparison of Figure 6.12 and Figure 6.13. However, improvements in the position solution can be seen in Table 6.6. The horizontal

errors are now reduced to 3.4 m which is an improvement of about 40 % compared to Case I (see Table 6.7). Improvements in the vertical solution can also be seen relative to Cases I and III. These improvements seem to be low relative to that seen in open area environment during GPS gaps. However, it should be noted that complete GPS outages are of short duration over the trajectory, and mostly partial GPS outages were encountered. In addition, these improvements are computed in RMS errors over the complete trajectory and not specifically during GPS gaps (as in the case of open area analysis).

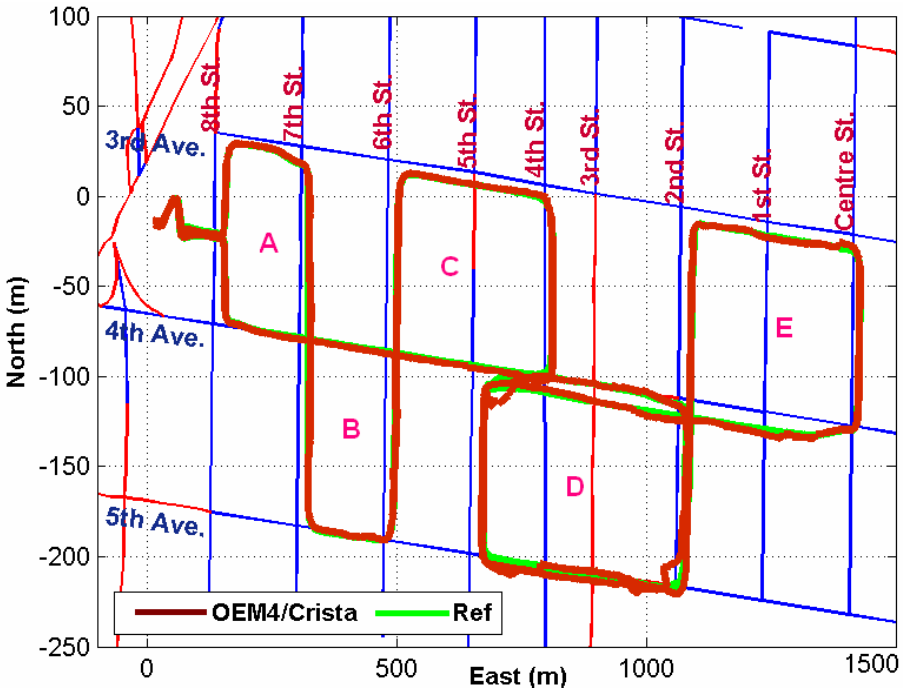

Figure 6.13: Case IV – OEM4/Crista/Height-Velocity Constraints

Figure 6.14 demonstrates the improvements that the use of constraints provided in region D. All the severe glitches are now reduced to small values through the use of constraints. The maximum error reached during the trajectory is 16 m (see Figure 6.15) with errors

remaining within 10 m for most of the time (see Table 6.8). These results are significant considering the type of inertial sensor being used, and the environment in which the testing was conducted.

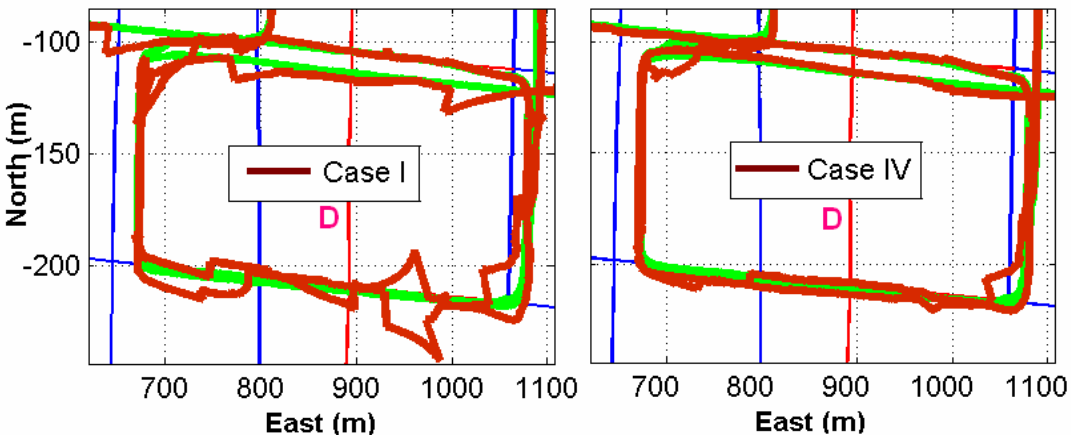

Figure 6.14: Trajectory Comparison – Case I vs. Case IV

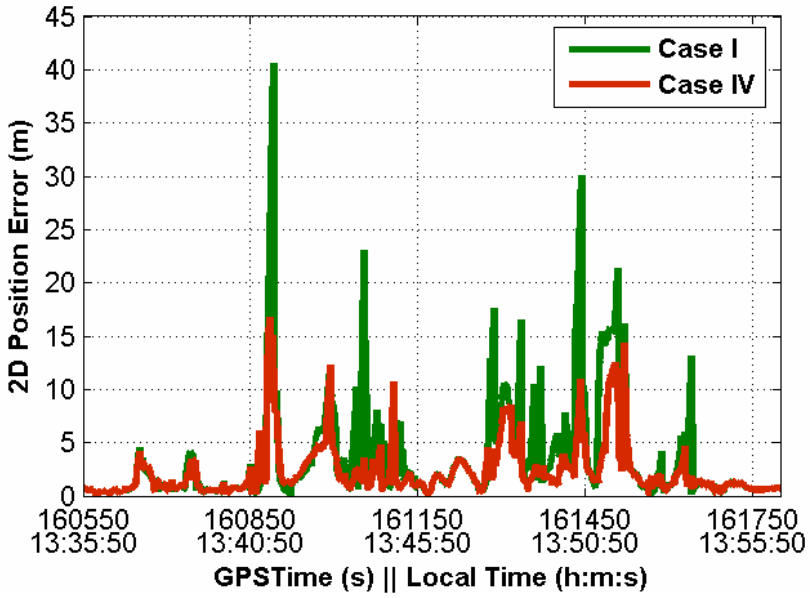

Figure 6.15: Horizontal Error – Case I vs. Case IV

Table 6.6: Position RMS Errors

Position (m)	Processing	*North*	*East*	*Up*	*2D*	*3D*
Case I	***27-state TC***	4.82	2.97	6.16	5.66	8.37
Case II	***27-state/Height TC***	3.89	2.46	2.63	4.60	5.31
Case III	***27-state/Velocity TC***	3.04	2.13	4.53	3.71	5.86
Case IV	***27-state/Velocity/Height TC***	2.70	2.01	2.67	3.37	4.29

Table 6.7: Percentage Improvements over Case I

2D	*Case II*	*Case III*	*Case IV*
%	18.7	34.6	40.46

Table 6.8: Integrated System Availability (%)

Case	*ISA-5*	*ISA-10*	*ISA-20*
I	78.6	92.1	98.7
II	87.7	95.5	99.2
III	90.4	97.0	100
IV	91.2	97.3	100

6.1.4.2 Integration with HG1700 IMU

This section discusses the results obtained through integration of the OEM4 receiver with the HG1700 IMU. The GPS data collected from antenna A4 is used, so as to keep the GPS availability conditions similar to those in Figure 6.4. This is necessary for a fair performance comparison with the MEMS IMU. For integration, the tightly coupled integration strategy is used, where the INS filter consists of only 15 states. Figure 6.16

shows the obtained trajectory, and Table 6.9 lists the corresponding position error statistics.

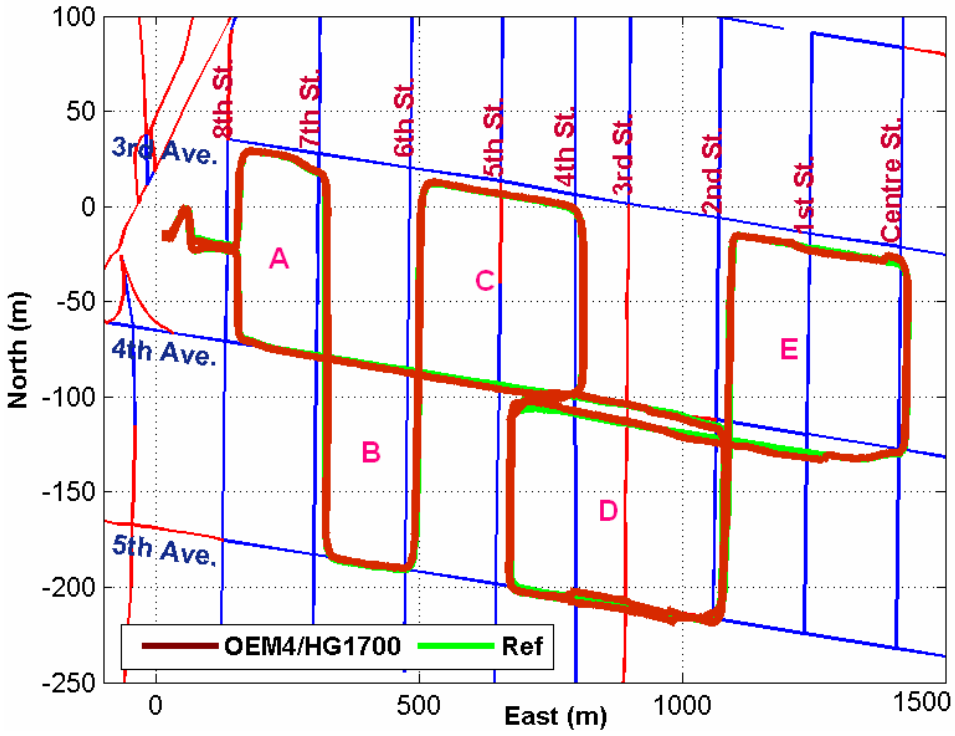

Figure 6.16: OEM4/HG1700 Solution

Through a comparison of Figure 6.8 and Figure 6.16, the superior quality of the HG1700 becomes evident. The INS bridges all the outages with superior accuracies (relative to the MEMS INS), with only a small disagreement between the reference and the computed trajectory being seen in region D (on 5th Avenue) and in region E (on 3rd and 4th Avenues). The horizontal RMS error seen with this IMU is 1.93 m. Although the performance of the tactical grade IMU is superior, the results suggest that the MEMS IMU with additional error modeling plus the vehicle motion constraints can provide accuracies comparable to what a tactical grade IMU can provide with a basic 15-state filter (Godha & Cannon 2005b).

Table 6.9: Position RMS Errors

Position (m)	*North*	*East*	*Up*	*2D*	*3D*
HG1700	1.28	1.44	3.40	1.93	3.90

6.2 Semi-Urban Area

Several tests were conducted on the University of Calgary campus of which one data-set will be used for results and analysis presented here.

6.2.1 Test Description

The university campus area features medium size buildings, which create lower masking angles. Also, the roads on the campus are narrow and are mostly covered by trees on both the sides, as shown in Figure 6.17. However, at the time of testing (in January), the foliage was absent from the trees, so masking was only moderate. These conditions are not ideal for GPS signal tracking but are also not as severe as in the case of urban canyon environments. The reference station for the test was set-up at the CCIT building.

The test began in a parking lot located on Collegiate Blvd, and then followed a trajectory as shown in Figure 6.18. The vehicle speed varied from 0- 70 km/hr, with frequent stops during traffic lights and pedestrian cross-walks. The total distance travelled was around 6-7 km, and the distance from the reference station varied between 1-4 km. Again, the distance of the vehicle from the reference station remained small thus virtually eliminating the effects of residual differential GPS errors.

Figure 6.17: Semi-Urban Test Environment

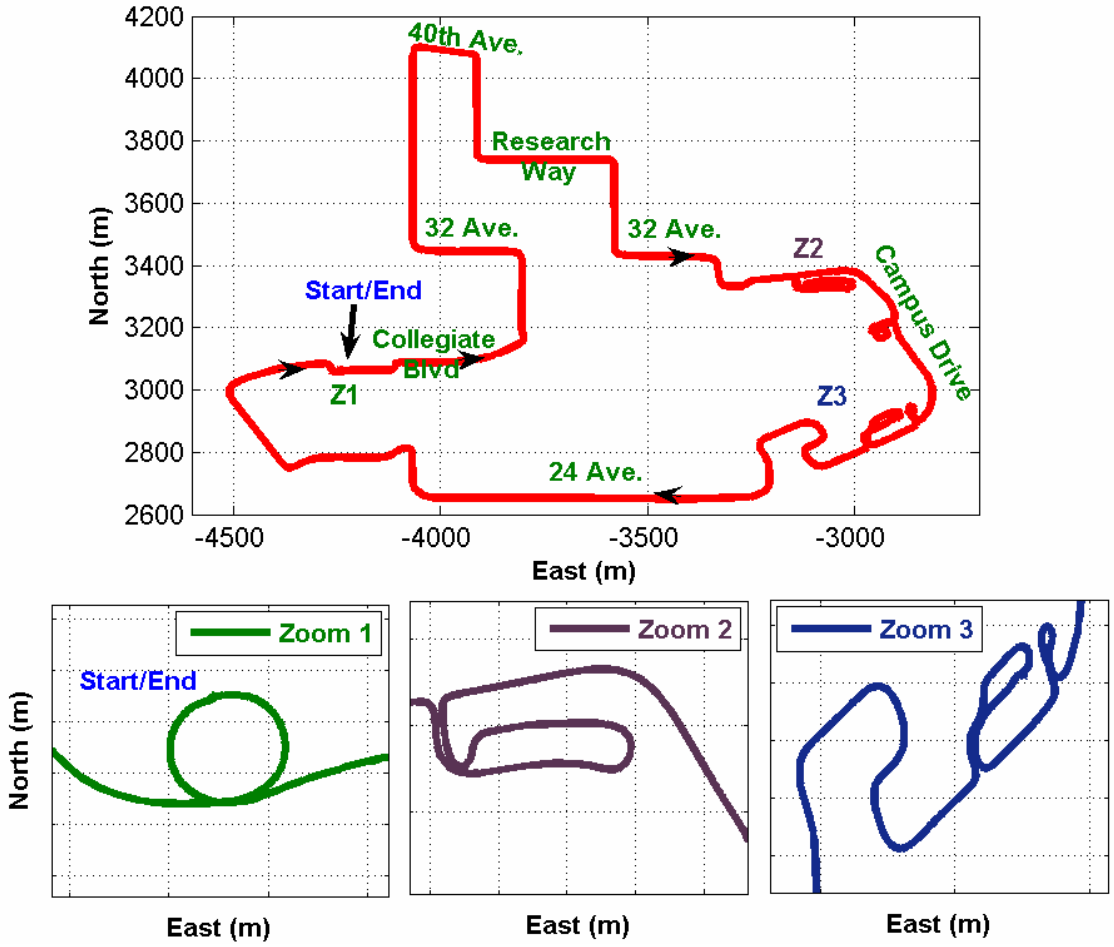

Figure 6.18: Semi-Urban Area Test Trajectory

Figure 6.19 shows the number of satellites tracked at the reference station (at CCIT) and the rover station during the test run. As can be seen, the average number of satellites visible during the test run is greater than seven. Frequent periods of partial outages (1-3 satellites) can also be seen. Overall the GPS satellite visibility is not severely poor; however, the GPS measurements are still susceptible to errors due to multipath, and thus reliability monitoring is important.

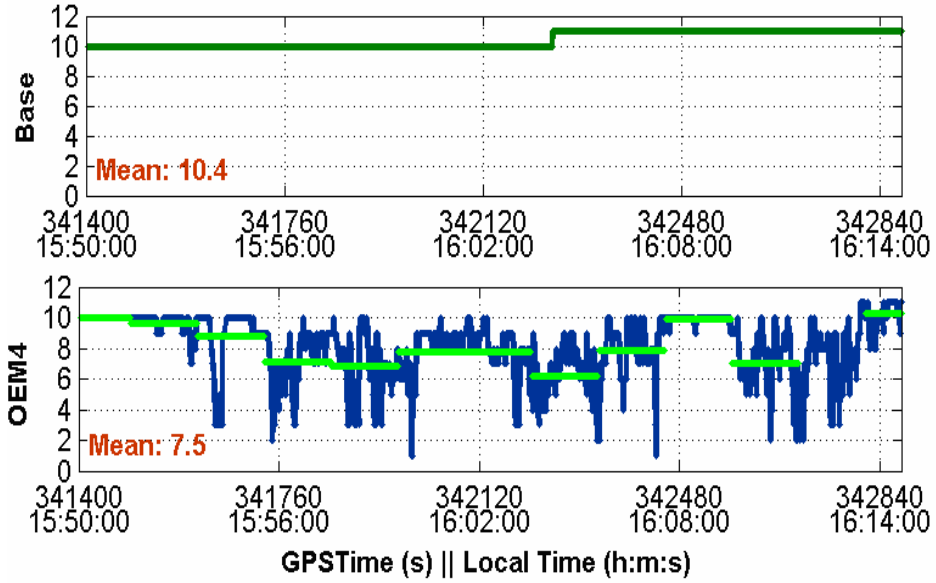

Figure 6.19: Semi-Urban Area Test: Satellites Tracked at Reference and Rover Station

Figure 6.20 shows the GPS observation available over the test trajectory, after statistical testing. In general, only short periods of partial GPS outages are seen over different portions of this trajectory. Table 6.10 lists the measurement availability statistics over the test run, and shows that the GPS availability is good for about 91 % of the time.

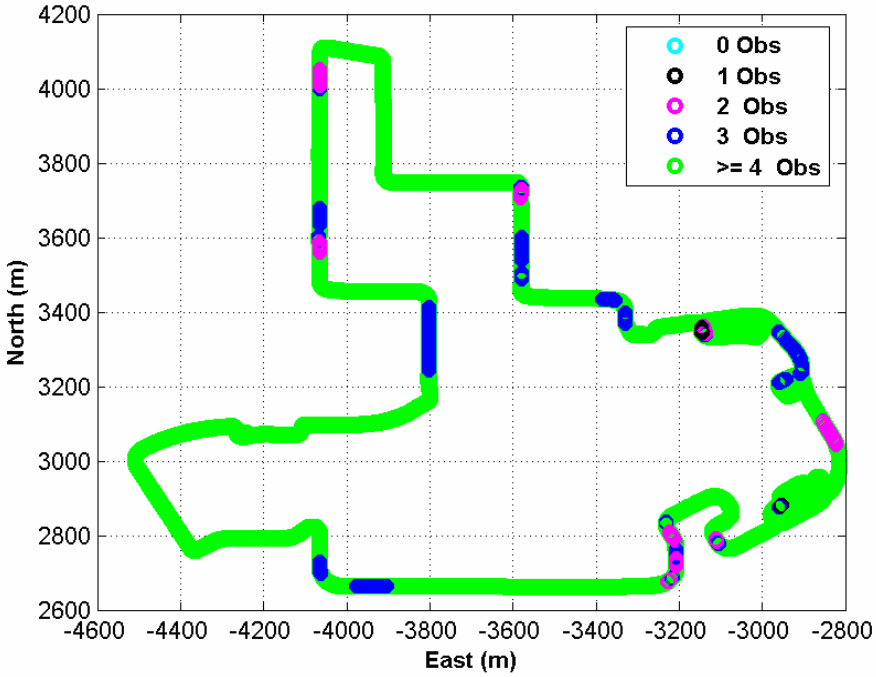

Figure 6.20: GPS Pseudorange Observation Availability over the Test Trajectory

Table 6.10: GPS Observation Availability – Semi-Urban Area

Number of Obs.	*Pseudorange*	*%*	*Doppler*	*%*
1	9	0.7	5	0.4
2	30	2.3	20	1.6
3	76	5.8	59	4.5
4+	1185	91.2	1216	93.5
Total	**1300**	**100**	**1300**	**100**

6.2.2 GPS/INS Integration Results

This section presents the results obtained through the integration of the OEM4 receiver with the Crista and HG1700 IMUs. The reference solution for this analysis is again obtained from the CIMU/OEM4 integrated system through processing with the POSPac software. The Crista IMU data is processed with the 15-state and 27-state filters, whereas

for the HG1700 a simple 15-state filter is used. Since the tightly coupled integration strategy typically provides superior results during partial outages, loosely coupled integration strategy is not considered herein.

Figure 6.21 shows the trajectory obtained from Crista IMU processing, through both the 15-state and 27-state filters. The trajectory is magnified at specific periods during partial outages to illustrate the improvements provided by the 27-state filter compared to the 15-state filter. Since only short partial outages are encountered, the 27-state filter is able to bridge them without any apparent degradation in the trajectory. In contrast, error degradation can be seen in the 15-state filter case.

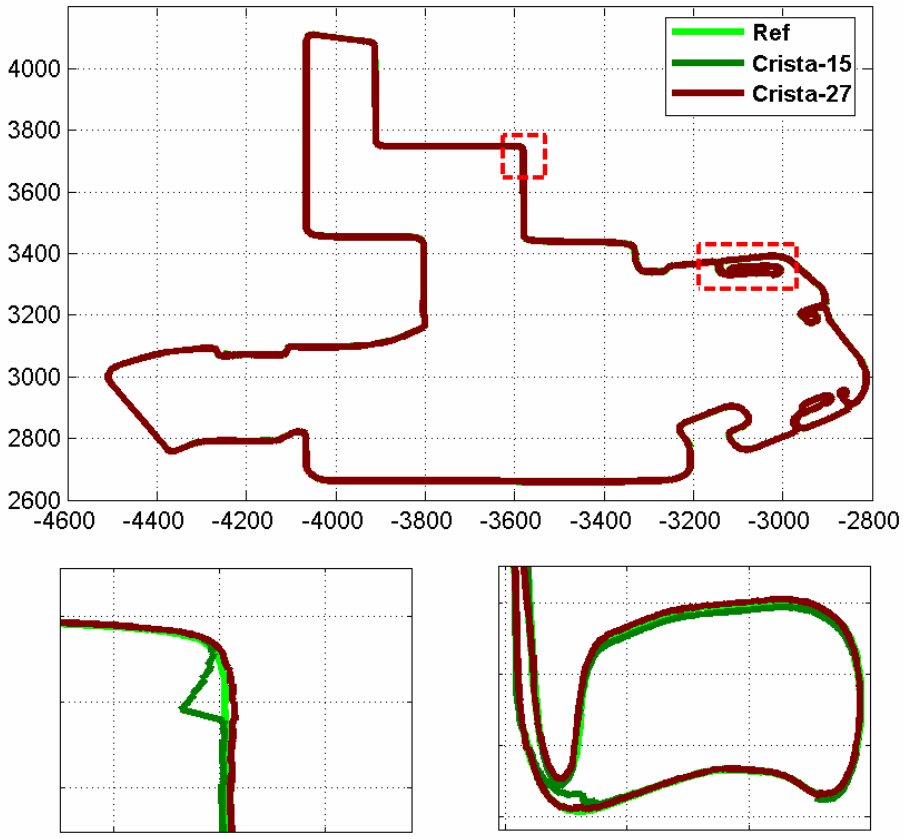

Figure 6.21: OEM4/Crista Integration: 15 State vs. 27 State

Table 6.11 lists the position RMS errors for each Crista processing mode and the errors obtained through integration with the HG1700 IMU. As can be seen, both the HG1700 and Crista IMUs provide sub-metre level accuracies. These results are only slightly degraded relative to the open area results discussed in Chapter Five (see Table 5.3). This is again because GPS is more or less available continuously which did not allow INS error accumulation. Since the integration performance is good and INS prediction error degradation is minimal with the 27-state filter (in the case of the Crista IMU), the use of vehicle motion constraints is not considered herein. Table 6.12 lists the integrated system availability.

Table 6.11: Position RMS Errors (TC)

Position (m)	*North*	*East*	*Up*	*2D*	*3D*
Crista-15	0.69	0.48	1.27	0.84	1.52
Crista-27	0.53	0.43	1.00	0.68	1.22
HG1700	0.48	0.44	0.72	0.65	0.97

Table 6.12: Integrated System Availability (%)

Processing	*ISA-5*	*ISA-10*	*ISA-20*
Crista-15	99.9	100	100
Crista-27	100	100	100
HG1700	100	100	100

6.3 Results Summary

This chapter presented the performance comparative analysis of the DGPS/MEMS INS (Crista) and the DGPS/tactical INS (HG1700) in urban and semi-urban areas. The following points summarize the results:

1. Satellite visibilities in urban canyons are typically poor. In the data set tested herein, poor GPS conditions were observed for about 51 % of the time.
2. The GPS-only system provided the navigation solution for only 47 % of the time using a least-squares estimator. The availability improved with a Kalman filter; however, since filter frequently operated in prediction mode, accuracies were seen to be poor.
3. The DGPS/MEMS INS integrated system outperformed the GPS-only system in urban canyons, in terms of accuracy, availability, and reliability. The maximum horizontal error with tightly coupled integration scheme and 27-state INS filter was around 41 m, with an RMS value of 5.7 m.
4. The 27-state INS filter (with MEMS IMU) because of better sensor error compensation did not allow rapid INS error accumulation during poor GPS conditions, and thus performed superior relative to the 15-state filter.
5. The tightly coupled integration strategy provided superior accuracies as compared to the loosely coupled integration strategy under urban areas. The accuracy of the loosely coupled integration scheme during partial outages is heavily dependent on GPS-only predictions, which typically accumulate errors rapidly, thus degrading the quality of updates available to the INS.
6. The DGPS/MEMS INS integrated system was seen to be more efficient in isolating the poor measurement updates, relative to the GPS-only system, primarily because of measurement redundancy.
7. The use of vehicle motion constraints in the urban canyon environment provided significant improvements relative to the no constraint case.

8. The use of both height and velocity constraints simultaneously reduced the maximum horizontal error to about 16 m, and the RMS errors to about 3.5 m. Thus, the performance improved by about 40 %. The horizontal error was seen to remain below 20 m throughout the trajectory when both constraints are applied simultaneously.
9. The use of only velocity constraints provided additional improvement relative to only height constraints. The use of both constraints simultaneously provided only small improvements over the case when only the velocity is constrained.
10. The DGPS/tactical INS performed significantly better relative to the DGPS/MEMS INS integrated system, such that the trajectory obtained was almost coincident with the reference trajectory. The RMS horizontal error was less than 2 m in this case, with the basic filter configuration.
11. The performance of the DGPS/MEMS INS system with extra error modeling and both constraints was found to be comparable to the performance of the DGPS/tactical INS with a basic filter configuration.
12. Under semi-urban environment conditions, both the DGPS/MEMS and DGPS/tactical INS systems provided sub-metre level accuracies. In the case of the MEMS INS, the 27-state filter outperformed the 15-state filter in semi-urban environments as well.

CHAPTER SEVEN : BACKWARD SMOOTHING

From the discussions in the previous chapters, it is clear that the use of vehicle motion constraints typically provides significant improvement in the stand-alone INS performance. The specific advantage of this approach is that it can be implemented in real time. However, if a particular land vehicle navigation application allows/requires data post-processing (such as surveying applications), a potentially more effective approach can be used for bridging GPS outages. Such an approach is based on combining the forward and backward processed data, typically termed as backward smoothing (Gelb 1974). This chapter first introduces the underlying principle in backward smoothing, and then discusses the Rauch-Tung-Streibel (RTS) smoother (Meditch 1969, Gelb 1974, Brown & Hwang 1997), which is the smoothing technique used in this work. In the end, the smoothing results in open and urban areas are discussed.

7.1 Optimal Smoothing

Smoothing is a non-real time estimation method that uses the measurement data before and after time t_k, for computing the state estimates at time t_k. An optimal smoother can, thus be thought of as a suitable combination of two optimal filters, namely the *forward filter* and the *backward filter*. The forward filter provides state estimates based on all the measurements before the current time, t_k; while, the backward filter provide state estimates based on all the measurements after time t_k (Figure 7.1).

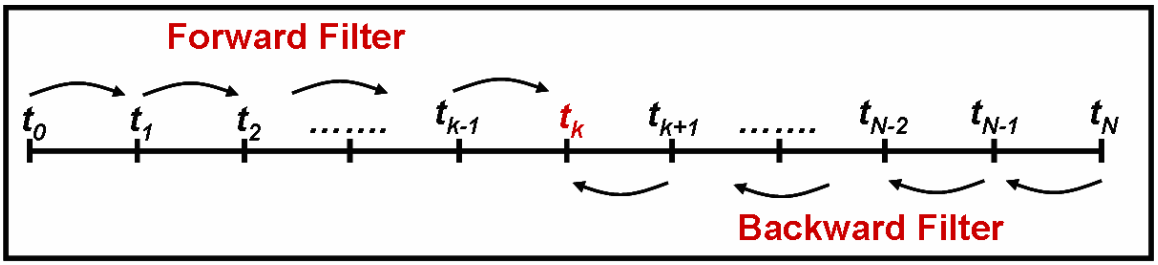

Figure 7.1: Forward and Backward Filters

Such a combination of two filter estimates can be represented by Equation (7.1) (Gelb 1974):

$$\hat{x}_k^s = A\,\hat{x}_k^f + B\,\hat{x}_k^b \tag{7.1}$$

where, the 'hat' signifies the estimated state, the superscript '*f*' represents the forward filter, '*b*' represents the backward filter, and '*s*' represents the smoother. The symbols,

x_k is the state vector at time t_k,, and

A, B are the weighing matrices.

By replacing each state estimate by its true value plus the estimation error in Equation (7.1), an equation in terms of state error vector can be derived and is given by Equation (7.2):

$$\delta\hat{x}_k^s = (A + B - I)x_k + A\,\delta\hat{x}_k^f + B\,\delta\hat{x}_k^b \tag{7.2}$$

where δ represents error perturbations. The corresponding error covariance matrix associated with Equation (7.2) is given by Equation (7.3):

$$P_k^s = A\,P_k^f\,A^T + B\,P_k^b B^T \tag{7.3}$$

where P_k is the state error covariance matrix at time t_k.

For the smoother to be unbiased, the first term in Equation (7.2) should be zero (Scherzinger 2004), as stated by Equation (7.4):

$$A + B - I = 0 \tag{7.4}$$

By minimizing the smoother error covariance, and using the relation given by Equation (7.4), the weight matrices *A* and *B* are obtained as given by Equations (7.5) and (7.6) (ibid):

$$A = P_k^b (P_k^f + P_k^b)^{-1} \tag{7.5}$$

$$B = A - I = P_k^f (P_k^f + P_k^b)^{-1} \tag{7.6}$$

Thus by substituting Equations (7.5) and (7.6) into Equation (7.3), the expression for the smoother error covariance is obtained, and is given by Equation (7.7):

$$P_k^{s^{-1}} = P_k^{f^{-1}} + P_k^{b^{-1}} \tag{7.7}$$

It is clear from Equation (7.7), that the smoother estimated error covariance is always smaller than the estimated errors of each individual filter, which is actually logical, since the smoothed estimate is obtained using a higher number of measurements. This further implies that the smoothed estimate, if not more accurate, could never be worse than the individual filter estimates (Brown & Hwang 1997). However, since the smoothing algorithm depends on the individual filtered solution; accurate filtering is a pre-requisite to accurate smoothing (Gelb 1974).

In the context of GPS/INS integrated system, smoothing is typically useful during GPS outages. The principle of smoothing during GPS outages is explained in Figure 7.2. The INS operates in a prediction mode during GPS outages (see Section 4.3.2.3). It can be seen from Equation (3.8) that when a filter operates in prediction mode, the estimation error grows since there are no measurement updates and thus the errors keep accumulating. The forward INS filter will accumulate error forward in time (brown line in Figure 7.2), while the backward filter will also accumulate error (green line in Figure 7.2), but backward in time. Thus, when the two solutions are combined using the above algorithm (Equations (7.2) through (7.7)), a smoothed estimate is obtained, which is represented by the red line in Figure 7.2. Clearly, smoothing reduces the errors significantly during the data outage interval, relative to either of the forward or backward estimate.

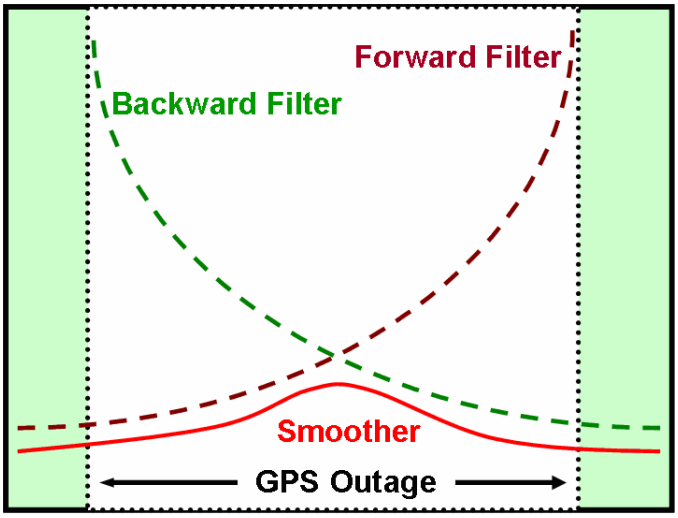

Figure 7.2: Errors during GPS Outage (adapted from Hide & Moore, 2004)

The smoothing algorithm can typically be implemented using three approaches, which give three different smoothers, namely a fixed-interval smoother, a fixed-point smoother and a fixed-lag smoother (Meditch 1969, Gelb 1974, Brown & Hwang 1997). In GPS/INS applications, a fixed-interval or a fixed-lag smoother is typically of more interest. In fixed-interval smoother, the initial and final times (t_0 and t_N) are fixed, and the estimate at epoch t_k is sought, where $t_k \in [t_0, t_N]$. This kind of smoother is used when the smoothed estimate is required for all the trajectory points in a post-mission application (Nasaar 2003). In the fixed-lag smoother, the smoothed estimate at epoch t_k is obtained, using only the measurements available between t_k and t_{k+m}, where m is a fixed number of epochs (fixed-lag) and $t_k < t_{k+m} \leq t_N$. This smoother is used when the smoothed estimates are required in *near* real-time, for instance just after a GPS outage (ibid).

In this work, the Rauch-Tung-Streibel (RTS) smoother is used, which is generically a fixed-interval smoother, but can also be used as a fixed-lag smoother (Shin & El-Sheimy 2002). Further details about RTS smoother are provided in the following section.

7.2 RTS Smoother

The RTS algorithm provides a very efficient way of implementing a smoothing algorithm (Hide & Moore 2004). The efficiency lies in the fact that the computational effort is reduced as this smoother does not require backward processing of the measurements *per se*. The smoother consists of forward processing which is a standard Kalman filter (discussed in Chapter Three), and a set of backward processing equations which propagates the saved statistics of the forward filter backward in time, to compute the

smoothed state estimates. The smoother is initialized with the forward filter's last epoch states and covariance at the end of forward processing, as stated by Equation (7.8):

$$\begin{aligned} \delta\hat{x}_{k+1}^{s} &= \delta\hat{x}_{k+1}^{f+} \\ P_{k+1}^{s} &= P_{k+1}^{f+} \end{aligned} \tag{7.8}$$

Once initialized, the smoother uses Equations (7.9) and (7.10) to provide the smoothed state estimates:

$$\delta\hat{x}_{k}^{s} = \delta\hat{x}_{k}^{f+} + G_k\left(\delta\hat{x}_{k+1}^{s} - \delta\hat{x}_{k+1}^{f-}\right) \tag{7.9}$$

$$P_{k}^{s} = P_{k}^{f+} + G_k\left(P_{k+1}^{s} - P_{k+1}^{f-}\right)G_k^{T} \tag{7.10}$$

where '+' and '-' denote the estimated and the predicted variables, and G_k is the smoothing gain at time t_k, given by Equation (7.11):

$$G_k = P_k^{f+}\Phi_{k+1,k}^{T}\left(P_{k+1}^{f-}\right)^{-1} \tag{7.11}$$

where $\Phi_{k+1,k}$ is the transition matrix from time t_k to t_{k+1}.

Equations (7.8) through (7.11) combined are referred as the backward processing equations. Since in a GPS/INS filter the state vector is actually a state error vector, the above set of equations results in a series of smoothed corrections for each epoch that should be applied to the navigation solution computed using the forward filter (Hide & Moore 2004). Ultimately, the smoothed solution is computed using Equation (7.12):

$$\hat{x}_{k}^{s} = \hat{x}_{k}^{f+} + \left(\delta\hat{x}_{k}^{s} - \delta\hat{x}_{k}^{f+}\right) \tag{7.12}$$

With each backward sweep, the forward filter estimate is updated to yield an improved smoothed estimate, which is based on all the measurement data (Brown & Hwang 1997).

From an inspection of the backward processing equations, it can be seen that state estimation is independent of covariance estimation, so it does not have to be computed in order to compute the smoothed state (Hide & Moore 2005). Also, RTS implementation requires saving of the predicted/estimated states and predicted/estimated covariance information for every epoch processed in the forward Kalman filter. This makes the RTS smoother somewhat demanding on storage space requirements. In a closed loop GPS/INS implementation, the predicted error states are always zero and the estimated states and covariance are available only when GPS updates are performed. In addition the covariance matrices are symmetric, which helps to reduce the storage space requirements. In between GPS updates, the predicted covariance is interpreted as the estimated covariance and is propagated backwards.

7.3 Results

The results are divided into two sections. The first section discusses the results obtained in an open area environment. The data set used is the same as the one described (and used) in Chapter Five. The second section discusses the corresponding results in urban canyons. The data set used for this analysis is the one described in Chapter Six. The results discussed in Chapter Five and Chapter Six, herein are referred to as the forward filter results (as in those results, backward smoothing was not used). The effectiveness of the RTS smoother in controlling the INS error degradation is quantified in terms of the

RMS position and velocity errors, and the improvements are computed relative to the forward filter results. All the results are obtained through a tightly coupled integration scheme.

7.3.1 Open Area

The open area results are divided into two sections. The first section discusses the results under complete GPS coverage. The latter section discusses the corresponding results when artificial GPS outages are simulated.

7.3.1.1 No GPS Outage Results

Figure 7.3 shows the trajectory obtained from the Crista IMU (15-state) after RTS smoothing, and Table 7.1 compiles the corresponding position/velocity error statistics computed with respect to the open area reference solution, for each IMU.

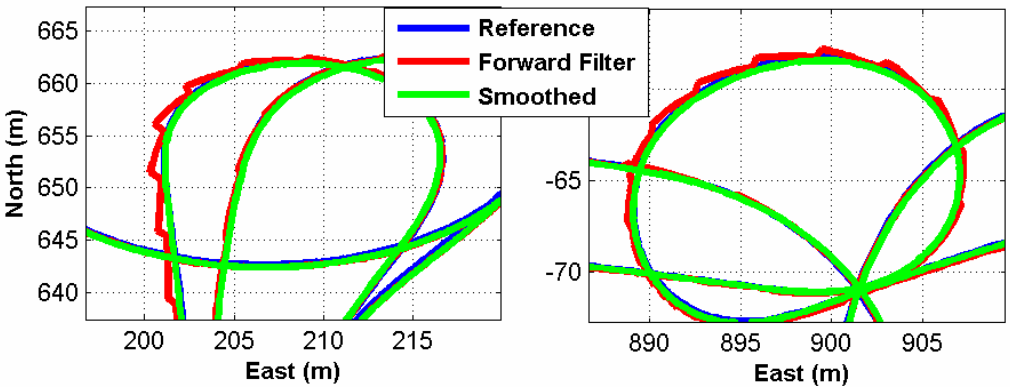

Figure 7.3: Trajectory Comparison: Forward Filter vs. Smoothed (15-state)

Under good GPS coverage, the primary advantage of the smoother generally comes into play only during INS predictions between GPS updates, the duration of which is actually limited to 1 s. Consequently, the improvements due to the smoother are expected to be

small. As noted from Figure 7.3, smoothing reduces the errors accumulated during the periods of INS prediction, leading to a smoother and even more accurate trajectory. The saw tooth behaviour seen in the forward filter solution is now reduced completely, such that the differences between the trajectories are very small, and the trajectories are nearly coincident. By comparing the results obtained during full satellite availability in Table 5.3 and Table 7.1, the above conjecture of small improvements can be verified. The Crista IMU horizontal position results improve by about 9 cm when smoothed, while the corresponding improvement in the HG1700 solution is about 15 cm.

Table 7.1: Smoothed Position and Velocity RMS Errors

	North	***East***	***Up***	***2D***	***3D***
Position	***(m)***	***(m)***	***(m)***	***(m)***	***(m)***
Crista 15	0.20	0.24	0.19	0.31	0.36
Crista 27	0.18	0.23	0.19	0.30	0.35
HG1700	0.08	0.15	0.21	0.17	0.27
Velocity	***(m/s)***	***(m/s)***	***(m/s)***	***(m/s)***	***(m/s)***
Crista 15	0.028	0.022	0.023	0.035	0.042
Crista 27	0.024	0.023	0.021	0.033	0.039
HG1700	0.009	0.009	0.016	0.013	0.021

7.3.1.2 Complete GPS Outage Simulation Results

This section discusses the smoothing results during simulated GPS outages (refer to Figure 5.13). Figure 7.4 shows the trajectory obtained with the Crista IMU (15-state), with and without smoothing. As can be noted, the errors during GPS outages reduce

significantly with smoothing, such that the smoothed trajectory follows the reference trajectory very closely.

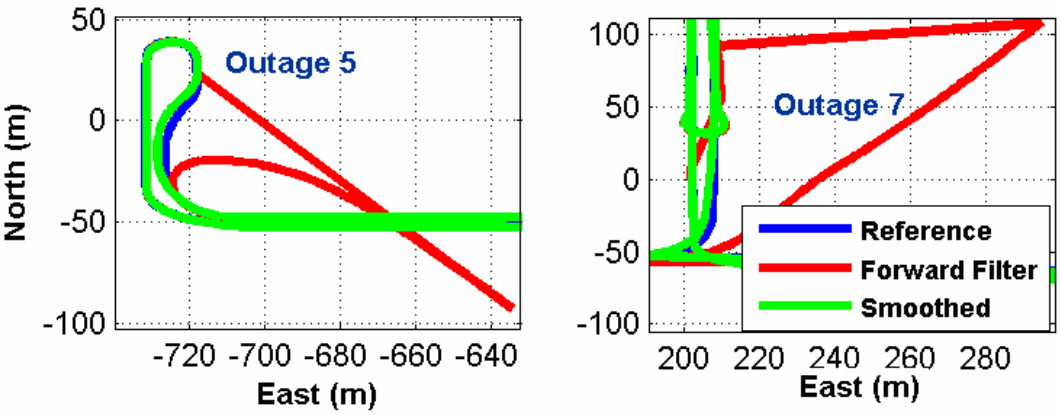

Figure 7.4: Trajectories with GPS Gaps: Forward Filter vs. Smoothed (15-state)

Figure 7.5 shows the RMS position errors computed across all the GPS outages, for each IMU, while Table 7.2 and Table 7.3 list the corresponding position RMS errors and the percentage improvements relative to the forward filter. The figures and tables show that for the HG1700, the horizontal position errors are reduced to a maximum of 25 cm, for an outage duration of 30 s. This error level is similar (in fact slightly better) to the case when no GPS gaps were simulated. The errors were thus reduced by 77 %, which compare well with previous investigations done with this IMU (e.g. Nassar 2003). In the case of the Crista IMU, the position solution improved significantly with the horizontal position errors being reduced to a maximum of 1-4 m with 27- and 15-state filters, respectively. As expected, the performance is again superior with a 27-state filter. The percentage improvement with the Crista IMU is 95 %. A hump can be noticed in the figure, which is characteristic of a smoother (refer to Figure 7.2). The results obtained with the Crista

IMU after smoothing are comparable to the results obtained with the HG1700 IMU with only forward-processing.

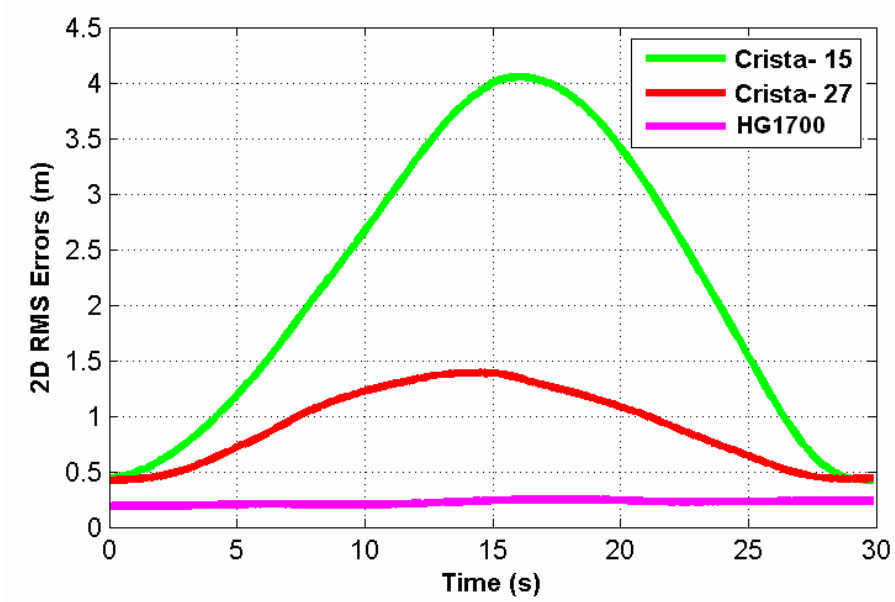

Figure 7.5: RMS Position Errors during GPS Gaps (30 s)

Table 7.2: Maximum of RMS Position Errors after Smoothing

30 s Gaps	*North*	*East*	*Up*	*2D*	*3D*
Position	*(m)*	*(m)*	*(m)*	*(m)*	*(m)*
Crista 15	1.58	3.85	2.65	4.05	4.83
Crista 27	0.82	1.13	0.76	1.39	1.57
HG1700	0.11	0.23	0.24	0.25	0.35

Table 7.3: Percentage Improvement Relative to Each Case Forward Filter

30 s Gaps	*Crista 15*	*Crista 27*	*HG1700*
2D Position (%)	95.5	95.5	77.0

7.3.2 Urban Area

The results in the previous section showed that the backward smoothing technique is an efficient way of reducing the INS accumulated error during GPS outages. This section now quantifies the smoother performance in practical situations, i.e. in urban canyons. The results are divided into two sections, discussing the results obtained through integration of the MEMS (Crista) and tactical grade (HG1700) IMUs.

7.3.2.1 Integration with Crista IMU

Figure 7.6 shows the smoothed trajectory obtained from the Crista IMU. Also shown in the figure is the trajectory obtained through forward filter processing, to allow for a direct performance comparison. For clarity, the trajectory plots with only the 27-state filter are shown; however, the error statistics of the 15-state filter are summarized at the end of this section.

As can be seen in Figure 7.6, smoothing provides a much accurate trajectory relative to forward filter. The performance improved significantly in region D which is noted as the worst portion of the trajectory in terms of GPS satellite visibility (refer to Figure 6.4). Only a small disagreement is seen in the reference and smoothed trajectories, and it is located in the south-east corner of region D. The horizontal error during the trajectory reduces to a maximum of 14 m which is an improvement of about 65 %, relative to the 27-state forward filter solution. The RMS error during the trajectory is reduced to 3.8 m, which is an improvement of about 33 % relative to the 27-state forward filter solution

(refer to Table 6.4**)** Interestingly, these improvements are slightly less than the improvements provided by the vehicle motion constraints (refer to Table 6.6).

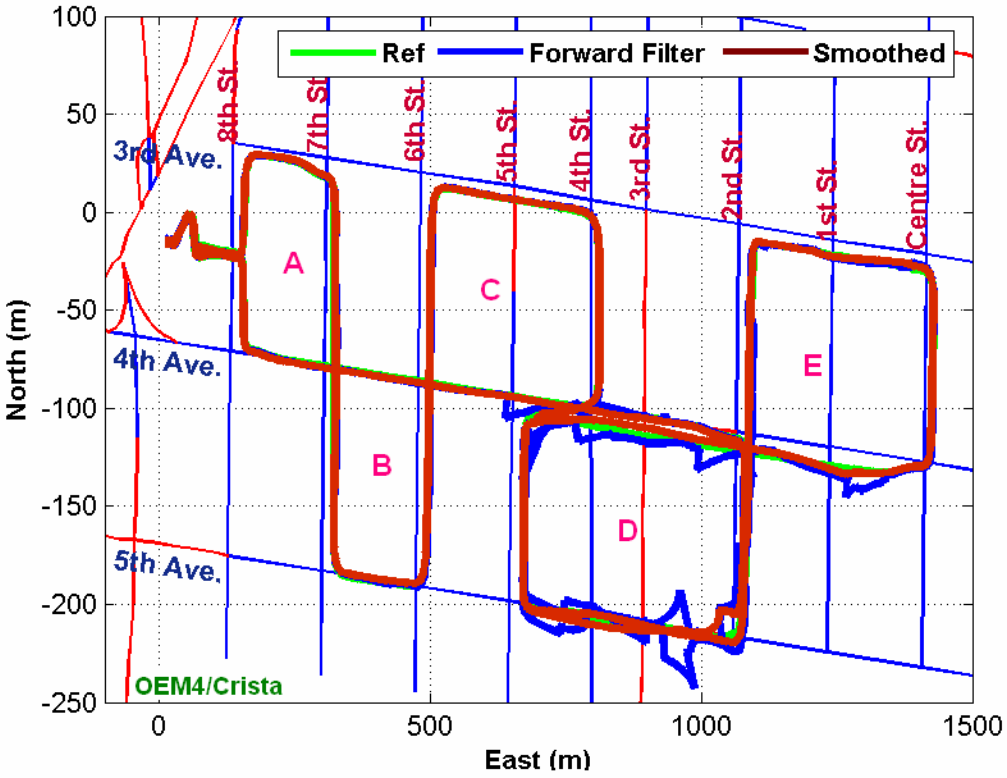

Figure 7.6: Smoothed Trajectory: OEM4/Crista (27-state)

7.3.2.2 Integration with the HG1700 IMU

Figure 7.7 shows the trajectory obtained with the HG1700 IMU. The forward filter in this case is seen to perform reasonably well (refer to Figure 6.16), such that there were only a few periods, specifically in region D on 5th Avenue and in region E on 3rd and 4th Avenues, where INS error accumulation was seen. The smoother corrected these errors, such that the smoothed trajectory is coincident with the reference trajectory. However, there is a very small disagreement in the north-east corner of region E, which is not clearly visible because of the scale of the figure, which features the maximum error seen

during the trajectory. The maximum horizontal errors seen in this case are about 6 m, and the RMS error is reduced to 1.8 m. The improvements seen are about 17 % in the maximum error and 7 % in the RMS error, relative to the forward filter results (refer to Table 6.9). These improvements are lower relative to the open area results (77 %), but it seems to be reasonable in light of the forward filter results.

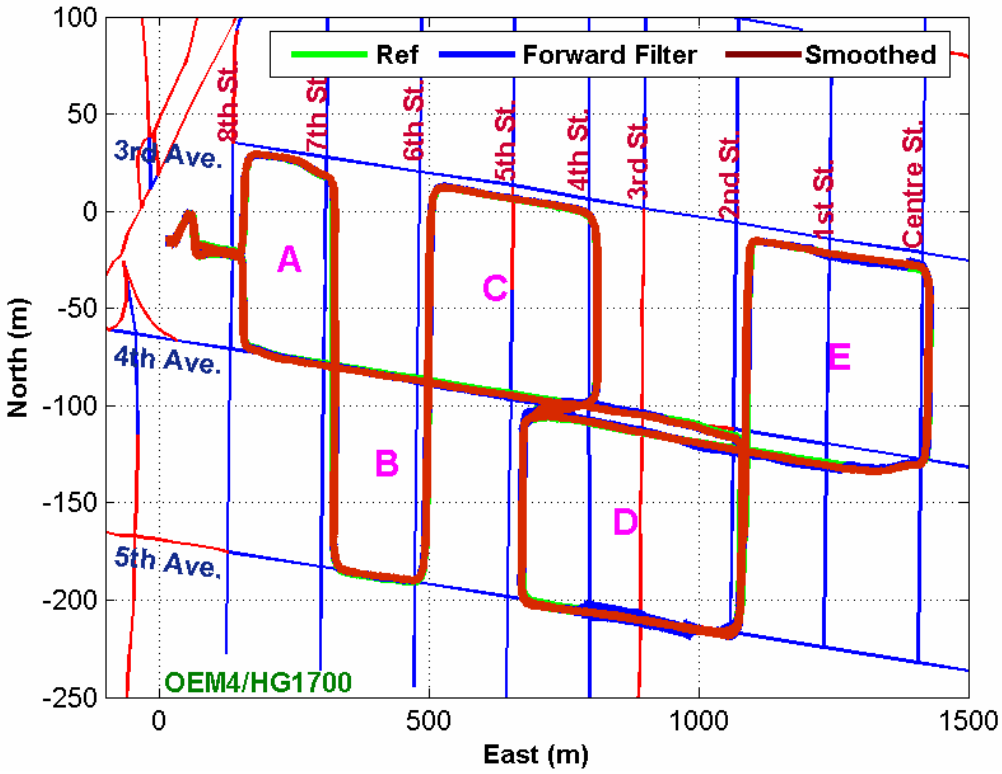

Figure 7.7: Smoothed Trajectory: OEM4/HG1700 (15-state)

Table 7.4 summarizes the error statistics discussed in the last two sections. Also shown are the statistics for the 15-state filter for the Crista IMU, to allow for a performance comparison between the two filter implementations. Table 7.8 lists the improvements achieved in each case, relative to each forward filter case.

Table 7.4: Maximum and RMS Errors in each Processing after Smoothing

***2D Position* (m)**	***Crista 15***	***Crista 27***	***HG1700***
Max.	16.90	14.15	6.08
RMS	4.10	3.78	1.80

Table 7.5: Improvements in Maximum and RMS Errors Relative to Forward Filter

***2D Position* (%)**	***Crista 15***	***Crista 27***	***HG1700***
Max.	67.3	65.2	16.9
RMS	37.9	33.2	7.0

7.3.3 Results Summary

This chapter evaluated the system performance specifically for post-mission applications, utilizing backward smoothing techniques. The following points summarize the results:

1. In an open area environment using a clean data set without any GPS gaps, the percentage improvements were small. This is because the error accumulation originally was also small. The trajectory became smoother and more accurate relative to forward filter processing.
2. The smoother reduced the MEMS INS error accumulation during GPS outages by about 95 %.
3. In the case of the tactical grade INS during GPS outages, the smoother performed as good as the no GPS outage case. The percentage improvement in this case was about 77 %.

4. Under an urban canyon environment, the smoother provided improvements of about 33 % in the case of the MEMS INS. These improvements were seen to be lower relative to the improvements provided by the vehicle motion constraints.
5. With a tactical grade INS, the original error accumulation was small in urban canyon environments, and thus so are the improvements provided by the smoother. The horizontal RMS error was seen to reduce to 1.8 m which is an improvement of about 7 % relative to the forward filter.

CHAPTER EIGHT : CONCLUSIONS AND RECCOMENDATIONS

The work presented in this thesis dealt with thorough assessment of performance of a low cost DGPS/MEMS INS integrated system for land vehicle navigation application (LVNS). The motivation behind using an integrated system for land vehicle navigation system is the fact that GPS signal does not always reach the users, and thus continuous positioning is not possible through system based only on GPS. The primary piece of equipment used was a MEMS-based Crista IMU (from Cloud Cap Technology Inc.) and a NovAtel OEM4 receiver. A tactical grade Honeywell HG1700 IMU was also used to compare the performance differences of the two IMUs, under similar operating conditions.

Both the GPS and the INS sensors are integrated together using two different integration strategies, namely loosely coupled and tightly coupled. These integration strategies were implemented using a closed loop approach. The implemented GPS-filter for loosely coupled integration strategy uses a position-velocity model, where the processing is done in a differential mode, using single-differenced technique. The designed INS-filter models the inertial navigation error states, including the position, velocity and attitude error states, using a phi-angle error model. The INS-filter was augmented by different sensor error states based on the characteristics of inertial sensor in use. Typically, for MEMS inertial sensor two INS filters were used. The first filter is a conventional 15-state filter which models nine navigation error states, and six sensor bias-drift error states. However, based on the MEMS sensor error characteristics, the 15-state filter was

augmented by additional twelve sensor error states, including six turn-on bias error states and six scale factor error states. Thus, the second filter in all includes 27 states, and was termed as 27-state filter throughout this thesis. Both the filters were used to evaluate MEMS sensor performance, to show the performance differences with each filter and the specific advantages of extra error modeling.

Different algorithms were tested to limit the MEMS INS accuracy degradation during GPS outages. The first method is based on using the vehicle motion constraints-derived virtual measurements for updating the INS filter, and is useful for implementation in real-time applications. Specifically, two constraint measurements were derived, namely the vehicle velocity constraints and the height constraints. The second algorithm used is typically useful for post-mission (or near real-time) applications, where the use of RTS smoother was evaluated. The RTS smoother provides the smoothed results based on the knowledge of all stored forward filter state estimates and covariances, and thus is an efficient way of implementing smoothing technique. The primary advantage of using these approaches to prevent error degradation in the INS is that no external auxiliary sensor is required, which keeps the system cost low.

The performance of each IMU, with each integration strategy, each INS filter, and each error compensation algorithms was evaluated in three different operating environments, namely open, semi-urban and urban areas.

8.1 Conclusions

The following conclusions can be drawn from the work presented in this thesis:

1. The DGPS/MEMS INS integrated system provided sub-metre level accuracies (38-40 cm, 2D, RMS) in open area environment, where GPS is typically available continuously with consistent accuracies. In semi-urban environment which often features partial outage conditions, the performance degraded only slightly, such that the errors remain at sub-metre level (65-70 cm, 2D, RMS). The MEMS INS was shown to bridge partial outages quite well in the semi-urban canyon environment.

2. The error in tilt estimation because of unresolved sensor error in MEMS INS is the dominant factor affecting its prediction capabilities during the GPS outages. For the outage duration of 30 s, the errors in roll and pitch were shown to grow to 3-4° level, which causes the position error expansion to 92 m in 30 s outage. This substantiates the requirement of additional aiding/special estimation techniques to keep the INS errors bounded during GPS outages.

3. Positioning accuracy during partial data outages (three-satellites) was shown to be less than 1.5 m for data outages lasting for about 30 s. When partial outages are simulated throughout the trajectory, the MEMS INS was shown to keep horizontal errors within 5 m for about 52 s.

4. Based on different tests result, modeling of the extra sensor error terms (which depends on inertial sensor error characteristics) is recommended for DGPS/MEMS

INS integrated system. The dominant error sources for the MEMS IMU tested herein were turn-on biases and scale factor errors which tend to vary from turn-on to turn-on. Modelling these errors in Kalman filter produced a 27-state filter, which was shown to improve the results substantially. During simulated GPS outages in open area environment, the 27-state filter because of superior sensor error compensation was shown to limit the errors in tilt estimation to 1˚. This ultimately provided improvements of about 67 % in position domain. The filter performed superior in urban canyons as well (which features blend of complete and partial outages.) where it was shown to provide improvements of about 15-20 %.

5. In general, velocity error trends are analogous to position error trends. Under consistent GPS availability, the errors through both loosely coupled and tightly coupled DGPS/MEMS INS system was shown to be around 15 cm/s and 9 cm/s with 15- and 27-state filter, respectively. During the complete GPS outages, the velocity errors grow rapidly to 3-8 m/s (in 30 s) with different INS filter. Primary reason for these errors is shown to be the errors in tilt estimation, which projects the gravity signal in horizontal directions.

6. The attitude error estimates from a DGPS/MEMS INS system is typically poor, specifically the heading estimates. Additional heading update, through the explicit use of GPS-derived heading information is an efficient way of limiting the INS heading error growth. The GPS heading was seen to limit the error growth by about 50-70 % using different INS filters.

7. GPS satellite visibility in urban canyons is typically poor. In the data set used herein, poor GPS conditions were observed for about 51 % of the time. With least-square estimator the GPS solution availability was shown to be only 47 %. The use of Kalman filter typically increases the availability; however, large prediction errors were noticed. The system was also shown to be inadequate in isolating and rejecting the measurement outliers. This confirms that the GPS-only system under degraded signal environment is inadequate to fulfill LVNS requirements.

8. The DGPS/MEMS INS system with tightly coupled integration scheme and 27-state INS filter performed reasonably well within the urban canyons. The horizontal RMS errors were shown to be around 5.7 m over the trajectory, with a maximum value of 41 m.

9. The DGPS/MEMS INS integrated system was shown to be more efficient in isolating and rejecting the poor measurement updates, relative to GPS-only system, in urban canyon conditions. This is because redundant information from two different sensors is combined to test the presence of outliers.

10. The type of integration strategy to be used depends on the operational environments of the system. For instance, both loosely coupled and tightly coupled integration strategy is shown to provide similar accuracies under full satellite visibility, in open area environment. Under such conditions, a loosely coupled integration strategy is preferred due to its ease for implementation. In contrast, the tightly coupled

integration scheme is shown to perform superior relative to loosely coupled case, in urban canyon conditions, which frequently features the periods of complete and partial GPS availability. During partial outages, the performance of loosely coupled integration scheme was shown to be heavily dependent on GPS-filter prediction capabilities, which are typically poor. Specifically, the improvements of over 1 m (15 %) were observed with tight coupling in urban canyons.

11. The use of vehicle height constraint provides only small improvements during complete GPS outages. For instance, during complete GPS outages simulated in an open area environment the height constraint was shown to provide improvements by about 20 % with 15-state filter, and was also shown to degrade the results a little with 27-state filter. Even with two-satellites, the height constraint was shown to have no effect on accuracies of horizontal solution. However, during the case when three satellites were available, the height constraint was shown to provide substantial improvements in the estimation of horizontal position. The percentage improvement in urban canyon environment during partial outages was shown to be about 19 %.

12. Constraining the vehicle velocity during complete and partial GPS outages controls the time-dependent INS error growth significantly. During the complete outages, and partial outages (two-satellites) simulated in open area environment, the amount of improvements were shown to be about 73-85 % with different INS filters. In urban canyon environment, which features the blend of complete and partial GPS outages, the improvements were shown to be about 35 %. The integrated system availability

with these constraints in urban canyons is shown to be 100 %, such that the horizontal position errors remain less than 20 m (ISA-20), throughout the trajectory.

13. The vehicle velocity constraints typically aids in the estimation of the lateral and up INS velocities, while the forward velocity component remains unobservable through these measurements. The constraints, however, were shown to improve the attitude estimation, which indirectly aids the INS forward velocity component.

14. In general, the velocity constraints provide more improvement relative to the height constraints. The use of both the height and velocity constraints simultaneously, typically provides only a small improvement over the case when only velocity constraints are used.

15. Backward smoothing technique is an efficient way of limiting the INS error growth to acceptable levels, but is applicable only for near real-time or post-mission applications. The percentage improvement in the MEMS INS performance during the complete GPS outages (simulated in open area environment) was shown to be about 95 %. In urban canyon conditions the percentage improvement was limited to 33-38 %.

16. The tactical grade IMU performs significantly superior relative to MEMS IMU. The INS based on tactical grade IMU is seen to outperform the MEMS INS in every operating environment and under each processing scenario. Although performance

trends of different integration strategy is shown to be similar to MEMS INS. Under some specific situations, the performance of MEMS INS is seen to be comparable to tactical grade INS, which are outlined as under:

a. Under full satellite visibility, in open area and somewhat in semi-urban area the performance differences between two systems are seen to be within few cm.

b. The performance of tactical grade INS when vehicle motions constraints are used during partial GPS outages (three satellites) is shown to be similar to the performance of MEMS INS, such that the differences remains within 50 cm.

c. The performance of DGPS/MEMS INS integrated system with extra error modeling and vehicle motion constraints in urban canyons is found to be degraded only by few metres relative to DGPS/tactical grade INS with a basic filter configuration.

d. The performance of MEMS INS with backward smoothing during complete GPS outages is seen to be comparable to performance of tactical grade INS with forward filter only.

17. The ultimate conclusion of this work is that the DGPS/MEMS INS integrated system performs reasonably well in different operating environment and typically

outperforms the GPS-only system in terms of navigation solution accuracy, availability and reliability. At times, the performance of DGPS/MEMS INS system is shown to be comparable to performance of DGPS/tactical INS. The results presented in this work strongly indicate the potential of MEMS INS for use in land vehicle applications such as emergency applications, in-car navigation applications, fleet management system, and other LBS applications.

8.2 Recommendations

The following recommendations can be made for future investigation with MEMS inertial sensors:

1. The vehicle velocity constraints are shown to provide only small improvements in the INS forward velocity component. Thus, the investigation of the system performance through the addition of an odometer which can aid in forward velocity estimation is warranted.

2. While deriving the measurement model for vehicle velocity constraints, it was assumed that the vehicle frame is aligned with the IMU frame. Further enhancements, therefore, may involve modeling the misalignments between the vehicle frame and the IMU body frame in the Kalman filter.

3. The MEMS INS performance can be improved further through the map-matching techniques. Such techniques provide additional map-derived motion constraints, and thus can potentially help to keep the INS error bounded in the absence of GPS.

4. For modeling the sensor residual biases, a Gauss Markov model was used. Further investigations may involve using AR modeling methods.

5. The integrated system used in this work typically used an extended Kalman filter for integration. Therefore, the investigation of the system performance through the adaptive Kalman filtering methods is warranted.

6. Investigate MEMS INS performance in GPS single point positioning mode. This would provide simplicity in systems integration and also reduce the overall cost of the system.

7. Further, it is recommended to test the benefits of tested algorithms with more data sets, particularly in urban areas, to represent broader range of vehicle dynamics and satellite geometries.

REFERENCES

Abdel-Hamid, W., A. Osman, A. Noureldin, and N. El-Sheimy (2004) "Improving the Performance of MEMS-based Inertial Sensors by Removing Short-Term Errors Utilizing Wavelet Multi-Resolution Analysis," in *Proceedings of ION NTM,* 26-28 January, San Diego CA, pp. 260-266, U. S. Institute of Navigation, Fairfax VA

Barbour, N. and G. Schmidt (2001) "Inertial Sensor Technology Trends" *Sensors Journal*, vol. 1, no. 4, December, IEEE, pp. 332-339

Braasch, M. S. (1996) "GPS Multipath Model Validation," *Position Location and Navigation Symposium,* vol. 1, April, IEEE, pp. 672-678

Brenner, M. (1995) "Integrated GPS/Inertial Fault Detection Availability," in *Proceedings of ION GPS*, 12-15 September, Palm Springs CA, pp. 1949-1958, U. S. Institute of Navigation, Fairfax VA

Brown, A., and Y. Lu. (2004) "Performance Test Results of an Integrated GPS/MEMS Inertial Navigation Package," in *Proceedings of ION GPS*, 21-24 September, Long Beach CA, pp. 825-832, U. S. Institute of Navigation, Fairfax VA

Brown, R. G. and P.Y.C. Hwang (1997) *Introduction to Random Signals and Applied Kalman Filtering.* John Wiley & Sons.

Bye, C.T., Hartmann, G.L., and Killen, A. (1997) "Inertial and GPS Technology Advances on the GGP Program," in *Proceedings of ION AM,* 30 June-2 July, Albuquerque NM, pp. 639-648, U. S. Institute of Navigation, Fairfax VA

Cao, F. X., D. K. Yang, A. G. Xu, J. Ma, W. D. Xiao, C. L. Law, K. V. Ling, and H. C. Chua (2002) "Low cost SINS/GPS Integration for Land Vehicle Navigation," in *Proceedings of Intelligent Transportation Systems*, 3-6 September, Singapore, IEEE, pp. 910-913.

Chansarkar, M. M. and L. Garin (2000) "Acquisition of GPS Signals at Very Low Signal to Noise Ratio," in *Proceedings of ION NTM*, 26-28 January, Anaheim CA, pp. 731-737, U. S. Institute of Navigation, Fairfax VA

Chiang, K.W. (2004) *INS/GPS Integration Using Neural Networks for Land Vehicular Navigation Applications*, PhD Thesis, Department of Geomatics Engineering, University of Calgary, Canada, UCGE Report No.20209.

Chiang, K. W., H. Hou, X. Niu and N. El-Sheimy (2004) "Improving the Positioning Accuracy of DGPS/MEMS IMU Integrated Systems Utilizing Cascade De-noising Algorithm" in *Proceedings of ION GPS*, 21-24 September, Long Beach CA, pp. 809-818, U. S. Institute of Navigation, Fairfax VA

Crista- Interface/Operation Document, (2004) *Crista Inertial Measurement Unit (IMU) Interface / Operation Document*. A Cloud Cap Technology Inc.

Dana, P. H. (1999) *Global Positioning System Overview,* Department of Geography, University of Colorado at Boulder
(Available Online: http://www.colorado.edu/geography/gcraft/notes/gps/gps_f.html)

El-Sheimy, N. (2004) *Inertial techniques and INS/DGPS Integration*, ENGO 623- Course Notes, Department of Geomatics Engineering, University of Calgary, Canada

Farrell, J. A. and M. Barth (2001) *The Global Positioning System & Inertial Navigation*, McGraw Hills.

Faulkner, N. M., S. J. Cooper, and P. A. Jeary (2002) "Integrated MEMS/GPS Navigation Systems," *Position Location and Navigation Symposium,* April, Palm Springs CA, IEEE, pp. 306-313

Ford, T., J. Neumann, P. Fenton, M. Bobye, and J. Hamilton (2001) "OEM4 Inertial: A Tightly Integrated Decentralized Inertial/GPS Navigation System," in *Proceedings of ION GPS,* 11-14 September, Salt Lake City UT, pp. 3153-3163, U. S. Institute of Navigation, Fairfax VA

Fontana, D. R., W. Cheung, and T. Stansell (2001) "The Modernized L2 Civil Signal – Leaping Forward in the 21st Century," GPS World, 1st September, pp 28-34

Gao, Y. (2004) *Advanced Estimation Methods and Analysis* ENGO 629- Course notes, Department of Geomatics Engineering, University of Calgary, Canada

Gaylor, D. E. (2003) *Integrated GPS/INS Navigation System Design for Autonomous Spacecraft Rendezvous*, PhD Thesis. The University of Texas at Austin, USA.

Gelb, A. (1974) *Applied Optimal Estimation*. The Massachusetts Institute of Technology Press, USA

Godha, S. and M. E. Cannon (2005a) "Integration of DGPS with a MEMS-Based Inertial Measurement Unit (IMU) for Land Vehicle Navigation Application," in *Proceedings of ION GPS,* 13-16 September, Long Beach CA, pp. 333-345, U. S. Institute of Navigation, Fairfax VA

Godha, S. and M. E. Cannon (2005b) "Development of a DGPS/MEMS IMU Integrated System for Navigation in Urban Canyon Conditions," in *Proceedings of International Symposium on GPS/GNSS*, 9-11 December, Hong Kong

Godha, S., M. G. Petovello, and G. Lachapelle (2005) **"**Performance Analysis of MEMS IMU/HSGPS/Magnetic Sensor Integrated System in Urban Canyons," in *Proceedings*

of ION GPS, 13-16 September, Long Beach, CA, pp. 1977-1990, U. S. Institute of Navigation, Fairfax VA

Grewal, S. M., L. R. Weill, and A. P. Andrews (2001) *Global Positioning Systems, Inertial Navigation and Integration,* John Wiley and Sons Inc.

Grewal, M. and A. P. Andrews (2001) *Kalman Filtering: Theory and Practice Using Matlab*, John Wiley and Sons Inc.

Hoffmann-Wellenhof, B., H. Lichtenegger, and J. Collins (1992) *Global Positioning System: Theory and Practice*, Springer New York.

Hou, H. (2004) *Modeling Inertial Sensors Errors Using Allan Variance*, MSc Thesis, Department of Geomatics Engineering, University of Calgary, Canada, UCGE Report No. 20201.

Hide, C. D. (2003) *Integration of GPS and Low Cost INS Measurements*, PhD Thesis, Institute of Engineering, Surveying and Space Geodesy, University of Nottingham, UK

Hide, C. D. and T. Moore (2004) "Low Cost Sensors, High Quality Integration," in *Proceedings of NAV/AIS04, Location and Timing Applications*, London.

Hide, C. D. and T. Moore (2005) "GPS and Low Cost INS Integration for Positioning in the Urban Environment," in *Proceedings of ION GPS,* 13-16 September, Long Beach CA, pp. 1007-1015, U. S. Institute of Navigation, Fairfax VA

IEEE Standard (2001) *Standard for Inertial Sensor Terminology*, IEEE Standard IS 528-2001.

Jekeli, C. (2001) *Inertial Navigation Systems with Geodetic Applications*, Walter de Gryter GmBH and Co.

Kaplan, E. D. (1996) *Understanding GPS: Principles and Applications*, Artech House Inc., Norwood, MA.

Kealy, A., S. Young, F. Leahy and P. Cross (2001) "Improving the Performance of Satellite Navigation Systems for Land Mobile Applications through the Integration of MEMS inertial sensors" in *Proceedings of ION GPS,* 11-14 September, Salt Lake City UT, pp. 1394-1402, U. S. Institute of Navigation, Fairfax VA

Knight, D. T. (1999) "Rapid Development of Tightly Coupled GPS/INS Systems," in *Aerospace and Electronic Systems Magazine,* vol. 12, no. 2, IEEE, pp. 14-18

Kondo, S., N. Kubo, and A. Yasuda (2005) "Improvement of the performance of prototype software GPS Receiver," in *Proceedings of International Symposium on GPS/GNSS,* 9-11 December, Hong Kong

Kraft, M. (1997) *Closed Loop Digital Accelerometer Employing Oversampling Conversion*, PhD Thesis, School of Engineering, Coventry University, UK.

Kreye, C., B. Eissfeller, and J. O. Winkel (2000) "Improvements of GNSS Receiver Performance Using Deeply Coupled INS Measurements," in *Proceedings of ION GPS*, 19-23 September, Salt Lake City UT, pp-844-854, U. S. Institute of Navigation, Fairfax VA

Kuusniemi, H. (2005) *User-Level Reliability and Quality Monitoring in Satellite-Based Personal Navigation,* PhD Thesis, Institute of Digital and Computer Systems, Tampere University of Technology, Finland.

Lachapelle, G. (1995) "Far Reaching Recommendations on GPS Made by High Level U.S. Study" in *International Journal for Geomatics*, vol. 9, no. 8, pp. 48-49

Lachapelle, G. (2003) *Advanced GPS Theory and Applications,* ENGO 625- Course notes, Department of Geomatics Engineering, University of Calgary, Canada

Lachapelle, G., O. Mezentsev, J. Collin, and G. Macgougan (2003) "Pedestrian and Vehicular Navigation Under Signal Masking using Integrated HSGPS and Self Contained Sensor Technologies" *11th World Congress, International Association of Institutes of Navigation*, 21-24 October, Berlin

Lee, H. (2002) "GPS/Pseudolites/SDINS Integration approach for Kinematic Applications," in *Proceeding of ION GPS,* 24-27 September, Portland ON, pp. 1464-1473, U. S. Institute of Navigation, Fairfax VA

Liu, Z. (2002) *A Java-Based Wireless Framework for Location-Based Services Applications*, MSc Thesis, Department of Geomatics Engineering, University of Calgary, Canada, UCGE Report No. 20161

Macgougan, G. (2003) *High Sensitivity GPS Performance Analysis in Degraded Signal Environments,* MSc Thesis, Department of Geomatics Engineering, University of Calgary, Canada, UCGE Report No. 20176

Mathur, N. G. (1999) *Feasibility of Using a Low-Cost Inertial Measurement Unit with Centimeter Accuracy Differential Global Positioning System*, PhD Thesis, Ohio University, USA, UMI No. 9975068

Mathur, N. G. and F. V. Grass (2000) "Feasibility of using a Low-Cost Inertial Measurement Unit with Centimeter-Level GPS" in *Proceedings of ION AM,* 26-28 June, San Diego CA, pp. 712-720, U. S. Institute of Navigation, Fairfax VA

Mao, X., M. Wada, H. Hashimoto (2002) "Investigation on Nonlinear Filtering Algorithms for GPS" in *Intelligent Vehicle Symposium*, vol. 1, June, IEEE, pp. 64-70

Meditch, S. (1969) *Stochastic Optimal Linear Estimation and Control,* McGraw-Hill, New York.

Mezentsev, O. (2005) *Sensor Aiding of HSGPS Pedestrian Navigation*, PhD Thesis, Department of Geomatics Engineering, University of Calgary, Canada. UCGE Report No. 20212

Misra, P. and P. Enge (2001) *Global Positioning System- Signals, Measurements, and Performance*, Ganga Jamuna Press.

Nassar, S. (2003) *Improving the Inertial Navigation System (INS) Error Model for INS and INS/DGPS Applications*, PhD Thesis, Department of Geomatics Engineering, University of Calgary, Canada, UCGE Report No. 20183

Nayak, R. A. (2000) *Reliable and Continuous Urban Navigation Using Multiple GPS Antennas and a Low Cost IMU*, MSc Thesis, Department of Geomatics Engineering, , University of Calgary, Canada. UCGE Report No. 20142

Numajima, T., Kihara M., Kubo Y., Sugimoto S. And Seki T. (2002) "INS/DGPS/VMS Integration for In-Motion Alignment" in *Proceedings of ION GPS*, 24-27 September, Portland OR, pp. 556-564, U. S. Institute of Navigation, Fairfax VA

Park, M. (2004) *Error Analysis and Stochastic Modeling of MEMS based Inertial Sensors for Land Vehicle Navigation Applications*, MSc Thesis, Department of Geomatics Engineering, University of Calgary, Canada, UCGE Report No. 20194

Park, M. and Y. Gao (2002) "Error Analysis of Low Cost MEMS-Based Accelerometers for Land Vehicle Navigation," in *Proceedings of ION GPS*, 24-27 September, Portland OR, pp. 1162-1170, U. S. Institute of Navigation, Fairfax VA

Parkinson, B. W. and J. J. Spilker (1996) *The Global Positioning System: Theory and Applications,* American Institute of Aeronautics and Astronautics

Petovello, M. (2003) *Real-time Integration of a Tactical-Grade IMU and GPS for High-Accuracy Positioning and Navigation,* PhD Thesis, Department of Geomatics Engineering, University of Calgary, Canada, UCGE Report No. 20173

Petovello, M., M. E. Cannon, and G. Lachapelle (2003) "Quantifying Improvements from the Integration of GPS and a Tactical Grade INS in High Accuracy Navigation Applications," in *Proceedings of ION NTM,* 22-24 January, Anaheim CA, pp. 454-465, U. S. Institute of Navigation, Fairfax VA

Petovello, M., M. E. Cannon, and G. Lachapelle (2000) *C3NavG2^{TM} Operating Manual,* Department of Geomatics Engineering, University of Calgary, Canada

POSPac- Product Manual (2001) *Position and Orientation System, Post-Processing Package*, Applanix Corporation, Canada

Ray, J. K. (2000) *Mitigation of GPS Code and Carrier Phase Multipath Effects using a Multi-Antenna System,* PhD Thesis, Department of Geomatics Engineering, University of Calgary, Canada, UCGE Report No. 20136

Raquet, J. F. (1998) *Development of a Method for Kinematic GPS Carrier-Phase Ambiguity Resolution Using Multiple Reference Receiver*. PhD Thesis, Department of Geomatics Engineering, University of Calgary, Canada, UCGE Report No. 20116

Rogers, R. M. (2000) *Applied Mathematics in Integrated Navigation Systems*, AIAA Education Series

Satirapod, C., Wang, J. (2000) "Comparing the Quality Indicators of GPS Carrier Phase Observations" *Geomatics Research Australasia,* vol. 73, pp. 75-92.

Salychev, O. S. (1998) *Inertial Systems in Navigation and Geophysics*, Bauman MSTU Press

Salychev, O., V.V. Voronov, M. E. Cannon, R. A. Nayak and G. Lachapelle (2000) "Low Cost INS/GPS Integration: Concepts and Testing," in *Proceedings of ION NTM,* 26-28 January, Anaheim CA, pp. 98-105, U. S. Institute of Navigation, Fairfax VA

Salycheva, A. (2004) *Medium Accuracy INS/GPS Integration in Various GPS Environments*, MSc Thesis, Department of Geomatics Engineering, University of Calgary, Canada, UCGE Report No. 20200

Salycheva, A. and M. E. Cannon (2004) "Kinematic Azimuth Alignment of INS using GPS Velocity Information," in *Proceedings of ION NTM*, 26-28 January, San Diego CA, pp. 1103-1113, U. S. Institute of Navigation, Fairfax VA

Savage, P. G. (2000) *Strapdown Analytics,* vol. 1. Strapdown Associates, Inc.

Scherzinger, B. (2004) *Estimation with Application to Navigation*, ENGO 699.11-Course Notes, Department of Geomatics Engineering, University of Calgary, Canada

Schwarz, K. P., M. E. Cannon, and R. V. C. Wong (1989) "A Comparison of GPS Kinematic Models for the Determination of Position and Velocity Along a Trajectory," *Manuscripta Geodaetica*, vol. 14, pp. 345-353.

Scott, C. (1994) "Improved GPS Positioning for Motor Vehicles through Map Matching," in *Proceedings of ION GPS*, 20-23 September, Salt Lake City UT, pp. 1391-1400, U. S. Institute of Navigation, Fairfax VA

Shin, E. (2001) *Accuracy Improvement of Low Cost INS/GPS for Land Application*, MSc Thesis, Department of Geomatics Engineering, University of Calgary, Canada, UCGE Report No. 20156

Shin, E. and N. El-Sheimy, N. (2002) "Optimizing Smoothing Computations for Near Real Time GPS Measurement Gap Filling in INS/GPS Systems," in *Proceedings of ION GPS,* 24-27 September, Portland OR, pp. 1434-1441, U. S. Institute of Navigation, Fairfax VA

Shin, E., and N. El-Sheimy (2004) "An Unscented Kalman Filter for In-Motion Alignment of Low Cost IMUs," in *Proceedings of Position Location and Navigation Symposium IEEE*, 26-29 April, pp. 273-279

Shin, E. (2005) *Estimation Techniques for Low-Cost Inertial Navigation*, PhD Thesis, Department of Geomatics Engineering, University of Calgary, Canada, UCGE Report No. 20219

Shin, E, and N. El-Sheimy (2005) "Backward Smoothing for Pipeline Surveying Applications," in *Proceedings of ION NTM,* 24-26 January, San Diego CA, pp. 921-927, U. S. Institute of Navigation, Fairfax VA

Shin, E., X. Niu, and El-Sheimy N. (2005) "Performance Comparison of the Extended and the Unscented Kalman Filter for Integrated GPS and MEMS-Based Inertial Systems," in *Proceedings of ION NTM,* 24-26 January, San Diego CA, pp. 961-969, U. S. Institute of Navigation, Fairfax VA

Shreshtha, S. M. (2003) *Investigations into the Estimation of Tropospheric Delay and Wet Refractivity Using GPS Measurements,* MSc Thesis, Department of Geomatics Engineering, University of Calgary, Canada, UCGE Report No. 20180

Skaloud, J. (1999) *Optimizing Georeferencing of Airborne Survey Systems by INS/DGPS*, PhD Thesis, Department of Geomatics Engineering, University of Calgary, Canada, UCGE Report No. 20126

Sukkarieh, S. (2000) *Low Cost, High Integrity, Aided Inertial Navigation Systems for Autonomous Land Vehicles*, PhD Thesis, Department of Mechanical and Mechatronic Engineering, University of Sydney, Australia

Syed, S. (2005) *Development of Map-Aided GPS Algorithms for Vehicle Navigation in Urban Canyons*, MSc Thesis, Department of Geomatics Engineering, University of Calgary, Canada, UCGE Report No. 20225

Teunissen, P. J. G. and M. A. Salzmann (1989) "A Recursive Slippage Test for Use in State-Space Filtering," *Manuscripta Geodaetica*, vol. 14, pp. 383-390.

van Digglen, F. (1998) "GPS Accuracy: Lies, Damn Lies and statistics," GPS World. 1998.

van Dierendonck, A. J. V., P. Fenton, and T. Ford (1992) "Theory and Performance of Narrow Correlator Spacing in a GPS receiver," *Journal of The Institute of Navigation*, vol. 39, no.3, pp. 265-283

Wang, J. and C. Wilson (2002) "Improving KGPS/INS Performance for Safety Applications with Vehicle Dynamic Constraints," in *Proceedings of ION GPS,* 24-27 September, Portland OR, pp. 1790-1797, U. S. Institute of Navigation, Fairfax VA

Wang, J-H. (2004) "The Aiding of a Low-Cost MEMS INS for Land Vehicle Navigation Using Fuzzy Logic Expert System," in *Proceedings of ION GPS,* 21-24 September, Long Beach CA, pp. 718-728, U. S. Institute of Navigation, Fairfax VA

Ward, P. W. (1996) "GPS Receiver Search Techniques," *Position Location and Navigation Symposium,* April, IEEE, pp. 604 - 611

Winkler, S., M. Buschmann, T. Kordes, H.-W. Schulz, and P. Vorsmann (2003) "MEMS based IMU Development, Calibration and Testing for Autonomous MAV Navigation," in *Proceedings of ION AM,* 23-25 June, Albuquerque NM, pp. 128-133, U. S. Institute of Navigation, Fairfax VA

Xin-Xiang, J. (1996) *Theory of Carrier Adjusted DGPS Positioning Approach and Some Experimental Results,"* PhD Thesis, Delft University of Technology

Zhao, L., Y. O. Washington, M. A. Quddus and B.N. Robert (2003) "Extended Kalman Filter and Map Matching Algorithm for an Integrated GPS/Dead Reckoning System for Transport and Telematics Applications," *Journal of Navigation*, vol. 56, pp. 257-275

Zhang, J., Z. Jin, and W. Tian (2003) "A Suboptimal Kalman Filter with Fading Factors for DGPS/MEMS-IMU/Magnetic Compass Integrated Navigation," in *Proceedings of Intelligent Transportation Systems,* 12-15 October, IEEE, pp. 1229-1234

Zhang, X. (2003) *Integration of GPS with a Medium Accuracy IMU for Metre-Level Positioning,* MSc Thesis, Department. of Geomatics Engineering, University of Calgary, Canada, UCGE Report No. 20178

Zhang, Z. (1997) *Impact of Rubidium Clock Aiding on GPS Augmented Vehicular Navigation,* MSc Thesis, Department of Geomatics Engineering, University of Calgary, Canada, UCGE Report No. 20112

Zumberge, J. F. and W. I. Bertiger (1996) "Ephemeris and Clock Navigation Message Accuracy," [Chapter 16] in *The Global Positioning System: Theory and Applications*, B. W. Parkinson and J. J. Spilker., ed., American Institute of Aeronautics and Astronautics, Reston, VA

All theses references pertaining to the University of Calgary are available at:
(http://www.ensu.ucalgary.ca/links/GradTheses.html).

APPENDIX A

Accuracy Assessment of a Low Cost Magnetometer

This appendix characterizes the quality of the heading solution that can be obtained from a magnetometer in different environments. Figure A.1 shows the raw heading measurements (after removing spikes) obtained from HMR2330r magnetometer, in the open area field test (refer to Chapter Five). Figure A.2 shows the errors in heading solution with respect to reference heading obtained from CIMU. Figure A.3 shows the corresponding heading errors in urban areas, while Table A.1 lists the error statistics.

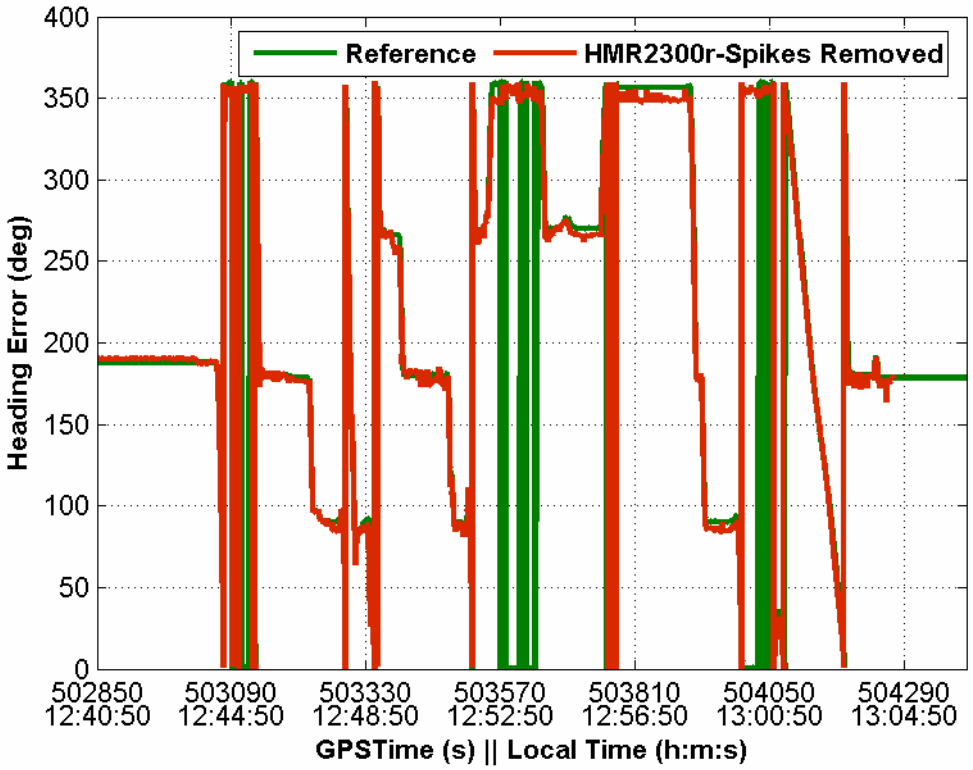

Figure A.1: Raw Heading after Removing Spikes through Interpolation

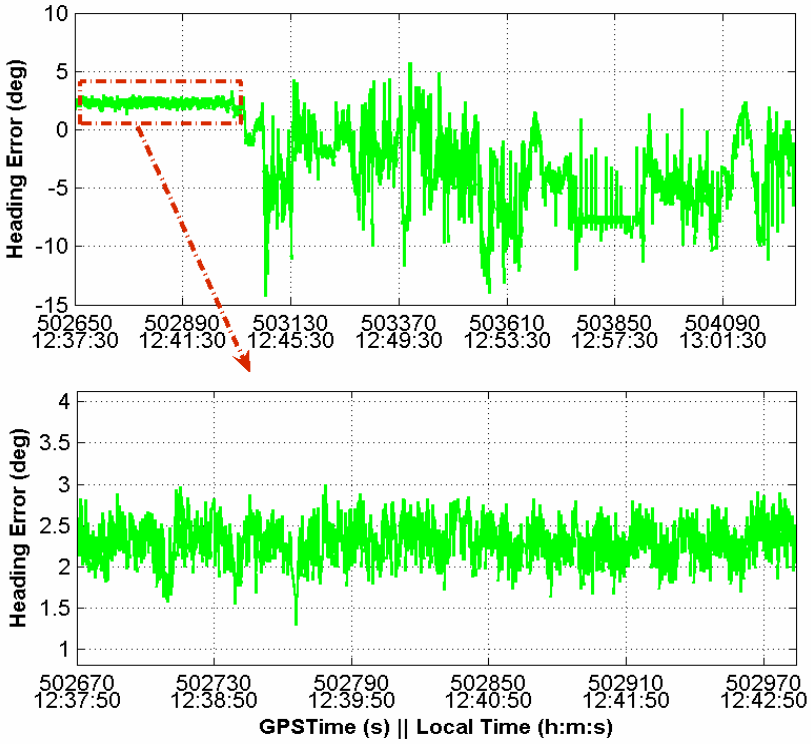

Figure A.2: Heading Error after Removing Spikes in Open Areas

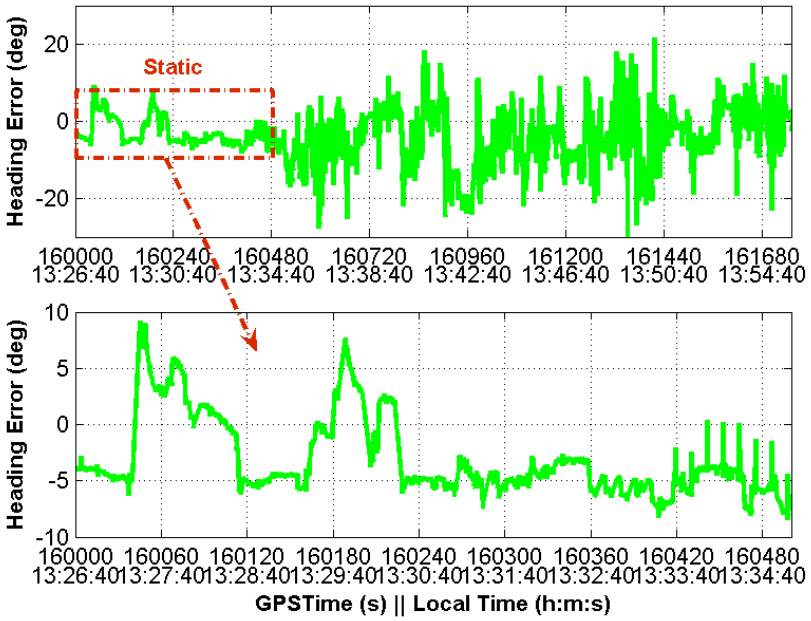

Figure A.3: Heading Errors after Removing Spikes in Urban Canyons

Table A.1: Heading Error Statistics

	GPS Time (s)	***Std. (˚)***
	Open Area	
Static	<503060	<0.5
Kinematic	>503060	3.5-4
	Urban Canyon	
Static	<160550	6.5
Kinematic	>160550	8.5

Table shows that the accuracy of the heading solution, in the open area (relatively free from magnetic interference sources), when the vehicle is static, is less than 0.5˚, and thus can be used to initialize a low cost MEMS INS. However, in urban canyons the magnetic disturbances are large such that the errors are greater than 6˚.

APPENDIX B

North, East, and Up Velocity Error Dynamics

The North, East and up velocity error dynamics is dependent on the attitude errors and the accelerometer sensor errors (El-sheimy, 2004). Their error dynamics equation is given by Equation (B.1).

$$\begin{bmatrix} \delta\dot{v}^e \\ \delta\dot{v}^n \\ \delta\dot{v}^u \end{bmatrix} = \begin{bmatrix} 0 & f^u & -f^n \\ -f^u & 0 & f^e \\ f^n & -f^e & 0 \end{bmatrix} \begin{bmatrix} \delta\eta \\ \delta\xi \\ \delta\psi \end{bmatrix} + \begin{bmatrix} \delta f^e \\ \delta f^n \\ \delta f^u \end{bmatrix} \tag{B.1}$$

where,

v^i is the velocity in 'l-frame',

f^i is the specific force in 'l-frame',

ξ is the roll,

η is the pitch,

ψ is the heading, and

δf^i is the accelerometer sensor errors in 'l-frame',

It can be noted from Equation (B.1) that the errors in north and east velocities are related to errors in pitch and roll, respectively, through specific force in up directions, which is typically close to gravity ($9.8\ m/s^2$). Consequently, a strong coupling exists between the tilt estimation and the horizontal velocities, and thus, any dynamical change in estimation of one over time will show on the other. This means that accurate estimation of velocity

error states by any suitable velocity updates measurements, not only improves the accuracy of velocity estimation, but also the accuracy of computed roll and pitch angles.

It can also be noted from Equation (B.1) that errors in roll and pitch estimation, projects the up acceleration in horizontal direction, which can potentially lead to large errors in velocity estimation. This substantiates the necessity for accurate estimation of tilt angles. Similarly, error in estimation of heading projects the forward velocity in lateral direction. The second factor that affects the velocity estimation is the accelerometer sensor errors, as it bears direct relation to velocities. So, any unresolved sensor errors leads to inaccurate velocity solution, which ultimately introduces errors in position solution.